ELECTRONIC STRUCTURE AND PHOTOEXCITATION DYNAMICS OF CHEMISORBED ALKALI ATOMS INDUCED RESONANCES

by

Shengmin Zhang

B.S. in Physics, USTC, Hefei, 2009

M.S. in Physics, University of Pittsburgh, Pittsburgh, 2011

Submitted to the Graduate Faculty of

the Dietrich School of Arts and Sciences in partial fulfillment

of the requirements for the degree of

Doctor of Philosophy

University of Pittsburgh

2017

UNIVERSITY OF PITTSBURGH

DIETRICH SCHOOL OF ARTS AND SCIENCES

This dissertation was presented

by

Shengmin Zhang

It was defended on

March 20th, 2017

and approved by

Dr. Hrvoje Petek, Department of Physics and Astronomy

Dr. Jeremy Levy, Department of Physics and Astronomy

Dr. Vincent Liu, Department of Physics and Astronomy

Dr. Ayres Freitas, Department of Physics and Astronomy

Dr. Haitao Liu, Department of Chemistry

Dissertation Director: Dr. Hrvoje Petek, Department of Physics and Astronomy

ELECTRONIC STRUCTURE AND PHOTOEXCITATION DYNAMICS OF CHEMISORBED ALKALI ATOMS INDUCED RESONANCES

Shengmin Zhang, PhD

University of Pittsburgh, 2017

We investigate the electronic structure and photoexcitation dynamics of alkali atoms (Rb and Cs) chemisorbed on Ru(0001) and Cu(111) surfaces by angle and time-resolved multi-photon photoemission (mPP) spectroscopy. Although the electronic structure of alkali atoms on noble surfaces has been studied, the development of mPP methods, combined with wavelength tunable femtosecond laser excitation, provides more incisive tools for exploration of alkali chemisorption induced electronic resonances and probing of electron relaxation dynamics. On Ru(0001), three-photon photoemission (3PP) spectroscopic features due to the σ- and π-resonances arising from the ns and np states of free alkali atoms are observed at $\sim$2 and $\sim$1 eV below the vacuum level in the zero coverage limit, respectively. As the alkali coverage is increased to 0.02 monolayer, the resonances are stabilized by formation of a surface dipole layer and form dispersive bands with nearly free-electron mass. Density functional theory calculations confirm the band formation through substrate-mediated interaction involving hybridization with the unoccupied d-bands. Time-resolved measurements provide

the experimental measurements of phase and population decay in the 3PP process via σ- and π-resonances; simulations by solving the four-energy level optical Bloch equations quantify the phase and population relaxation times. By contrast, on Cu(111) we observe clear signatures of Cs and Rb alkali atom-localized electronic states in 3PP spectra. The angular distributions reflect the non-dispersive σ and π symmetries of the alkali atom localized states. Due to the high dispersion of Shockley surface state (SS) of Cu(111), the resonant two-photon transition is driven from SS to π-resonance under visible light. Time-resolved measurements and corresponding Fourier transforms (FT) with respect to time describe the phase and population relaxation dynamics. In the case of the σ-resonance with $\hbar\nu$=1.92 eV, the interferometric measurements contain extra frequency components at fractions of the laser frequency, which we attribute to multielectron (ME) dynamics. Two-dimensional electronic spectroscopy shows that the photoexcitation creates coherent polarization components outside of the excitation laser bandwidth, through Coulomb interaction induced decay of an electron excited from the SS to a two-photon virtual state decaying into one electron in the σ-resonance and the other excited from SS to the Fermi level.

TABLE OF CONTENTS

LIST OF TABLES

LIST OF FIGURES

LIST OF ABBREVIATION

1PP : one-photon photoemission

2PP : two-photon photoemission

AR : antibonding resonance (i.e., m = 0 resonance)

AR1PP : angle-resolved one-photon photoemission

AR2PP : angle-resolved two-photon photoemission

ARPES : angle-resolved photoemission spectroscopy

BBO : beta-barium borate

cps : counts per second

DFT : density functional theory

DOS : density of states

EDC : energy distribution curve

E_F : Fermi level

E_f : final state energy

E_i : initial state energy

E_{int} : intermediate state energy

E_{kin} : kinetic energy

ELS : energy loss spectroscopy

E_m : intermediate state energy

E_p : pass energy

eV : electron-volt

E_{vac} : vacuum level

fcc : face-centered cubic

FWHM : full-width half maximum

GVD : group velocity dispersion

hcp : hexagonal close-packed

HOMO : highest occupied molecular orbital

I2PC : interferometric two-pulse correlation

IPES : inverse photoemission spectroscopy

IPS : image-potential state

ITR2PP : interferometric time-resolved two-photon photoemission

$k_{||}$: parallel momentum

LEED : low energy electron diffraction

L_{sp} : lower sp-band

LUMO : lowest unoccupied molecular orbital

m_e : mass of electron ($= 9.110^{-31}$ kg)

ML : monolayer

mPP : multi-photon photoemission

multi-electron : ME

NOPA : noncollinear optical parametric amplifier

OBE : optical Bloch equations

PEEM : photoemission electron microscope/microscopy

PES : photoemission/photoelectron spectroscopy

QMS : quadrupole mass spectrometer

RCT : resonant charge transfer

RGA : residual gas analyzer

SHG : second harmonic generation

SPM : self-phase modulation

SS : Shockley surface state

TE : transverse electric

THG : third harmonic generation

TM : transverse magnetic

TR-2PP : time-resolved two-photon photoemission

TR-mPP : time-resolved multi-photon photoemission

UHV : ultra-high vacuum

UPS : ultraviolet photoelectron spectroscopy

U_{sp} : upper sp-band

UV : ultraviolet

WPP : wave-packet propagation

XPS : X-ray photoelectron spectroscopy

PREFACE

I would like to thank my professor Dr. Hrvoje Petek for his continuous support, knowledge and encouragement for my Ph.D work. It is impossible to complete my research and dissertation without his supervision and dedication. I also want to thank my committee professors, Dr. Jeremy Levy, Dr. Vincent Liu, Dr. Ayres Freitas and Dr. Haitao Liu for their precious time to give guidance and advice.

I really appreciate all the support from my parents. My mother and my father always believe in me and were supportive no matter how tough the situation was. I would like to take this chance to thank you for supporting every decision I made and trying to help financially and spiritually. Thank you my dear parents again for staying with me during this long journey. The special thanks are going to Dr. Xuefeng Cui, Dr. Jin Zhao and Dr. Cong Wang. They are not only my lab mates but also very good friends, who were always there for me whenever I need help. There are a lot of other friends from my lab, from our department, from our school and from my college, who are willing to help at crucial instances without hesitation. I feel very lucky.

One journey starts and one journey ends.

1.0 INTRODUCTION

The subject of this thesis is the study of the electronic structure and ultrafast electron dynamics of alkali atoms adsorbed noble and transition metal surfaces by multi-photon photoemission (mPP) spectroscopy and time-resolved mPP (TR-mPP). Chemisorption of atoms and molecules is important for many interfacial phenomena, such as the charge transport, sensing, thermionic emission, catalysis, etc. The properties of the chemisorbed interfaces depend on the alignment of the occupied and unoccupied electronic states with respect to the Fermi level. Although the system of alkali atoms on noble metals has been explored by experiment and theory for nearly 100 years, as the capability of experimental methods evolves, new features become accessible to experimental study. Moreover, the electronic structure of alkali atoms on transition metals has hardly been studied both experiment and theory. Multi-photon photoemission spectroscopy provides the most direct and precise method to study the occupied and unoccupied electronic structure of a chemisorption interface. In the

prior research the mPP experiments were performed with fixed wavelength lasers, and the surface electronic structure had to be tuned into resonance with the laser by the alkali atom surface coverage. With a broadly tunable laser system recently available in our laboratory, more refined measurements of the surface electronic structure at any sample coverage have become possible. The goal of this study is to explore the electronic structure of alkali atoms chemisorbed metal surfaces, and to explain and understand their electronic and dynamical properties. Additionally, with more advanced laser system, the TR-mPP method gives better resolution on the exploration of the excitation dynamics.

In this chapter, I will introduce the history and background of the alkali atoms chemisorbed metal surface system and the specific techniques of two-photon photoemission (2PP) technique.

1.1 CHARACTERISTICS OF NOBLE AND TRANSITION METALS

In this section, I will briefly discuss the noble and transition metals and their differences.

1.1.1 Noble metal surfaces

The physical properties of noble metals are defined by their electronic structure. Their d-bands are completely filled and reach up to 2.0 eV for Cu and 3.8 eV for Ag below the Fermi level. Their lone ns electron contributes to the metallic band structure. In a solid the ns and np orbitals hybridize to form the sp-conduction band. The simple Fermi surfaces and band structures of these monovalent elements have been studied extensively by both experiment and theory.[20] The screening properties of the fully occupied d-bands, the electron delocalization of the sp-band, and the chemical inertness, all related to the band structure, make noble metals ideal conductors of electricity.

The noble metals have the face-centered cubic (fcc) crystal structure. Their Fermi surfaces are completely enclosed within the first Brillouin zone. Since I only used Cu among the noble metals for my research, I will focus on its description. The Miller indices of the low index facets of fcc noble surfaces are designated as (111), (100) and (110). The different atomic density and symmetry make them unique in space/band structure. The (111) surface, which is the most stable one, has a hexagonal close-packed (hcp) arrangement of atoms with the highest in-plane atomic density. Figure ?? shows the top and side views of three low index surfaces. The distance between the atomic planes play a very important role

on the filling of electronic states, because it determines the Brillouin zone boundaries. The (111) surface has a projected band gap between the upper occupied sp-band and the lower unoccupied sp-band, which affects the surface electronic structure and electronic interactions with adsorbates such as alkali atoms.

Figure ??(a) shows an fcc lattice structure of (111) surfaces and its corresponding reciprocal space in the first Brillouin zone. The Brillouin zone defines the allowable range of the crystal momenta and enables the band structure of a solid to be presented in the momentum space. The surface-projected band structure of Cu(111) in the Γ-L direction in Figure ??(b) is shown in Figure ??(a). The d-bands of Cu (not shown) reach up to -2.0 eV below the Fermi level, and do not play a role in my research. From the band structure it is understood that the sp-bands have nearly free electron dispersion with wave vector $\mathbf{k}$. The band gap that opens up in the (111) direction and extends between -0.89 to 4.25 eV.[21] Moreover, right under the Fermi level, the Shockley Surface (SS) state is located at ~ -0.4 eV; it disperses with an effective mass of 0.4 m_e. Another feature of the surface electronic structure is the image potential (IP) state; its band minimum is at -0.82 eV respective to vacuum level[21, 22] and it disperses with the free electron mass. Both SS and IP states will be discussed in more detail with the experimental results in Chapter 5.

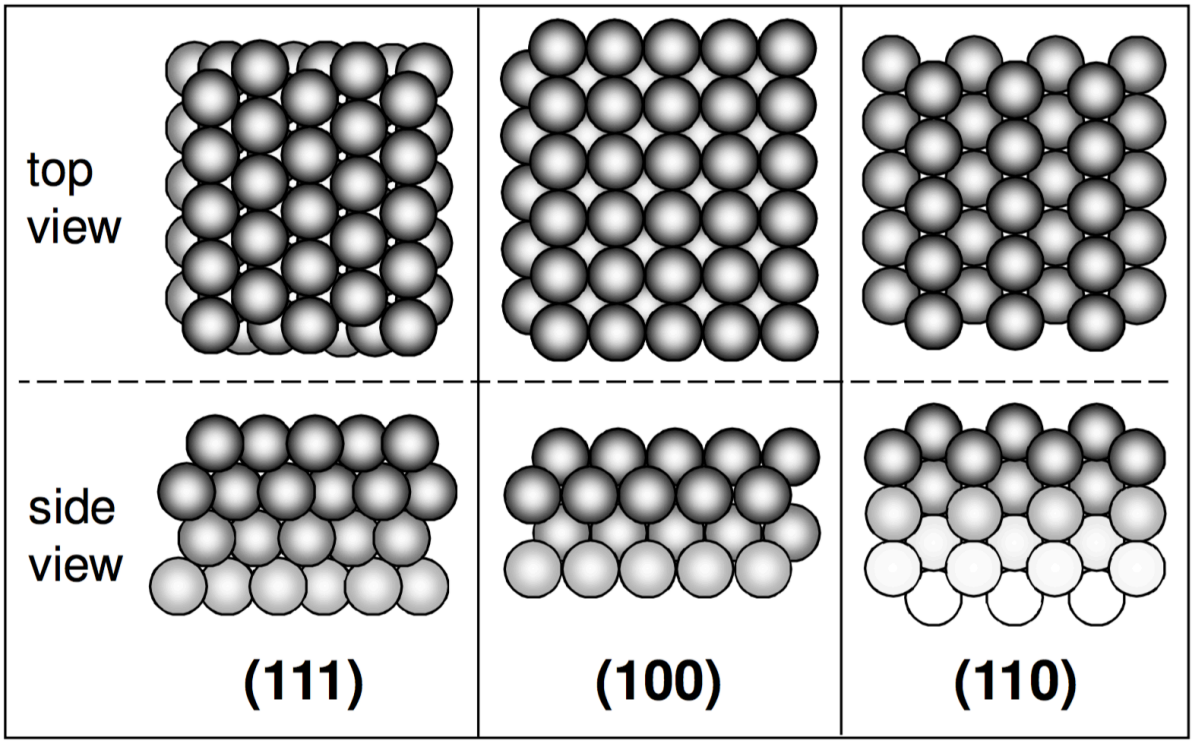

Figure 1.1: The top and side views of the atomic arrangements of noble metal surfaces with the Miller indices planes (111), (100) and (110), respectively.[1]

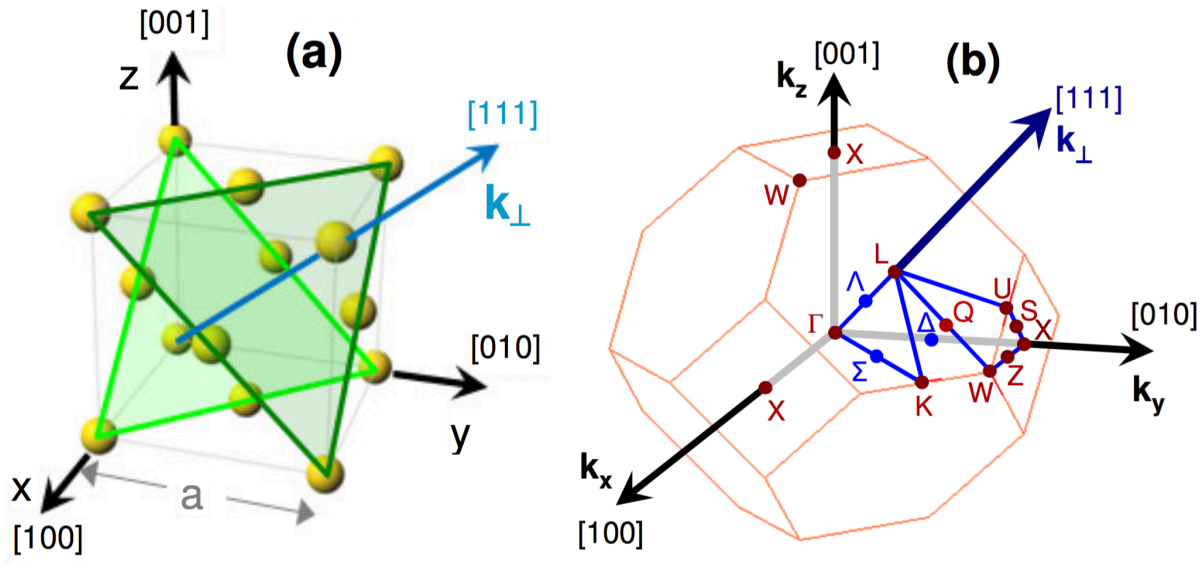

Figure 1.2: **a)** The fcc lattice structure. The (111) plane direction are marked with the green triangle. **b)** The first Brillouin Zone of the fcc lattice and the Γ point in the center of the structure is indicated as $k_{||}$=0 Å^{-1} in this thesis.

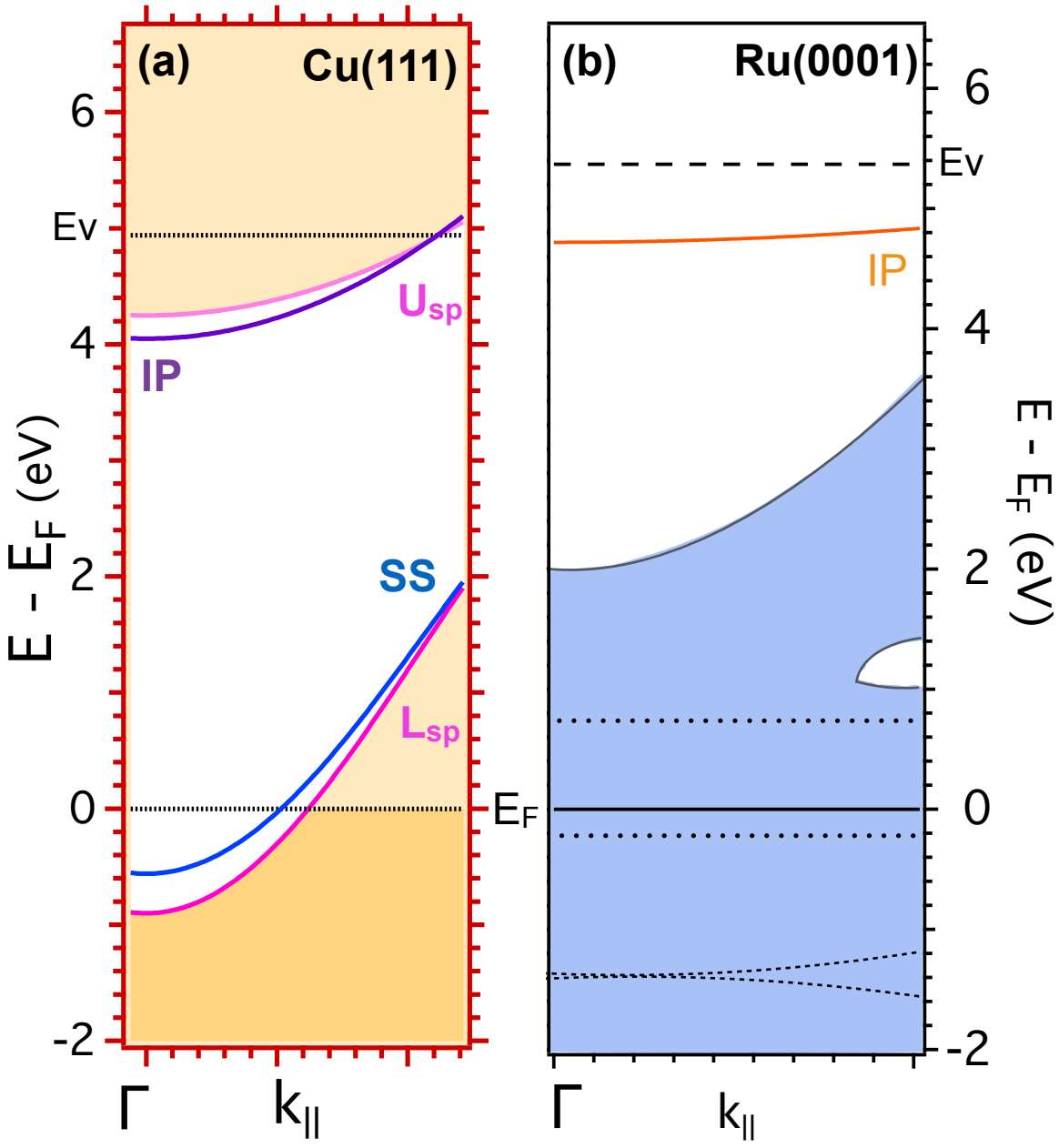

Figure 1.3: **a)** and **b)** are the electronic band structure of Cu(111)[2, 3, 4] and Ru(0001)[5, 6, 7] surfaces starting at the Γ point.

1.1.2 Transition metal surfaces

In the contrast with the noble metals, transition metals have partially occupied d-bands, which extend above the Fermi level. Figure ??(b) shows the electronic band structure of Ru(0001) to contrast it with that of the Cu(111) surface. Due to its hexagonal lattice structure, it is awkward to use standard Cartesian axes to describe the low index plane directions. Instead the notation is based on three axes at 60 degrees with respect to the close-packed plane, and an axis perpendicular to these planes. This leads to a four-digit index structure, as shown in Figure ??(b). A similarity with the noble metal (111) surface is that the (0001) plane is the most stable structure and both of them share the same hcp arrangement at the top layer, as shown in Figure ??(a). Figure ??(c) gives the first Brillouin zone with the plane direction marked, and the band structure in Figure ??(b) is following the Γ-M direction.

Like from Cu(111), Ru(0001) has an SS state, but at -5.5 eV below the Fermi level it is deeper than for copper,[6] and therefore it does not contribute to my mPP spectra. The IP state has the free electron dispersion as well on Ru(0001). The high energy unoccupied d-band provides the opportunity for adsorbates, like alkali atoms, to hybridize with it. This dissimilarity between Ru and Cu leads to the different spectroscopic features, which will be

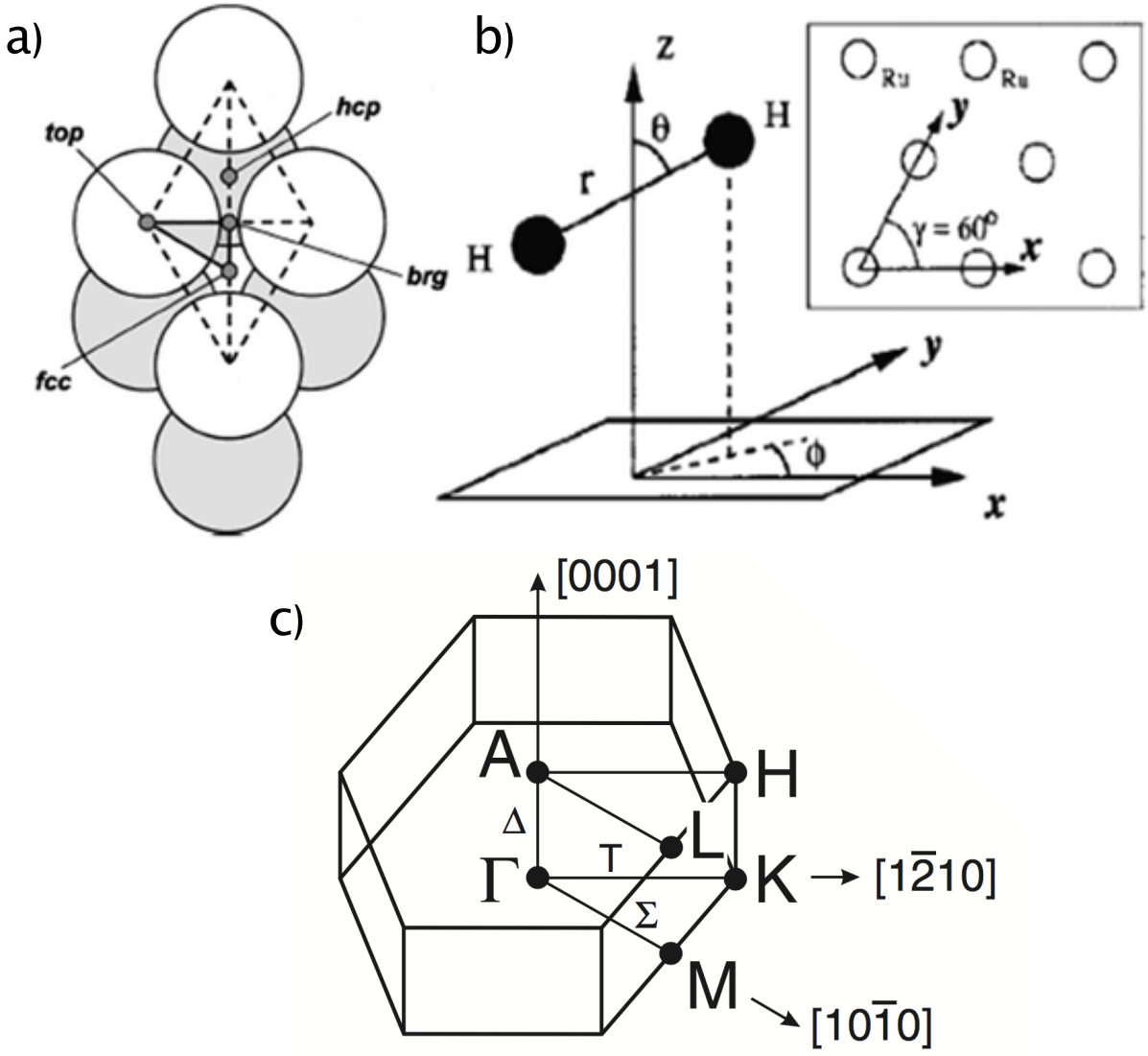

Figure 1.4: **a)** The Ru(0001) surface unit cell has four high symmetry points, which are indicated **b)** The coordinate system used to indicate the hexagonal lattice system. The x and y axis describe motion parallel to the surface, Z the motion perpendicular to the surface, r the H to H distance and θ and ϕ the polar and azimuthal angle of the molecular axis with the Z and X axis respetively.[8] **c)** The first Brillouin Zone of Ru hexagonal lattice.[6]

discussed in detail in Chapter 4.

1.2 ALKALI METALS AND CHEMISORPTION ON SINGLE CRYSTAL METAL SURFACES

Alkali atom chemisorption on metals has been a source of seminal ideas in surface science for several decades and yet as scientific techniques improve, more and more detailed information becomes accessible. In this section, I will give a brief background on alkali atom chemisorption on both the noble and transition metals.

1.2.1 Properties of Alkali Atoms

With a single valence *s*-orbital electron, the alkali atom elements (excluding hydrogen) form the simplest metal group. We focused on the two largest nonradioactive alkali metals, rubidium (Rb) and cesium (Cs), which are located within the left-most column (Group I) in the periodic table, as shown in Figure ??. The dominant interaction leading to chemisorption of alkali atoms is between their ns valence electron and the free electrons of the metal substrate that is mediated by the Coulomb field. Smaller alkali atoms are closer to the metal substrate,

and thus interact more strongly. Therefore, the spectroscopic and dynamical measurements reported herein are most accessible for Rb and Cs.

1.2.2 Alkali Atoms Adsorption on Solid Surfaces

Due to the simple electronic structure, alkali atoms are prototypical systems for studying the interaction between the atoms and molecules on the solid surfaces or the substrate itself. The earliest study of the interaction of alkali atoms and the metal surfaces was in 1920's by Langmuir and his coworkers.[23, 24] At a surface-atom distance of a few Ångstroms, the Coulomb image-charge interaction lifts the alkali ns electron above the Fermi level; this causes the ns electron to transfer from alkali atom to chemisorb in a predominantly ionic state.[12, 25, 26] The strong surface dipole formed by the ionic alkali atoms and their displaced electrons creates a surface potential, which causes a characteristic decrease of the surface work function.[27] Because of the ability to lower work functions of all materials, alkali atom-modified metal surfaces have found many applications in thermionic emission, catalysis, etc.[28, 29]

In their pioneering work, Langmuir and coworkers observed the work function decrease for a clean tungsten (W) surface by several eVs upon adsorption of Cs at submonolayer to monolayer (ML) coverage.[23, 24, 30, 31] Heating Cs covered W surface caused nearly

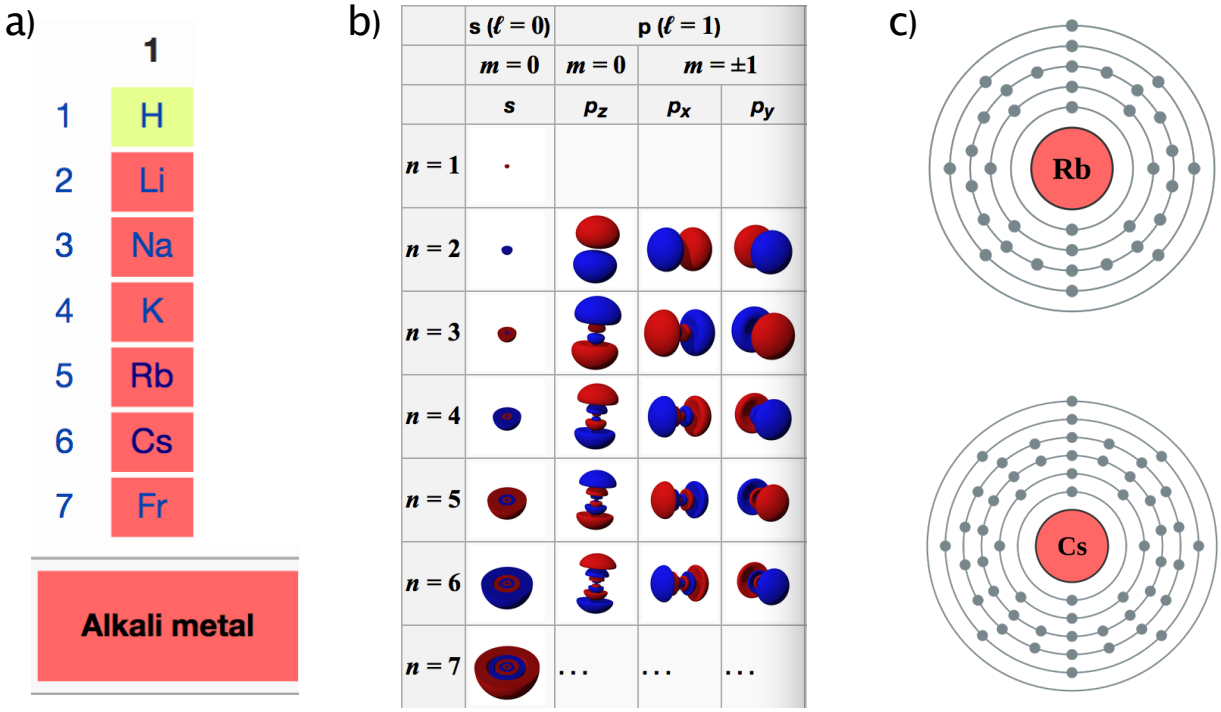

Figure 1.5: **a)** The first column indicating the position of Alkali atoms in Periodic Table of the Elements. **b)** The symmetry of s and p orbitals. **c)** The orbital diagrams of Rubidium and Cesium, which are the main topic of my study.

all Cs atoms to desorb as positive ions. Both described features formed the foundation of the alkali atoms on metal surfaces systems and they led to numerous practical applications such as low work function cathodes and thermionic energy conversion materials.[28] In 1932, Langmuir explained the mechanism of work function decrease by the fact that alkali atoms have low ionization potentials, which are significantly below the work function of W. This property energetically favored the transfer of the valence electron from alkali atoms to the substrate.[23]

In 1935, Gurney presented a quantum mechanical picture of chemisorption applicable to low adsorbate coverage in order to explain the effect of alkali earth atoms on the surface potential.[32] These alkali earth group atoms exhibit similar chemisorption properties to alkali atoms, because they can also easily give up one ns eletron, however their ionization potentials are higher than the work function of W. According to Gurney's interpretation, when an alkali or alkali earth atom approaches the substrate, its positive core is screened by the conduction band electrons in the substrate to create a negative image charge. The Coulomb repulsion between the negative image charge and the electron on ns valence destabilizes the latter. If the ns valence electron energy exceeds E_F of the substrate, it is broadened into a resonance because it can undergo transfer into the unoccupied states of the substrate. Therefore, the ns electron resonance energy and width are determined, respectively, by the

Coulomb repulsion and the tunneling rate. The degree of charge transfer into the substrate is determined by the fraction of the ns electron resonance density of states (DOS) above E_F.[33]

In 1970s, Lang developed a model for chemisorption where the substrate was represented by the "jellium" model.[34, 35, 36] The jellium model describes the delocalized valence electrons in metal to be interacting with a uniform positively charged background, which terminates at the physical interface between the metal and vacuum.[34] His calculations for the adsorbate-substrate interactions were based on pseudopotentials for the substrate and adsorbed atoms.[34] The model reproduced the general features of the Gurney model including that the position of the adsorbate valence level with respect to E_F of the substrate, and the characteristic work function decrease induced by alkali atoms.[34, 35, 36] Since the jellium model does not include details of substrate band structure, the calculated widths of the unoccupied resonances are much broader ($\sim$ 1 eV) than the subsequently observed and calculated widths for the Cu(111) and Ag(111) surfaces.[37]

With the aim of analyzing the relation of the electronic structure of chemisorbed alkali atoms and the work function variation quantitatively, Muscat and Newns constructed a new model in late 1970s, based on the Anderson impurity model,[38] where they extended the surface dipole fields by considering the intra-atomic polarization from the electric field of

the substrate.[38, 39, 40, 41, 42] The change of the work function was described in terms of adatom ion and intra-atomic dipole moment. On account of intra-atomic polarization, they predicted the hybridization of alkali atom s- and p-orbitals into a bonding and an antibonding pair forming two unoccupied resonances. The widths of these two resonances depend on whether the hybridized orbitals have maximum density between the substrate and adsorbate (wide), or on the vacuum side of adsorbate (narrow).[38]

Ten years later, Ishida applied density functional theory (DFT) calculations based on the local density approximation. In his work, the single alkali atom chemisorption approach was extended to finite coverage. His calculations predicted a relatively small amount of charge transfer and rather that chemisorption leads to an internal polarization of the charge density transferred between the substrate and the adsorbate.[43, 44] The chemical bond formed between the alkali atom and the substrate thus had significant covalent character, contrary to the previous models.

In 1990s, Nordlander and Tully introduced the influence of the surface potentials into the calculation of the energy shifts and lifetime broadening of the alkali-induced valence states.[25] They used the scattering approach at bond distances that are much larger than the equilibrium chemisorption bond length. Their calculations described how the intramolecular orbital hybridization influences on the resonance energies and widths as the interaction

strength approached the energy splittings between the interacting levels. At that time, however, lack of spectroscopic features in the conventional photoemission spectra of chemisorbed alkali atoms[45] did not provide a firm validation of the theory. Specifically, the photoemission spectra did not provide any evidence of the occupied ns electron DOS, which different theories predicted should exist unless alkali atoms were fully ionized, and therefore had narrow resonances.

Before ultrafast lasers enabled multi-photon photoemission (mPP) spectroscopy, various structural and spectroscopic methods have been applied in the experimental explorations of the alkali atom chemisorption.[33] A common surface science method, low-energy electron diffraction (LEED), has been utilized to determine the surface structure of alkali atoms chemisorbed metal surfaces.[46] With the reciprocal space LEED images, many studies have been performed at low (0.07 monolayer; ML) and high (0.25 ML) coverages.[33] At low coverages such as used in my experiments, alkali atoms mutually repel each other through repulsive dipole-dipole interaction to form hexactic liquid structures.[33, 47]

At higher coverages, there is probability for small alkali atoms (Li, Na) to absorb in three-fold hollow sites, while large alkali atoms (K, Rb, Cs) prefer to adsorb at on-top sites.[33, 48] With the DFT Calculations and LEED images, the lattice structures can be confirmed. In my study, the surface coverages are in the <0.07 ML range, where no structural information

exists. We believe that the hexactic liquid structure is still prevalent, though one should be concerned with the preferential adsorption at the step edges.

Employing electron energy loss spectroscopy (EELS) and inverse photoemission spectroscopy (IPES), Heskett and his coworkers studied Na[49, 49] and K[50] chemisorption on Al(111) surface as a function of coverages. They discovered a strong correlation between the peak energy of EELS and the unoccupied alkali-induced resonances in IPES, enabling them to interpret the EELS peaks as arising from an electronic transition at submonolayer alkali coverages. At low coverage of K on Al(111), they assigned unoccupied resonances feature at 0.6 eV and 2.7 eV for s- and p-resonances, respectively. Due to the limited energy resolution of their methods, it was difficult to determine the true widths of these resonances. Bartynski and his coworkers later used angle-resolved IPES to observe alkali-induced resonances of Cs/Cu(100) and Cs/Cu(111) at $\sim$ 3 eV relative to E_F. From the angle-resolved measurements, they concluded that the unoccupied resonances have predominantly d-character when resonant with the projected band gap and sp-character when resonant with the propagating conduction band states.[50]

The development of 2PP as a spectroscopic method for surface science by Steinmann and coworkers provided higher sensitivity and better resolution tool to probe the unoccupied electronic structure of clean and adsorbate modified metal surfaces.[51] In 1990s, Fischer

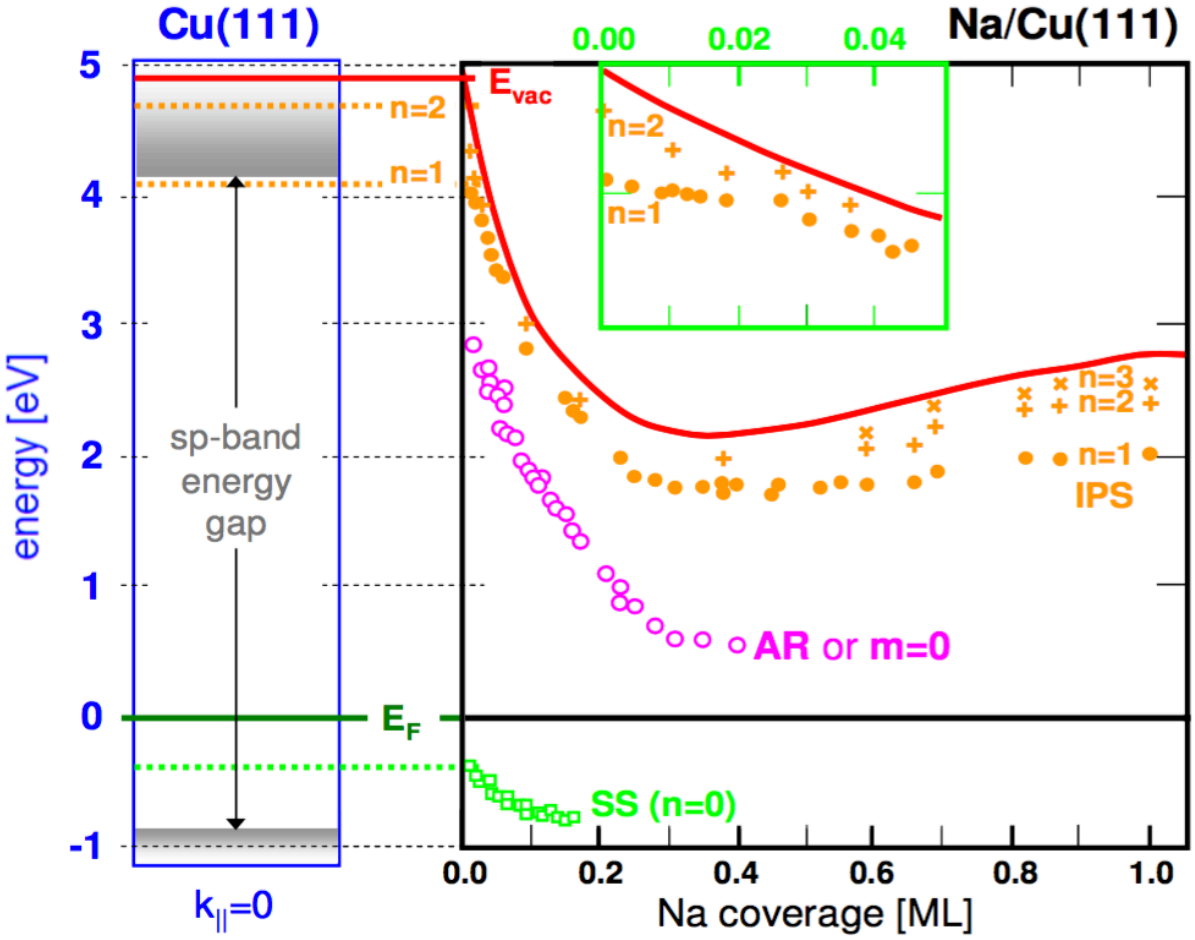

Figure 1.6: The electronic band structure of alkali absorbed noble metal system. Left is the energy diagram of clean Cu(111) surface at $k_{||}$=0 Å^{-1} point. Right is the experimental data of Na/Cu(111) system as function of alkali coverages from 2PP mesurements. The energy level diagram for 2PP on a clean Cu(111) surface including the Shockley surface (SS) state and n=1, 2 and 3 image potential (IP) states (left), and experimental tuning of those levels as a function of Na coverage, including the Na 3s resonance (m=0).[9, 10]

et al. applied 2PP with nanosecond laser excitation to explore the unoccupied electronic structure of Na adsorbed on Cu(111) surface.[9] They observed the alkali-induced unoccupied resonance and the image potential (IP) states of Cu(111). As the alkali atom coverage increased, they detected the expected downshift of the work function, as well as all the other states, as shown in Figure ??. The alkali-induced resonance was first observed at ∼2.9 eV above E_F for low coverages, and it had a linewidth of 410±30 meV. In addition, they measured how the resonance tuned to lower energy for coverages corresponding to the work function minimum, ∼0.40-0.45 ML. They attributed a sudden change in the occupancy of the alkali-induced resonance at this coverage to a transition from an ionic to metallic bonding as the overlayer coalesces into close-packed islands.[9]

As Ti:sapphire laser based ultrafast spectroscopic methods became available, time-resolved 2PP (TR2PP) was employed by the Aeschlimann group, to investigate energies and lifetimes of the unoccupied resonances of Cs adsorbed Cu(111) and Cu(100) surfaces.[52, 53] They found that the Cs resonance appeared at ∼3 eV in the low coverage limit, and measured its lifetime to be 15 fs at 300 K. Such lifetime appeared unexpectedly long because of the linewidths predicted by the theoretical models and observed in the previous work of Fischer et al. for Na/Cu(111) suggested a lifetimes in the femtosecond to subfemtosecond range.[9, 54] Moreover, Bauer et al. found that the lifetimes depend on the crystal lattice face because of

how the alkali resonances aligned with the band gaps in the metallic band structure.

In 1997, Petek and coworkers investigated the Cs/Cu(111) system by TR2PP at low temperature (∼33 K). They observed that cooling the surface increased the resonance lifetime to ∼50 fs, and the decay pattern became non-exponential. The complex decay kinetics in TR2PP measurements were interpreted as evidence for surface femtochemistry of desorption of Cs from Cu(111) surface.[16, 55, 56]

1.3 PHOTOEMISSION SPECTRUM AND DYNAMICS FEATURES

As mentioned in the last section, the development of time-resolved two-photon photoemission spectroscopy has provided an advanced method to explore the electronic structure and dynamics of alkali-modified metal surfaces. In this section, I will introduce the background such measurements.

1.3.1 Background of Photoemission

The photoemission technique is based on the photoelectric effect, where light with energy larger than the work function of the material excites electrons above the vacuum barrier,

whereby they are emitted into the vacuum.[57, 58] Many analytical methods surface science are based on energizing solid surfaces with photons or electrons, and detecting the emission of excited electrons into vacuum. We can summarize these experimental techniques into several groups: 1) photon in/out in X-Ray diffraction or photoluminescence; 2) electron in/out in electron diffraction or Auger electron spectroscopy; 3) electron-in/photon-out in inverse photoemission; and 4) photon-in/electron-out in photoemission spectroscopy.[59] Each method has its advantages for probing the electronic properties of solid surfaces. Here we use photoemission, in the form of mPP, to study the electronic band structure of the substrates, the DOS of alkali chemisorbed metal surfaces, and the electron dynamics of the corresponding features.

Photoemission spectroscopy provides information on the density of initial states below the Fermi level of a condensed matter system. Electrons are excited from the initial states to the final states above vacuum level (E_{vac}), which form a continuum with the density and transition probability that varies slowly with the energy. Monoenergetic photons are employed to excite a solid surface and analyze the energy *vs.* angle of emitted electrons.[60, 61] In the previous published research, it is usually performed with UV or synchrotron radiation light as excitation source, which cover photon energy range of 3-100 eV.[62] However, conventional photoemission spectroscopy measures only the occupied DOS.

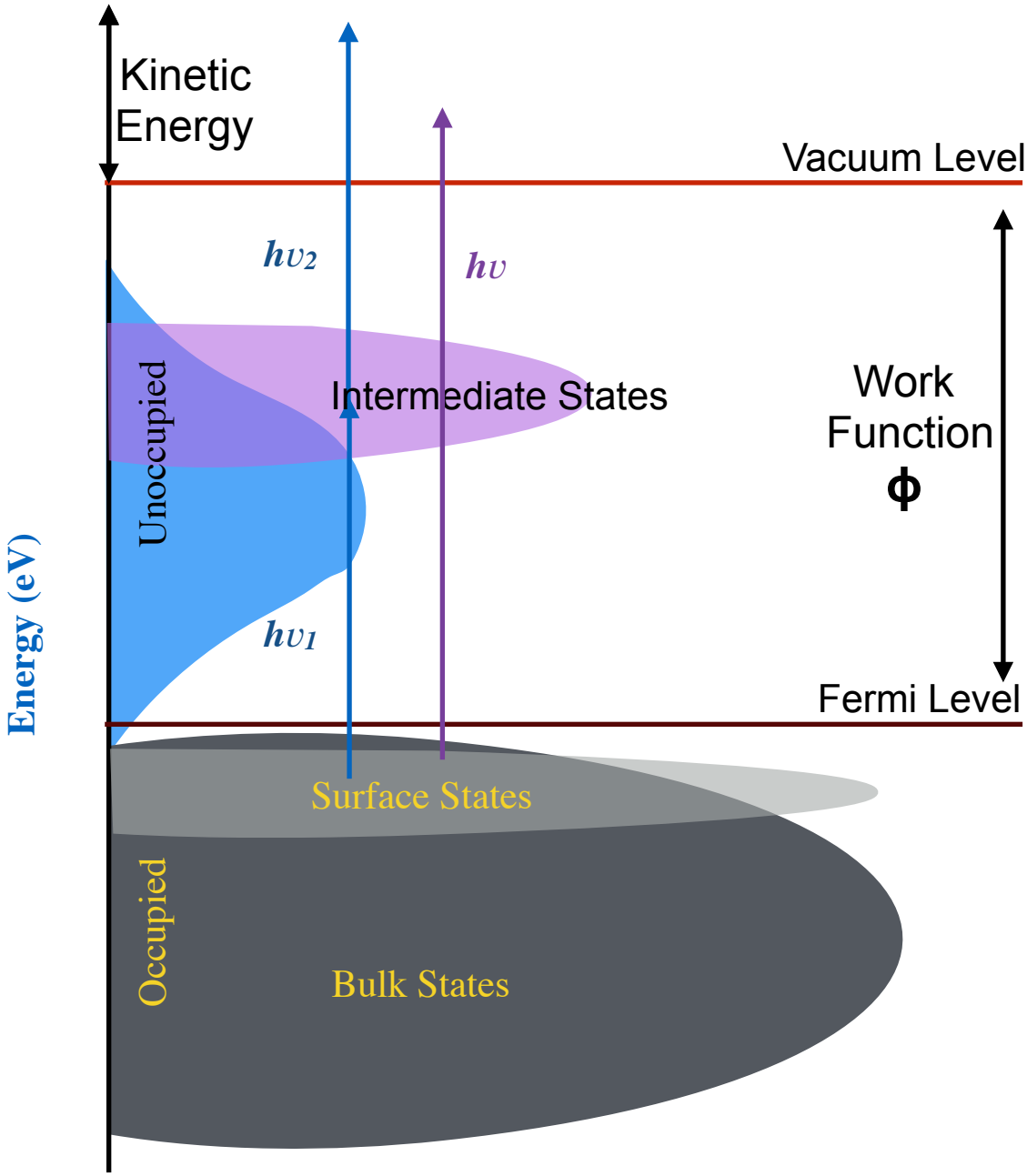

Figure 1.7: Schematic diagram of photoemission process with 1PP and 2PP, with the DOS distribution.

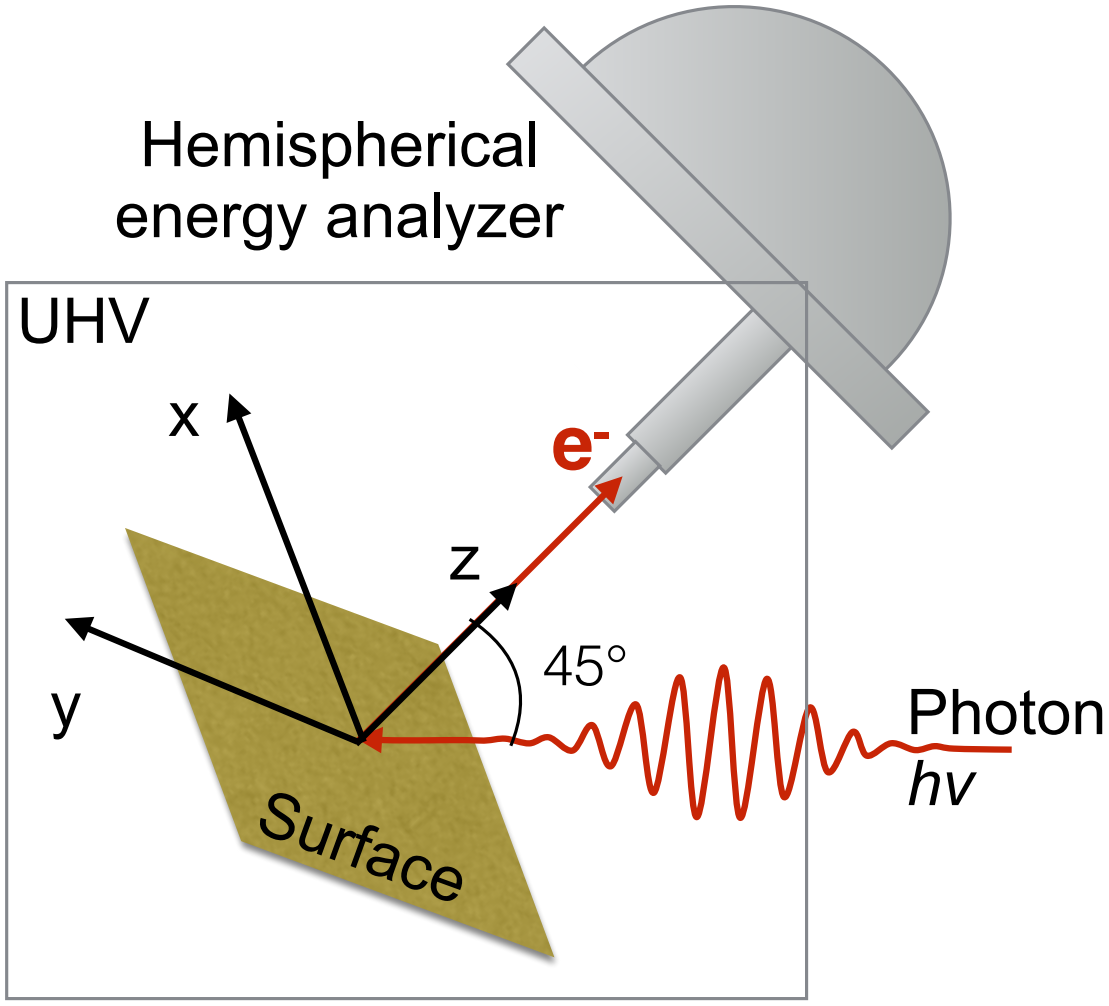

Figure 1.8: The three-dimensional illustration of the photoemission process on a solid sample in the ultra high vacuum chamber (square). The incident photon ($h\nu$) has 45 degree with the excited photoelectron (e^-) at the normal direction of sample. Photoelectrons are detected and measured by the energy analyzer.

The energy level scheme for photoemission spectroscopy is described in Figure ??, which shows the energy distribution of photoelectrons before and after the photoexcitation at different energy levels.[63] For the one photon photoemission (1PP) case, it is required to have $\hbar\nu > E_B + \Phi$ to excite the electrons from a state at binding energy (E_B), where E_B is the energy measured with respect to E_F and Φ is the work function of a solid surface (E_v-E_F); while for 2PP situation, the equation should be $2\hbar\nu > E_B + \Phi$. The spectrum of the photoexcited electrons in 1PP provides the information on the DOS of the occupied bands of a solid surface. In 2PP, or more generally, mPP the spectra contain additional information on the unoccupied states. The photon energy and the work function of a surface define the kinetic energy E_{kin} of photoemitted electrons as

$$E_{kin} = n * \hbar\nu - \Phi - |E_B|, \tag{1.1}$$

where n indicates the number of photons absorbed in the excitation.

A typical photoemission experiment is initiated by the incident light with energy $\hbar\nu$ impinging on a solid surface at an angle of 45° with respect to the sample surface; the excited electrons with energy E_{kin} are ejected into the vacuum, as shown in Figure ??. Electrons emitted within the angle of acceptance of our analyzer are measured with respect

to E_{kin} emission angle θ. The angular information can be converted to parallel momentum, $k_{||}$, of photoelectrons using the formula, [63]

$$k_{||} = \frac{\sqrt{2m_e E_{kin}}}{\hbar} \sin\theta \,. \tag{1.2}$$

The details of how the analyzer works will be discussed in the next chapter

1.3.2 Two-Photon Photoemission Spectra of Alkali Atoms Chemisorbed on Solid Surfaces

As mentioned above, in early published research of alkali atoms on noble metals, only one alkali-induced resonance, was observed for different coverages. In Figure ??(a) this resonance is marked by A.[11] 2PP spectra were measured for all of the alkali atoms (Li through Cs) on Cu(111) surface as a function of coverage. The σ-resonance was found to have the asymptotic energy of ∼2.97 eV above E_F in the zero coverage limit. Its energy decreased with the increasing coverage along with the work function, as can be seen in Figure ??(b).

In 2008, another alkali-induced resonance (π) was predicted by Borisov, and found in 2PP spectra. Figure ??(a) shows the angle-resolved 2PP (AR2PP) spectra of alkali atoms on Ag(111) and Cu(111) surfaces. In AR2PP spectra, the angular intensity distribution of the

σ-resonance could be determined. In the case of the sigma resonance the intensity maximum was at $k_{||}$=0. By contrast, the m=1 has a minimum intensity at $k_{||}$=0 and was predicted to have maxima at emission angle of ±17°, as shown in Figure ??(b). Both of these two features on noble metal surfaces are in agree with m=0 or m=±1 orbital symmetry of ns and np, respectively. Moreover, they pronounced the energy splitting of σ-π is 0.3-0.7 eV, which gives us the initial reference for our research.[13]

Moreover, in addition to the observation of m=±1 resonance, another two studies of alkali atoms on noble metal surfaces from Petek's group contributed efforts on the electronic potentials of the chemisorbed interface.[12, 14] As shown in Figure ??(a), increasing the alkali coverage causes a decrease in the energy of the σ-resonance as well as the work function. The work function changes because alkali atoms introduce a strong surface dipole layer. As introduced in the last section, the dipole layer forms by alkali atoms adsorbed on the metal surface transferring their valence electron to the substrate, leaving the positive cores and their negative image at the surface. The strength of the dipolar field depends on the density of charges. As the density increases the dipolar field introduces an additional surface potential, which causes the work function to decrease. Because the alkali atom resonance energies are referenced with respect to the vacuum level, decreasing the work function also decreases their binding energies with respect to the E_{vac}, shown in Figure ??(a). The relation

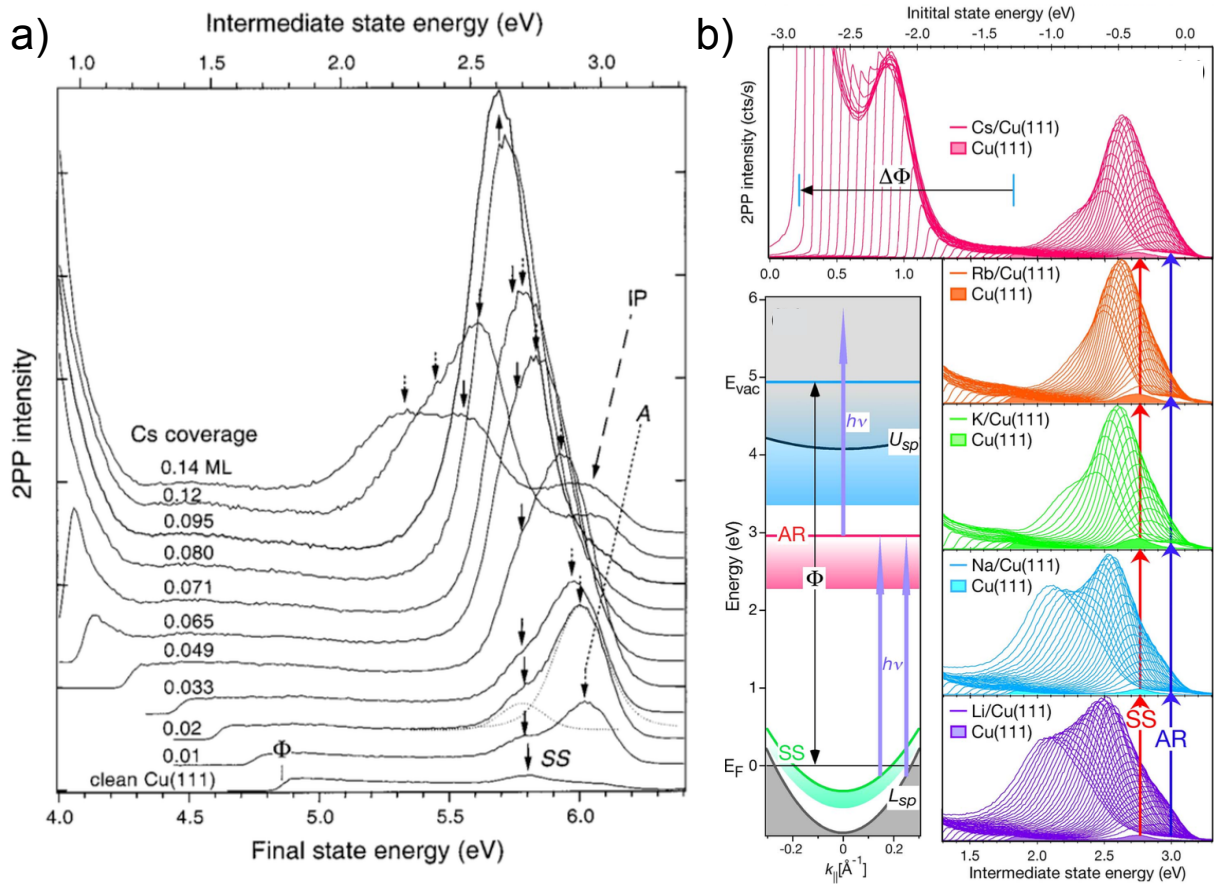

Figure 1.9: **a)** 2PP spectra of Cs-Cu(111) for different Cs coverages.[11] **b)** 2PP spectra for Li through Cs on Cu(111) during continuous alkali-atom deposition up to ∼0.1 ML. The surface-projected band structure is on the left.[12]

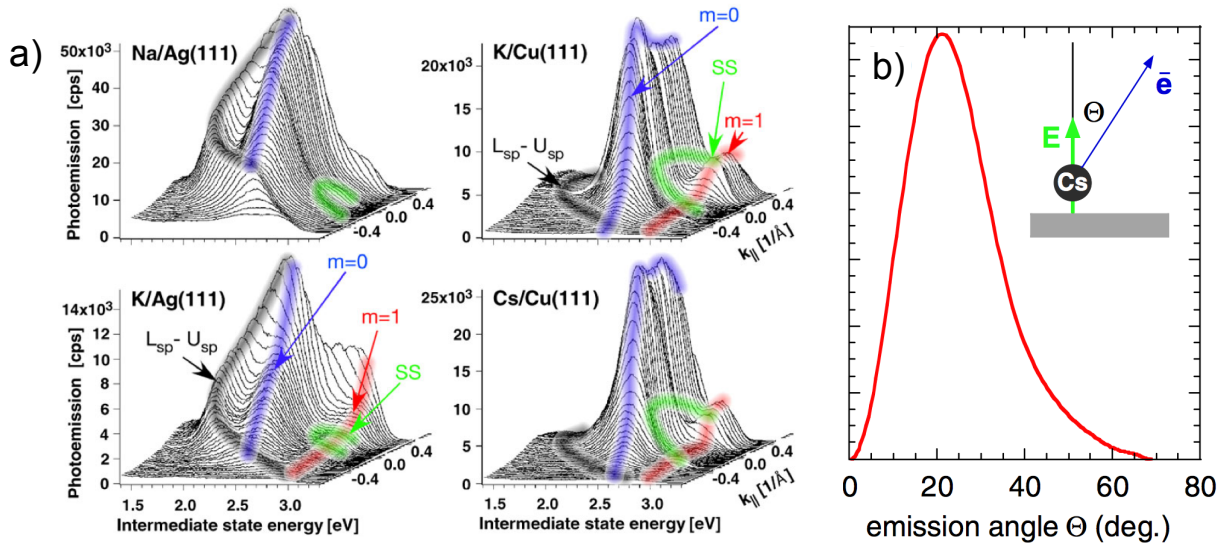

Figure 1.10: **a)** Waterfall plots of 2PP spectra for alkali atoms on Ag(111) and Cu(111) surfaces, plotted against emission wave vector parallel to the surface $k_{||}$. **b)** Calculated angular distribution of the emitted electrons intensity.[13]

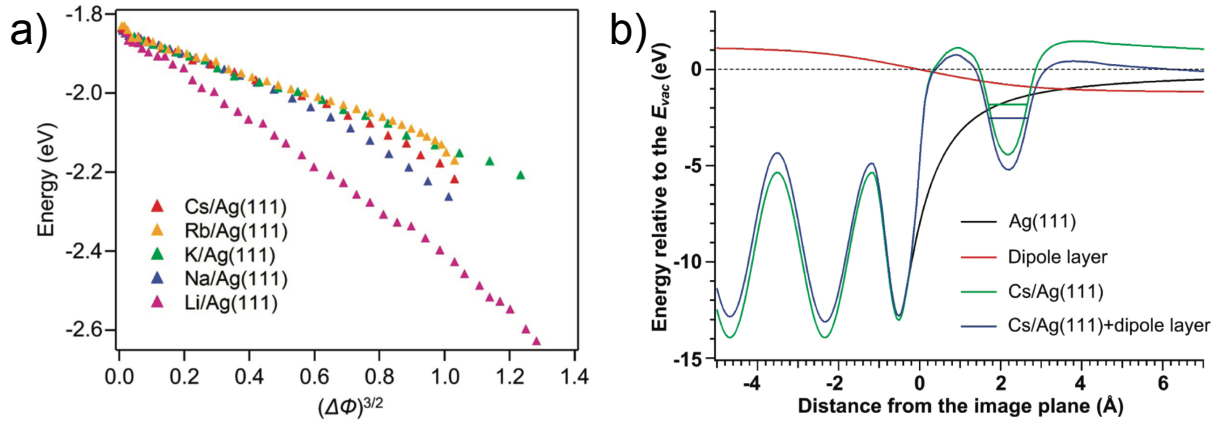

Figure 1.11: **a)** The binding energy of σ-resonance respect to E_{vac} at different coverages plotted against $(\Delta\Phi)^{3/2}$. **b)** The effective potentials experienced by a test charge through the Cs/Ag(111) interface.[14]

between the σ-resonance binding energy and the work function change ($\Delta\Phi$) is calculated to be linear with $(\Delta\Phi)^{3/2}$ by Borisov.[64] This relationship was experimentally confirmed for both Ag(111) and Cu(111). The effective surface potential of Cs/Ag(111) in Figure ??(b) is calculated at the limit of zero coverage.

1.3.3 Electronic Dynamics by Time-Resolved Two-Photon Photoemission

With the application of a Mach-Zehnder Interferometer (MZI) for the generation of identical pump-probe pulses and phase-resolved delay scanning, it became possible to explore the

electron polarization and population dynamics on the femtosecond time scale. This technique has also been applied to the electron dynamics of chemisorbed alkali atoms on metal surfaces. Specifically, the interferometric pump-probe measurements enabled the coherent charge transfer excitation of alkali resonances and the subsequent relaxation dynamics to be investigated. Figure ?? shows the interferometric time-resolved two-photon photoemission (ITR2PP) measurements for the sigma resonance of Cs/Cu(111) that have been recorded for different final state energies at and around the near resonant transition from SS. The 3.08 eV excitation is detuned by 0.17 eV from the SS to sigma resonance transition. Due to the finite dephasing time of the coherent polarization and the detuning from SS to sigma resonance transition, the interferometric two-pulse correlation (I2PC) scans show polarization beating at delays that are marked with arrows in Figure ??(c).

In addition, to observing the details of coherent polarization dynamics, by decomposing the I2PC into ω envelops at different harmonics of the laser frequency, the polarization and population relaxation parameters were derived from the experimental measurements, as shown in Figure ??(a). In [15], Petek obtained the life time of 40 fs for σ-resonance at 50 K and the coherent decay time of 20 fs from $\sigma \rightarrow$ SS. Figure ??(b) gives the plot of final state energy *vs.* lifetime at 33 K for p-polarized excitation of the σ resonance of Cs/Cu(111) system, and the background response with the s-polarized excitation. The result show that

the σ resonance lifetime for Cs/Cu(111) reaches 50 fs at low temperature.

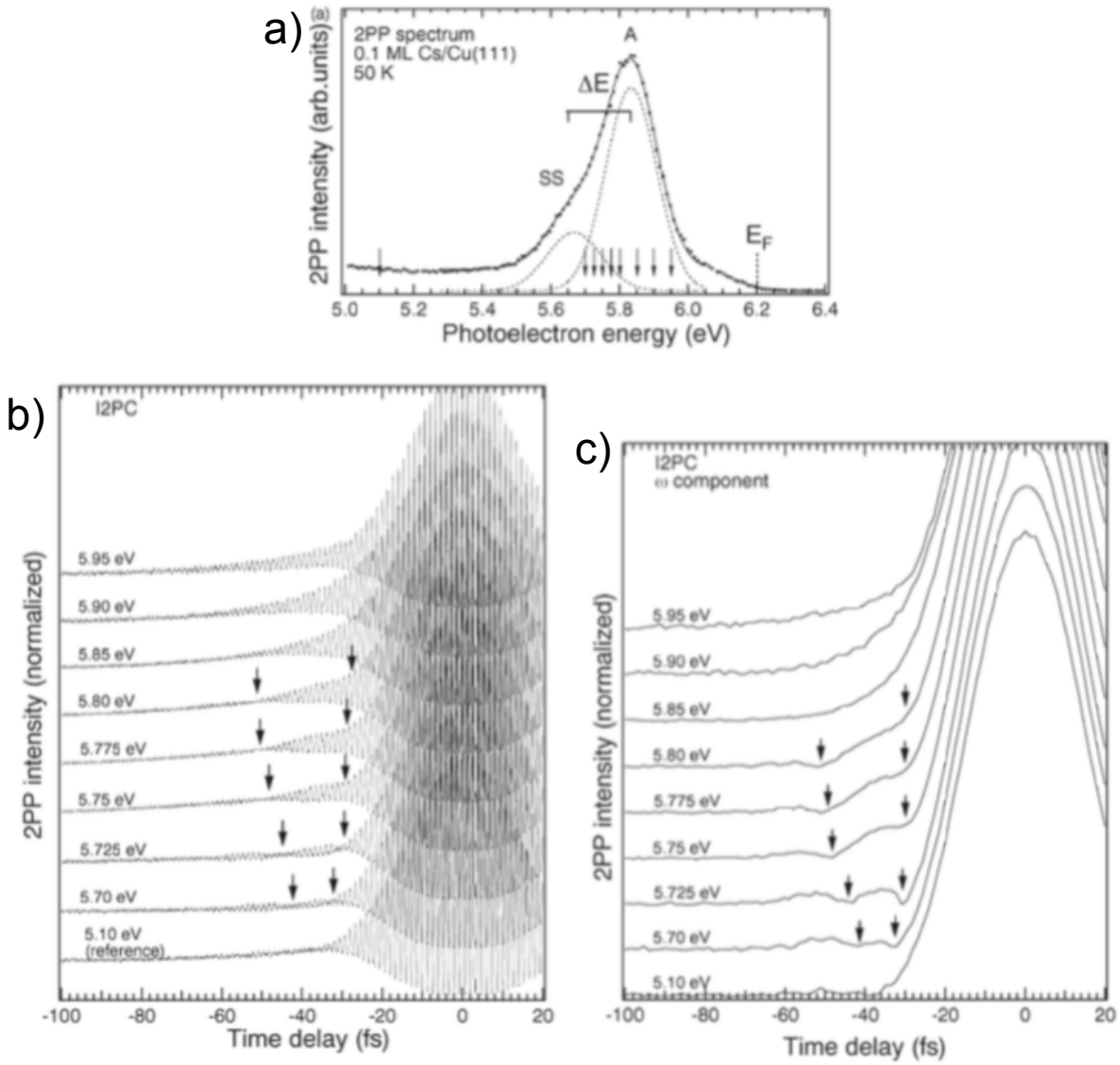

Figure 1.12: **a)** 2PP spectrum of Cs/Cu(111). The arrows are the energies for I2PC scans in **b)** and **c)**. **b)** I2PC scans at different final state energies. **c)** Corresponding ω envelops of **b)**.[15]

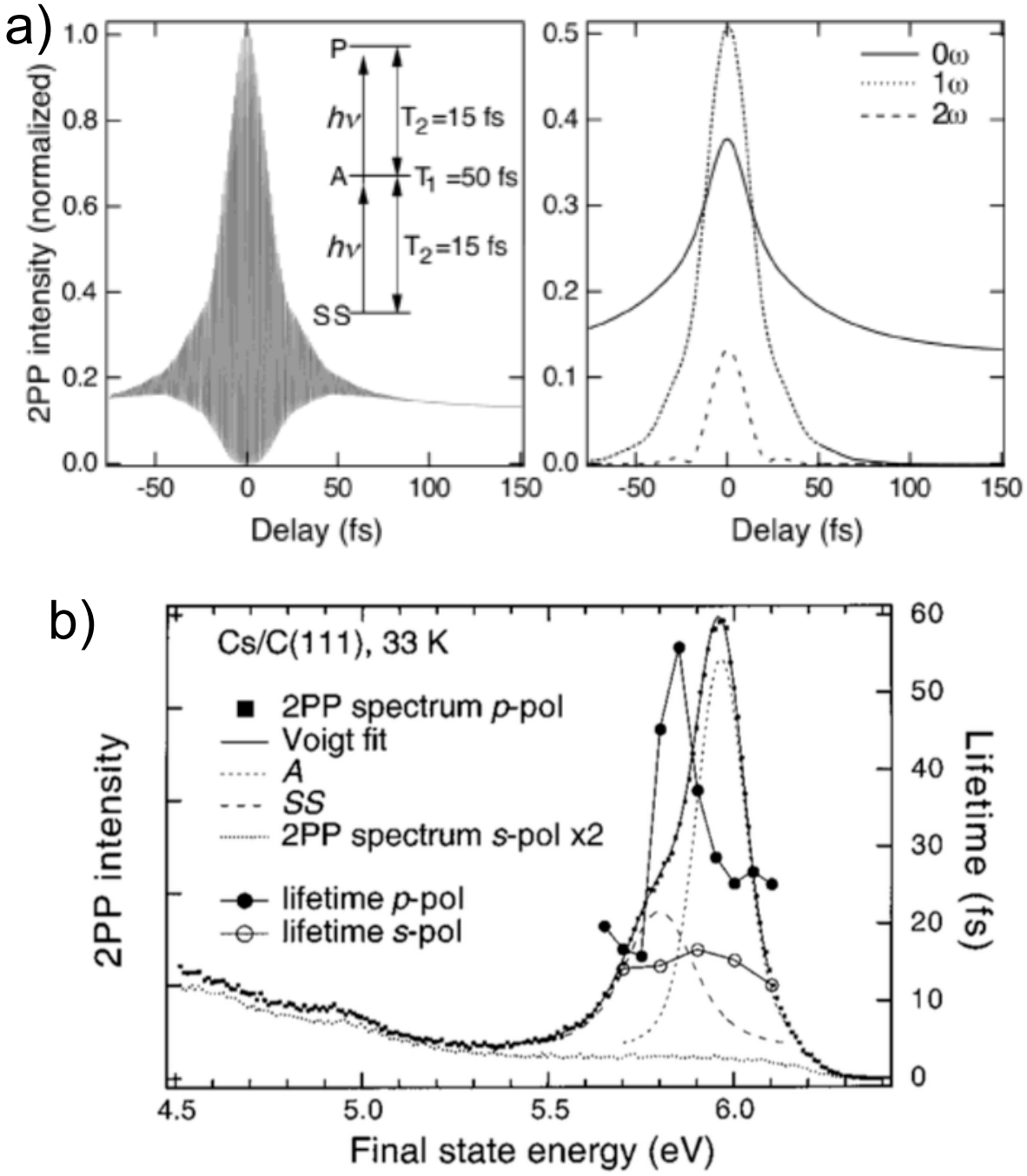

Figure 1.13: **a)** I2PC trace for the near resonant excitation of the Cs antibonding state from the occupied surface of Cu(111) that is calculated by optical Bloch equations for the indicated three-level system. **b)** The 2PP spectra and population decay times for Cs/Cu(111) that are taken with s- and p-polarized excitation at 33 K.[16]

1.4 OUTLINE OF THE DISSERTATION

In the next upcoming chapters I will describe the following topics. Chapter 2 will introduce the experimental apparatus for the measurements; Chapter 3 discusses the fundamental theories of our multi-photon photoemission technique and the implementation in programming language of the optical Bloch equations, which models the electron dynamics mathematically; Chapter 4 presents the experimental, theoretical and computational results on alkali/Ru(0001) system, mostly focusing on the unique features on transition metal surface comparing it to the noble metals; Chapter 5 describes the classic alkali atoms chemisorbed Cu(111) surface with a tunable laser source and two-dimensional energy-momentum imaging, which provides more precise measurements than in the previous work; Chapter 6 describes the extraordinary phenomenom of multielectron process in the charge transfer excitation dynamics of alkali/Cu(111). The last Chapter summarizes the remarkable results presented in this dissertation.

2.0 EXPERIMENTAL APPARATUS

In this chapter I will introduce the experimental apparatus for the multiphoton photoemission (mPP) measurements. The entire apparatus consists of three main parts: the non-collinear optical parametric amplifier (NOPA) system, a Mach-Zehnder interferometer (MZI) for the time-resolved multiphoton photoemission spectra (TR-mPP) and a UHV photoemission apparatus consisting of a Specs Phoibos 100 electron spectrometer equipped with a 3D-DLD delay-line photoelectron counting detector.

2.1 NOPA SYSTEM

2.1.1 Introduction of NOPA setup and mechanism

The photon induced excitations on the solid-state and systems by pulsed lasers have been interesting for decades, and the ultrafast lasers giving the pulses as short as 15 fs make many

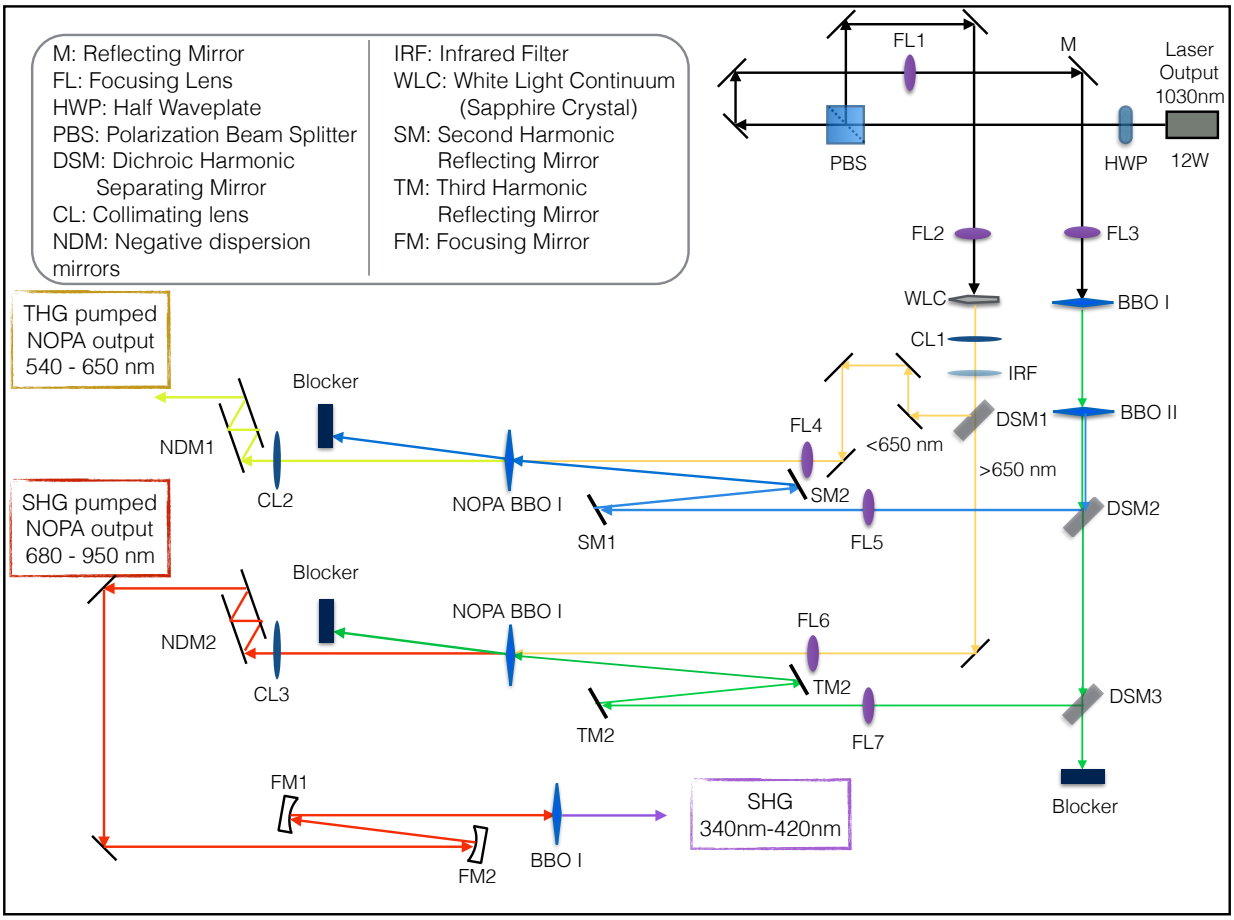

Figure 2.1: The NOPA system setup pumped by a commercial fiber based Yb:doped oscillator-amplifier system.

fast process possible to observe nowadays. Our NOPA system is pumped by a femtosecond fiber laser system. Figure 2.1 shows the optical layout for the entire NOPA system for TR-mPP measurements. The self-made NOPA is pumped by a Clark MXR Impulse Yb doped fiber-laser oscillator amplifier system. The NOPA consists of two separate arms for independent generation of two separate outputs with green and UV pumping. The output of the pump laser pulse provides ∼1030nm light with 12.2W average power at a repetition rate of 1.25 MHz and 250 fs pulse width. The polarization of the fiber laser beam is controlled by a $\lambda/2$ plate to vary the fraction of *p*- and *s*-polarized light before entering a polarizing beam splitter. The pump laser is then split by a polarizing beam splitter with ∼80% used as the NOPA pump and the remaining ∼20% for white light generation.

To be useful for NOPA pumping, the pump light is first frequency doubled in a Type I Beta barium borate (BBO) second harmonic generation (SHG) crystal, generating ∼515nm, pump light. Next, the SHG and fundamental beams are mixed in a Type II BBO crystal to produce the third harmonic (THG) UV, ∼343nm, pump light. The white light genertion beam is focused onto a sapphire crystal to generate white light through the process of self-phase modulation (denoted by yellow line in the Figure 2.1). The white light is split into two spectral regions for each NOPA arm with a dichroic mirror; light above 670nm is used with the SHG pump, and that below 680 nm is used THG light. Each white continuum

is combined with the respective pump beam in separate BBO crystals to generate tunable output as shown in the Figure 2.1.

The process of nonlinear optical parametric amplification is described in Figure 2.2. The nonlinear interaction with the pump light amplifies a part of the white light continuum to generate the signal and idler beams. When the phase matching condition is satisfied for one part of the white light spectrum it is amplified by the pump beam.

The phase-matching condition for white light amplification is:

$$\omega_1 n_1 \sin\theta_1 = \omega_2 n_2 \sin\theta_2 \tag{2.1}$$

$$\text{and } \omega_1 n_1 \cos\theta_1 + \omega_2 n_2 \cos\theta_2 = \omega_3 n_3 \tag{2.2}$$

where θ_1 is the angle between beam 1 and beam3 and θ_2 is the angle between beam 2 and beam 3 in Figure 2.2.

The wavelength of the laser is tunable by adjustment of two parameters. The angle between the pump and white light beams adjusts the phase matching condition for efficient amplification. In addition, the white light emerging from the sapphire crystal is strongly chirped. Therefore, to optimize amplification at a particular wavelength requires the adjustment of the delay between the white light and pump beams. The beam generated by NOPA

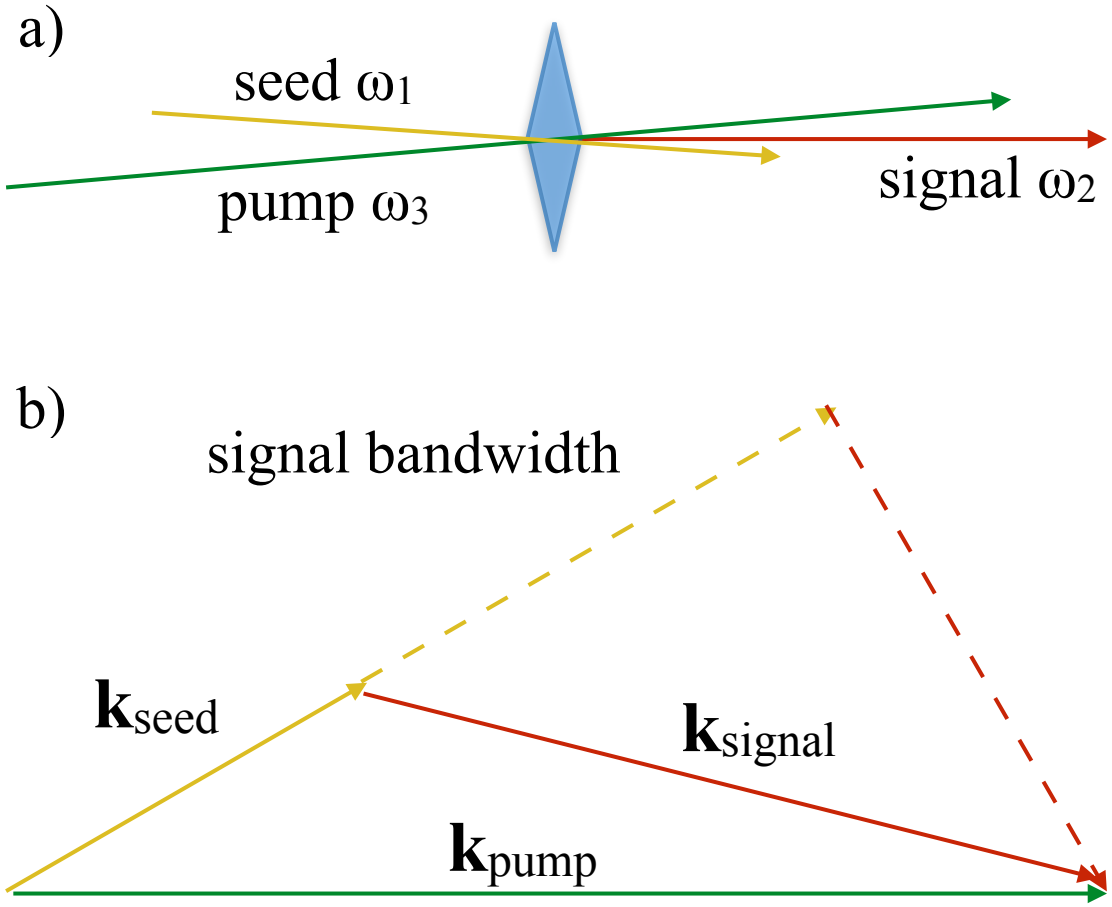

Figure 2.2: The noncolinear phase matching for the NOPA amplification. **a)** Amplification of seed light by BBO crystals shown in Figure 2.1 and **b)** angle adjustment for different frequency under the phase matching condition.

system might be directly guided into the chamber to excite the sample surfaces. Moreover, we further extend our laser wavelength range by frequency doubling the light by using BBO crystals with the thickness of 800 μm to obtain light in the UV-Violet range (340-420 nm).

2.1.2 White Light Generation

The white light generation occurs predominantly by a third-order nonlinear process called Optical Kerr Effect (OKE). OKE is a consequence of the dependence of the index of refraction n on the intensity I of the incident light:

$$n(I) = n + n_2 I \,, \tag{2.3}$$

where n_2 is related to the second-order nonlinear susceptibility. When light passes through a medium with a third-order nonlinear response, a phase shift arises due to the OKE. The phase shift is given by:

$$\Delta\phi(t) = 2\pi n_2 \frac{l}{\lambda_0} I(t) \,, \tag{2.4}$$

where l is pathlength through the medium, P is the laser power and S is the cross-sectional area. Then, the time derivative of the nonlinear phase shift produces a frequency shift of

the output beam:

$$\Delta\omega = \frac{\partial\phi(t)}{\partial t} = 2\pi n_2 \frac{l}{\lambda_0} \frac{\partial I(t)}{\partial t} \,. \tag{2.5}$$

2.1.3 Second and Third Harmonic Pump Light

For the Type I BBO crystal, the refractive index ellipsoid is shown in Figure 2.3a and the generation process in Figure 2.3c. By traveling through the Type I BBO crystal, the input beam of frequency ω with polarization "o" gets frequency doubled to 2ω with polarization "e". With the propagation angle θ, the phase matching condition should be satisfied. For the Type II BBO in Figure 2.3b, it is required after the Type I BBO crystal to obtain the third harmonic pump light, since in the collinear three-wave mixing, the phase-matching condition is $k_1 + k_2 = k_3$. In Figure 2.1, the pump beam of the second and third harmonic is separated by a dichroic mirror same as in the white light path.

2.1.4 Mach-Zendner Interferometer (MZI) System

In order to measure the time dependence of the ultrafast surface processes, we also performed interferometric time-resulved multiphoton photoemission measurements (ITR-mPP). Time-resulved measurements can provide the information on the quasiparticle dynamics in the

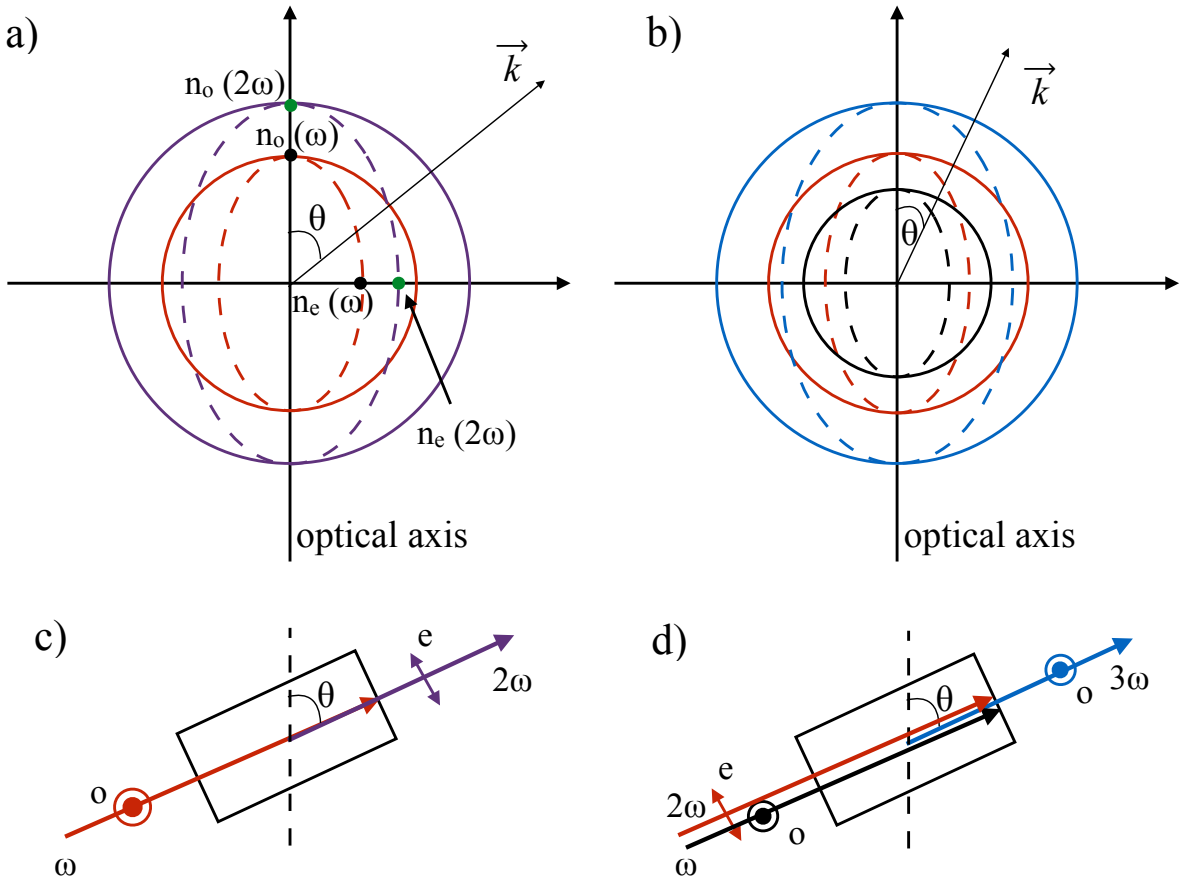

Figure 2.3: **a)** and **c)** are the phase matching and frequency doubling for Type I BBO crystal. **b)** and **d)** are for the Type II BBO crystal.

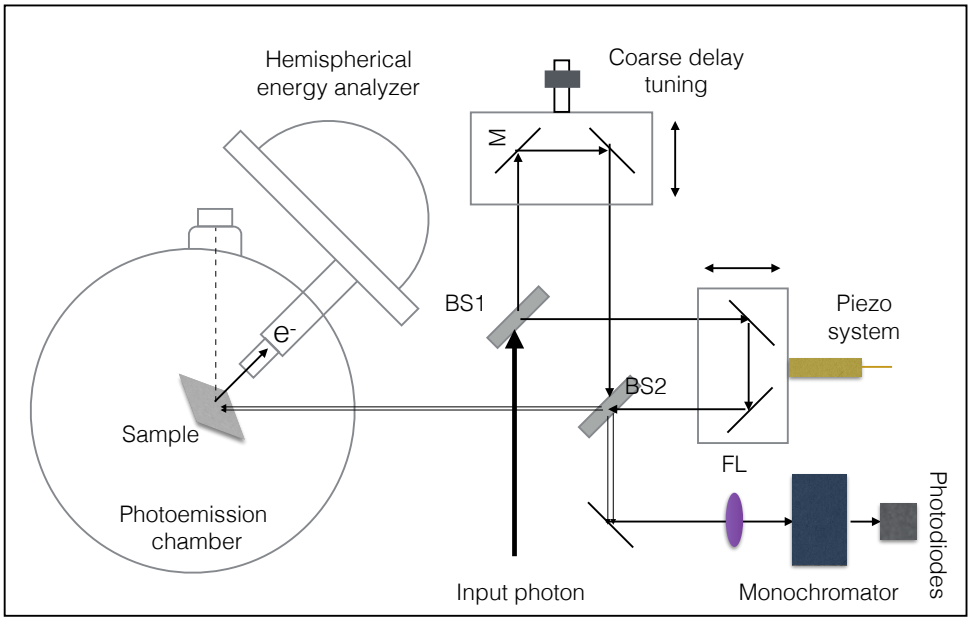

Figure 2.4: The MZI setup

time-domain. Compared with two-color time-resolved photoemission measurements, we can obtain information on the light-induced polarization that is excited in the sample. This will be discussed in detail in the next chapter.

The laser beam generated from the NOPA system is directed into the MZI as shown in Figure 2.4. With a 50% beam splitter, the beam is split into two different paths until they reach the second beam splitter. The second beam-splitter again splits the two beams into two different paths, one of which is directed to excite the sample and the other is directed through a monochrometer to a photodiode. Thus, the beam going into the chamber and

the beam going to the photodiode have equal intensities. When the two pulses overlap at the second beam splitter, they are actually recombined, with most intensity going into one or the other path depending on the relative phase of the pulses. The pump-probe delay is scanned with a piezoelectric actuator with a typical scanning at a step interval of ∼0.1 fs.

2.2 CHARACTERIZATION OF ULTRAFAST PULSES

In this section I will introduce some theoretical descriptions of laser pulse and practical methods to align the beam for our experimental measurements.

2.2.1 Autocorrelation of a Gaussian laser pulse

In order to characterize the laser pulses used for our experiments we perform autocorrelation measurements. The purpose of such measurements is to optimize the dispersion compensation so as to obtain the minimum pulse duration at the sample. This involves determining the number of reflections from the dispersion compensating chirped mirrors. We also need to characterize the pulses to extract information on the electron dynamics in the sample.[17]

The minimum pulse duration that we can obtain is defined by the uncertainty relation:

$$\Delta t \Delta \omega = 4ln2\,, \tag{2.6}$$

where $\Delta\omega$ is the full width at the half maximum (FWHM) of the spectral intensity profile $I(\omega)$. Usually it is easy to use the frequencies ν instead of the circular frequencies ω, and then the uncertainty relation, known as the time-bandwidth product, can be written as:

$$\Delta t \Delta \nu = \frac{2ln2}{\pi} = 0.441\,. \tag{2.7}$$

The spectral intensity profile $I(\omega)$ can be obtained from our commercial optical spectrometer directly. With the time-bandwidth product, we can calculate the estimated minimum pulse duration of the laser beam by assuming a pulse with Gaussian shape. This approach is useful to determine the theoretically possible pulse duration when tuning the laser, but it does not include the effects of dispersion.

In Figure 2.5, I show a typical laser spectrum obtained by the spectrometer. By Gaussian fitting, we can obtain the FWHM $\Delta\nu \approx 24 \times 10^{12} s^{-1}$, which implies a bandwidth-limited Gaussian pulse of Δt=18 fs.

The autocorrelation (AC) method is a more accurate way to measure the duration of a

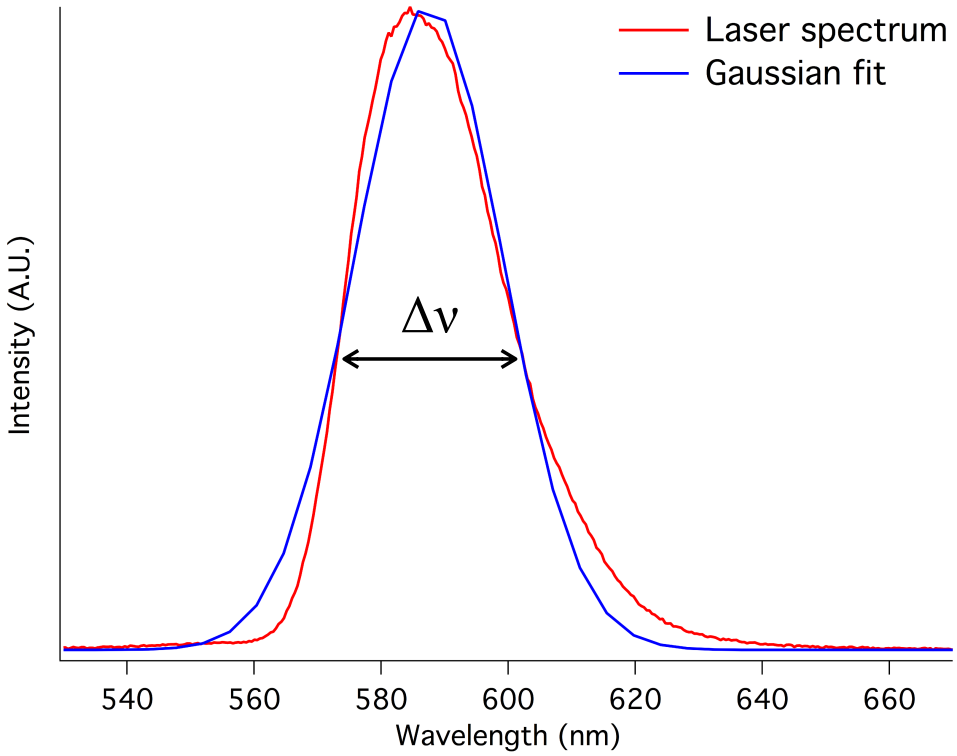

Figure 2.5: Gaussian fit for the laser spectrum at 586nm

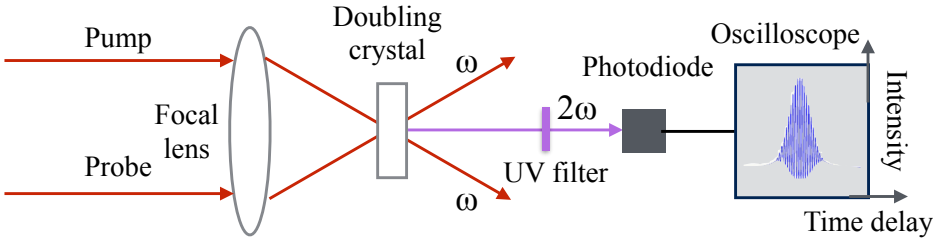

Figure 2.6: The principle for second order autocorrelation measurement.

laser pulse. For this purpose we use our MZI setup to scan the time delay between pump and probe pulses.

Figure 2.6 shows the basic principle of the second-order AC measurement. Usually we need to characterize the temporal laser field intensity $I(t) = \langle \mathbf{E}(t) \cdot \mathbf{E}^*(t) \rangle$. By defining the electric field as:

$$\mathbf{E}(t) = A(t)e^{i\Phi(t)}e^{i\omega t}\,. \tag{2.8}$$

The first order AC is a function of the time delay τ:

$$S_1(\tau) \;\; = \int_{-\infty}^{\infty} |\mathbf{E}(t) + \mathbf{E}(t-\tau)|^2 \mathrm{d}t \;\; = 2\int_{-\infty}^{\infty} \mathrm{d}t + 2\int_{-\infty}^{\infty} E(t)E(t-\tau)\mathrm{d}t\,. \tag{2.9}$$

It only provides information on the pulse spectrum. To get information on the pulse duration, we need the second or high order AC. The second order AC is given by:

$$S_2(\tau) = \int_{-\infty}^{\infty} |[\mathbf{E}(t) + \mathbf{E}(t-\tau)]^2|^2 \mathrm{d}t, \tag{2.10}$$

In my experiment, the second and higher-order AC functions could be obtained by using multiphoton photoemission processes; we will give a detailed discussion later.

The Wiener-Khintchine theorem states that the Fourier transformation of the AC of the electric field yields the spectral density, which is proportional to the spectral intensity $I(\omega)$. Thus the second-order AC in Eq. 2.10 can be decomposed into:

$$S_2(\tau) = \frac{1}{S_0}(S_{0\omega} + S_{1\omega} + S_{2\omega}), \tag{2.11}$$

with

$$S_0 = \int_{-\infty}^{\infty} A^4(t) \mathrm{d}t, \tag{2.12}$$

$$S_{0\omega} = \int_{-\infty}^{\infty} [A^4(t) + 2A^2(t)A^2(t-\tau)] \mathrm{d}t, \tag{2.13}$$

$$S_{1\omega} = 2Re\{e^{i\omega\tau} \int_{-\infty}^{\infty} A(t)A(t-\tau) \times [A^2(t) + A^2(t-\tau)] e^{i[\Phi(t-\tau)-\Phi(t)]} \mathrm{d}t\}, \tag{2.14}$$

$$S_{2\omega} = Re[e^{i2\omega\tau} \int_{-\infty}^{\infty} A^2(t)A^2(t-\tau) \times e^{i2[\Phi(t-\tau)-\Phi(t)]}\mathrm{d}t], \tag{2.15}$$

where $A(t)$ is the temporal amplitude.

As can be seen from Eq. 2.12-2.15 the second order AC has components that vary with the envelope of the laser pulse, the fundamental frequency and its second harmonic. $S_{0\omega}$ is the intensity correlation, which is obtained by averaging the oscillations; it is the phase average envelope. From Eq. 2.13 the intensity AC has a peak-to-baseline ratio of:

$$\frac{S_{0\omega}(0)}{S_{0\omega}(\infty)} = \frac{\int_{-\infty}^{\infty} 3A^4(t)\mathrm{d}t}{\int_{-\infty}^{\infty} A^4(t)\mathrm{d}t} = \frac{3}{1}. \tag{2.16}$$

$S_{1\omega}$ is a sum of two symmetric cross-correlations. $S_{2\omega}$ corresponds the AC of the second harmonic field and it is related to the second harmonic spectral intensity. Adding these three components together, the peak to baseline ratio of AC_2 is 8:1.

$$\frac{S_2(0)}{S_2(\infty)} = \frac{\int_{-\infty}^{\infty}(E+E)^4 dt}{\int_{-\infty}^{\infty} E^4 dt + \int_{-\infty}^{\infty} E^4 dt} = \frac{16\int_{-\infty}^{\infty} E^4 dt}{2\int_{-\infty}^{\infty} E^4 dt} = \frac{8}{1}\,. \tag{2.17}$$

With the same approach, it is easy to show that for the third-order autocorrelation (AC_3), the peak to baseline ratio is 32:1. These ratios are very helpful in the experiments to

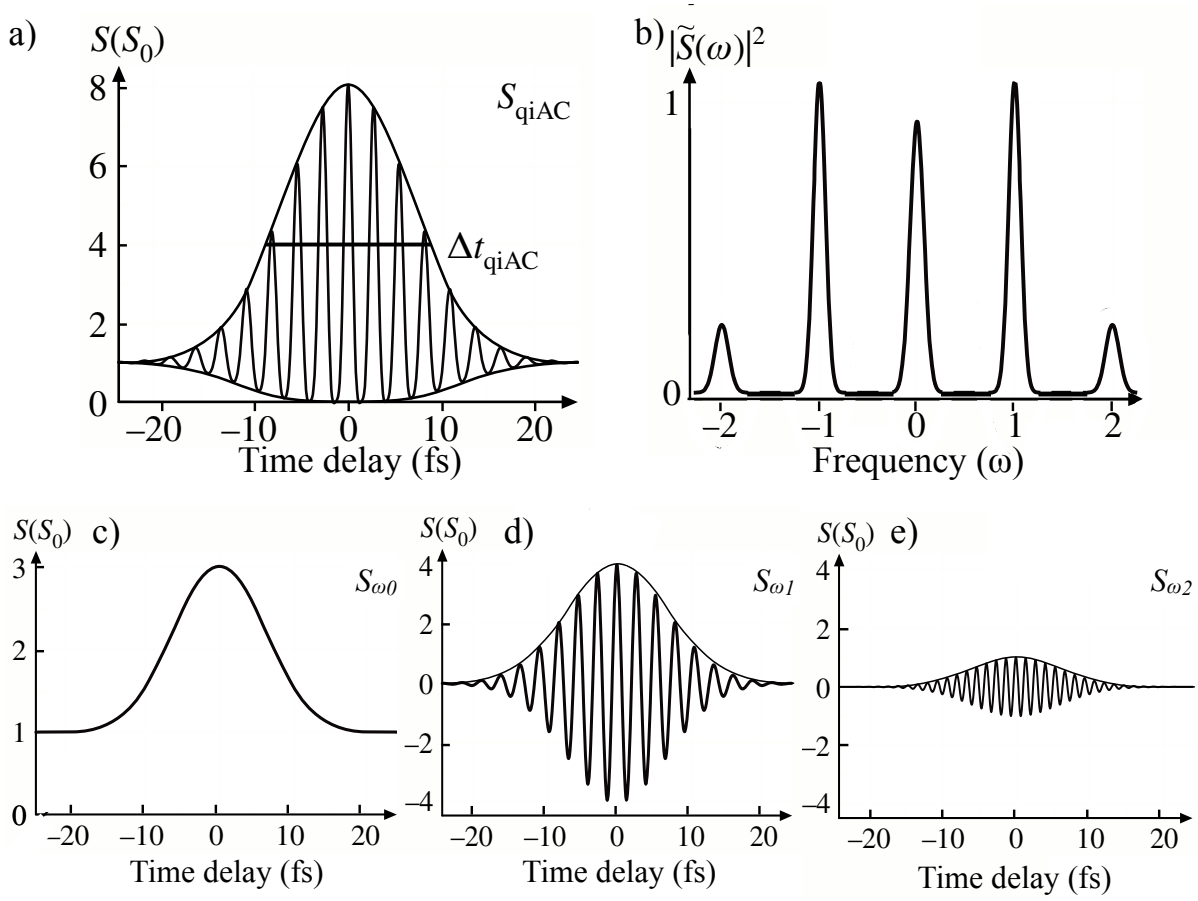

Figure 2.7: **a)** Second-order interferometric autocorrelation. **b)** The Fourier transform of **a)**. **c)-e)** the isolated components at different orders of the laser frequency.[17]

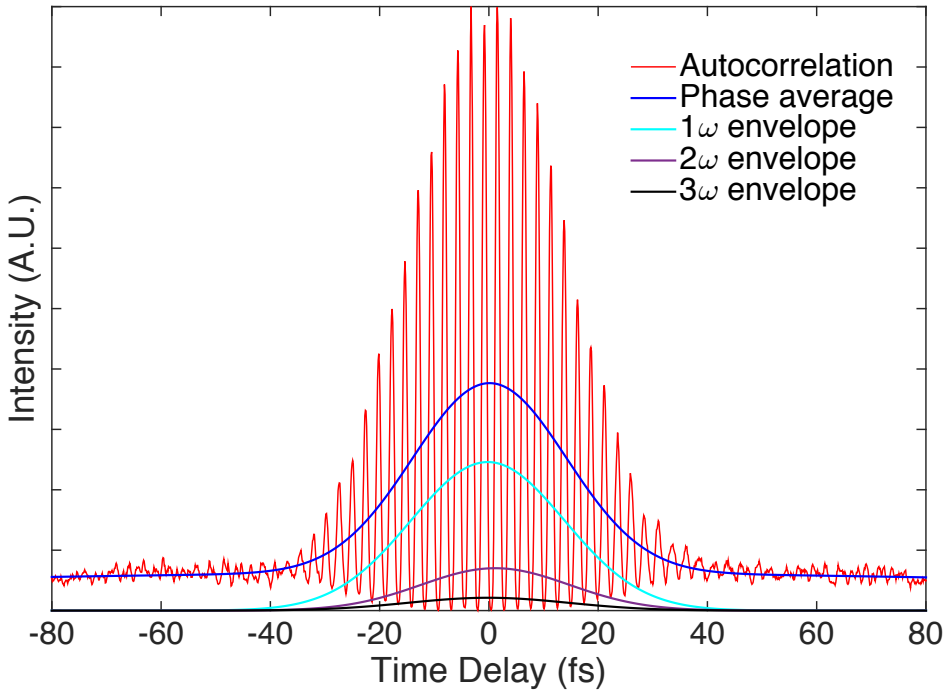

Figure 2.8: Third-order autocorrelation measured at 580nm by recording the 3PP signal a function of pump-probe time delay.

check if the interferometer is aligned properly or not. Bad alignment gives smaller ratio than the theoretical. The pulse duration can be estimated from the width of the AC function. For example, for a Gaussian pulse the width is obtained from ratio of $\Delta t_{AC}/\Delta t = 1.6963$, where Δt_{AC} is the FWHM of the interferometric the AC_2 signal (Figure 2.7a). More detailed analysis for interferometric scan will be described in the next chapter.

2.2.2 Dispersion compensation

As mentioned in the last section, the duration of the pump laser fundamental is ~250 fs, and therefore the white light, and the second and third harmonic NOPA pump pulses are comparably broad. Consequently, the NOPA output pulses are equally long, but their output is chirped. Moreover, other optics and even air in the optical beam path introduce more dispersion.

Dispersion can be described as a relation between the wave frequency or the wave number of an electromagnetic field propagating through a dispersive medium, $k(\omega) = \omega n(\omega)/c$, where $n(\omega)$ is the frequency dependent index of refracion. By applying the Taylor's expansion about the central frequency, we can express the frequency dependent wave number as

$$k(\omega) = k(\omega_l) + \frac{\mathrm{d}k}{\mathrm{d}\omega}|_{\omega_l}(\omega - \omega_l) + \frac{1}{2}\frac{\mathrm{d}^2k}{\mathrm{d}\omega^2}|_{\omega_l}(\omega - \omega_l)^2 + \frac{1}{6}\frac{\mathrm{d}^3k}{\mathrm{d}\omega^3}|_{\omega_l}(\omega - \omega_l)^3 + ...$$
$$= k_l + \dot{k_l}(\omega - \omega_l) + \frac{1}{2}\ddot{k_l}(\omega - \omega_l)^2 + \frac{1}{6}\dddot{k_l}(\omega - \omega_l)^3 + ... \tag{2.18}$$

Considering the first order dispersion, the electric field of the laser pulse is

$$E^{(1)}(\omega) = A \cdot \exp[i\omega\frac{Ln}{c} - k(\omega)L] = A \cdot \exp[-i(k_l - n \cdot \frac{\omega}{c}) + \dot{k_l}(\omega - \omega_l)L]\,. \tag{2.19}$$

By applying Fourier transform with respect to the frequency ω, we obtain the time domain expression for the field,

$$E^{(1)}(t) = A \cdot \exp[i\omega_l(t - (\frac{k_l}{\omega_l} - \frac{n(\omega)}{c})L)] \cdot \delta[t - (\dot{k_l} - \frac{n(\omega)}{c})L]\,. \tag{2.20}$$

From Eq(2.20) we can conclude that the first-order dispersion term only gives a trivial time delay given by

$$\Delta\tau = \omega \cdot \frac{\mathrm{d}n(\omega)}{\mathrm{d}\omega}|_{\omega_l}\frac{L}{c}\,. \tag{2.21}$$

To determine the effect of the second-order dispersion with the Gaussian pulse written as $A(t) \propto \exp[-(t/T_0)^2/2]$, the electric field is given by

$$E^{(2)}(\omega) = A(\omega) \cdot \exp[-\frac{i}{2} \cdot \ddot{k}_l(\omega - \omega_l)^2 L], \tag{2.22}$$

where the frequency dependent amplitude is

$$A(\omega) = \int A(t) \cdot \mathrm{e}^{-it(\omega-\omega_l))} \mathrm{d}t = \exp[-\frac{1}{2}(\omega - \omega_l)^2 T_0^2]\,. \tag{2.23}$$

Thus, the frequency dependent spectral amplitude with second-order dispersion is

$$E^{(2)}(\omega) = \exp[-\frac{1}{2}(\omega - \omega_l)^2 T_0^2 (1 + i\frac{\ddot{k}_l}{T_0^2} L)] \approx \exp[-\frac{1}{2}(\omega - \omega_l)^2 T_0^2 (1 + i\frac{\ddot{k}_l}{2T_0^2} L)^2]\,. \tag{2.24}$$

Assuming that the second order dispersion term, known as the group velocity dispersion (GVD), is very small, we can approximate $(1 + i\frac{\ddot{k}_l}{2T_0^2} L)^2 \approx 1 - i\frac{\ddot{k}_l}{T_0^2} L$. Then the Fourier

transformation of the $E^{(2)}(\omega)$ gives

$$E^{(2)}(t) = \exp[-\frac{1}{2}(\frac{t}{T_0})^2(1 - i\frac{\ddot{k}_l}{T_0^2}L)] = \exp[-\frac{1}{2}(\frac{t}{T_0})^2(1 + ia)]\,. \tag{2.25}$$

Here we have introduced the parameter a, corresponding to the linear chirp of a Gaussian pulse due to the GVD, which can be expressed as:

$$a = -\frac{L}{T_0^2}\ddot{k}_l = -\frac{L}{cT_0^2}[\omega_l \frac{\mathrm{d}^2 n(\omega)}{\mathrm{d}\omega^2}|_{\omega_l} + 2\frac{\mathrm{d}n(\omega)}{\mathrm{d}\omega}|_{\omega_l}]\,. \tag{2.26}$$

Including corrections up to second-order, the total electrical field of a chirped pulse is

$$E^{(1,2)}(t) \approx \exp[-\frac{1}{2}(\frac{t - \delta\tau}{T_0})^2(1 + ia)]\,. \tag{2.27}$$

As can be seen from Eq. 2.27, the effect of the linear chirp is to increase the pulse length. In order to perform experiments with optimal pulses we need to compensate for the positive chirp.

The dispersion compensation is performed by introducing two chirped (negative dispersion) mirrors in the optical path. This makes it possible to compensate for the pulse spreading due to the generation and propagation through optical components, like crystals, lenses, and beam splitters, as shown in Figure 2.1. The chirped mirrors are designed to

provide both a negative GVD as well as the third order compensation by reflection of the laser beam from the mirror surface. The number of reflections from a pair of chirped mirrors is varied until the shortest pulse is obtained.

The appropriate number of reflections is determined experimentally by measuring the pulse second- (2PP) or third-order (3PP) autocorrelation function. Using the MZI setup for interferometric scanning, the AC can be measured for different wavelengths by recording the mPP signal from the molybdenum sample holder at the same location as the sample in ultrahigh vacuum (UHV) chamber. Figure 2.8 shows a third-order AC measured from the sample holder for the laser wavelength of 580 nm. The envelopes of the AC signal for different harmonic components of laser frequency are shown in the Figure 2.8. By fitting the AC we can estimate the pulse duration to be $\sim 20fs$. Such AC measurements are performed to minimize the pulse duration, as well as for calibration of 2PP and 3PP interferometric measurements from experimental samples.

2.3 HEMISPHERICAL ENERGY ANALYZER (HSA) WITH A DELAYLINE DETECTOR (DLD)

In this section, we describe our analyzer with a delayline detector, including the schematic diagrams, the basic principles of operation and some specifications.

2.3.1 Hemispherical Energy Analyzer

The SPECS PHOIBOS hemispherical electrostatic energy analyzer with the Delayline Detector is one of the most important parts of our experimental apparatus. A muti-element, two-stage transfer lens, which is integrated into the analyzer, can be operated in different modes for our angle-resolved (AR) studies and all the modes can be set electronically. The Slit-Orbit mechanism and the multi-mode lens make the sampling area of the analyzer and the acceptance angle area selectable.

The standard working distance of 40 mm and 44^o conical shape of the front part of the lens are shown in Figure 2.9. With the sample being in the focal plane of the lens system, the electrons exciting from the sample are imaged on to the entrance slit S_1, which is marked as *Iris* in Figure 2.9. Then in the lens stage, the electrons pass through the intermediate image before they are focused onto the input slit S_1 of the hemispherical capacitor (Figure

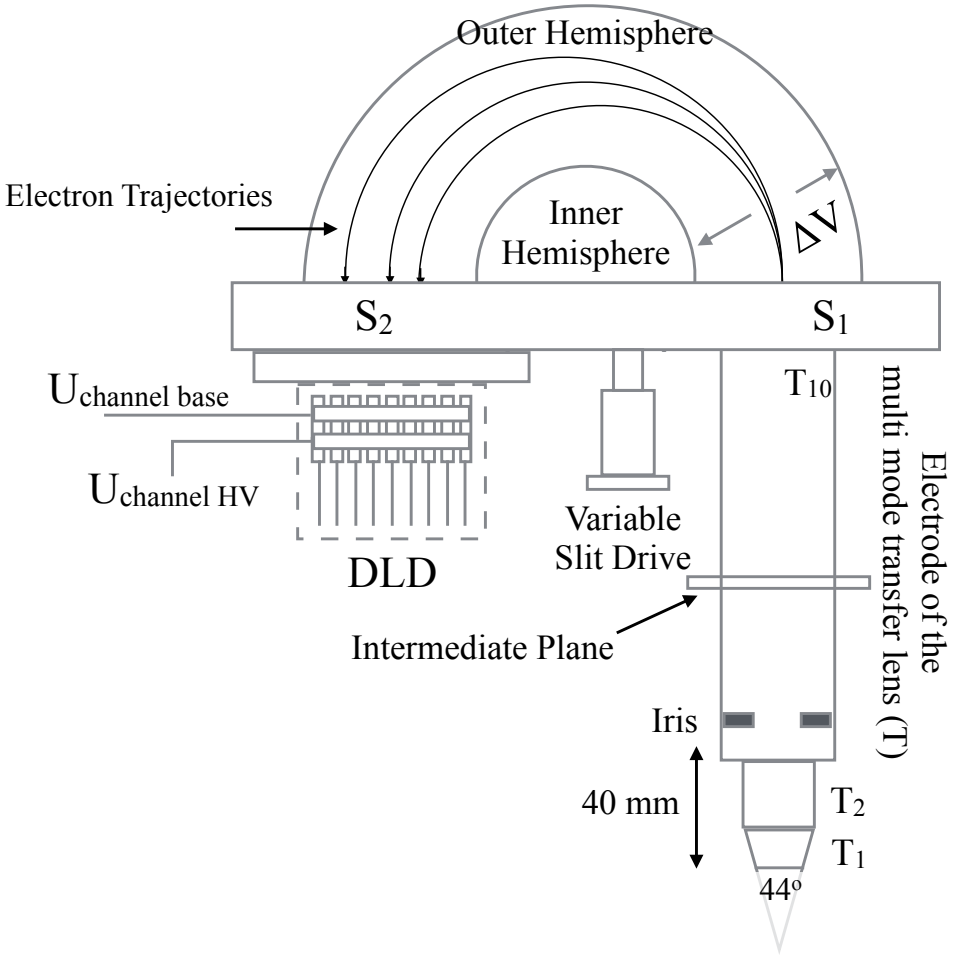

Figure 2.9: The simplified diagram of the hemispherical energy analyzer with the delay-line detector

2.9). At S_1 the electrons are retarded by the energy difference between the nominal kinetic energy E_{kin} and the nominal pass energy E_{pass}.

The electrons entering the HSA through the entrance slit S_1 are deflected into elliptical trajectories by the radial electrical field between the inner hemispheres R_{IN} and the outer hemisphere R_{out}. The entrance slit S_1 and exit plane S_2 are centered on the mean radius R_0:

$$R_0 = \frac{R_{in} + R_{out}}{2} = 150mm. \tag{2.28}$$

For a fixed electrical field gradient, only the electrons with kinetic energies in a certain energy interval are able to pass through the full deflection angle from the entrance slit to the exit plane. Those electrons with higher kinetic energy are deflected into the outer hemisphere, while the electrons with lower kinetic energy crash into the inner hemisphere. The electrons, which are able to pass through the hemisphere, have the nominal pass energy E_{pass}:

$$E_{pass} = (-q)k\nabla V, \tag{2.29}$$

where q is the charge, ΔV is the potential difference applied between the hemispheres

(marked in Figure 2.9), and k is the calibration constant,

$$k = \frac{R_{inner}R_{out}}{2R_0(R_{out} - R_{inner})} = 0.9375\,. \tag{2.30}$$

If the HSA has the half angle α in the dispersion direction, the HSA resolution ΔE_{an} is given by

$$\frac{\Delta E_{an}}{E_{pass}} = \frac{S}{2R_0} + \frac{\alpha^2}{4}, S = \frac{S_1 + S_2}{2} \tag{2.31}$$

Here S=(S_1+S_2)/2 is a constant for the analyzer. The integral signal intensity I of the measurement is proportional to product of the accepted solid angle Ω_S, the accepted sample area A_S and the HSA resolution ΔE_{an}:

$$I \sim \Delta E_{an}\Omega_S A_S = \Delta E_{an}\Omega_0 A_0 \frac{E_{pass}}{E_{kin}} \sim \frac{E_{pass}^2}{E_{kin}} \tag{2.32}$$

in which Ω_0 and A_0 are the values of the acceptances of the HSA and they are constant for certain analyzer.

2.3.2 Slit-Orbit Mechanism

The slit-orbit mechanism (marked as slit drive in Figure 2.9) is used to manually change the entrance and exit apertures of the analyzer. Figure 2.10 shows the internal structure of

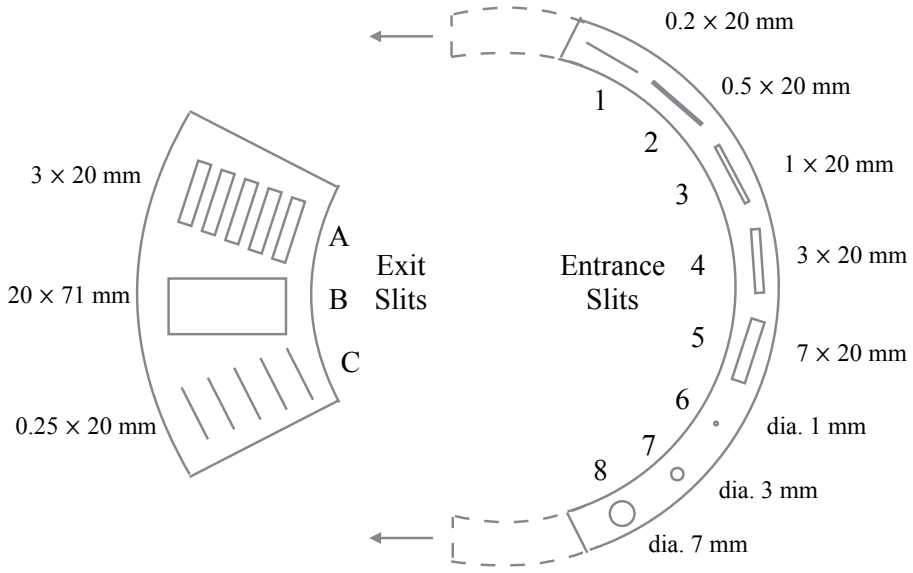

Figure 2.10: The entrance and exit slit rings. The arrows give the possible rotating directions to get different combination of entrance and exit slits.

the slit drive with the dimensions of every slit marked. Different combination of entrance and exit slits defines the analyzer energy resolution with the matching angular spread, as described in Eq(2.32). Thus for a given energy resolution and a required acceptance angle, we should choose the largest possible slit, which leads to the highest possible counts and a good signal to noise ratio. In our experiment, we generally use 2 or 3 for the entrance slit and B as the exit, and under this setup, the energy resolution of the spectrum is ∼0.16 eV.

2.3.3 Introduction of DLD

At the exit of the analyzer we use a delayline detector to recored the 2D distribution of photoelectrons. A DLD is made of a microchannel plate array for pulse amplification and an in-vacuum readout unit, consisting of a meander structured wire delayline, and each hitting position contains a fast data acquisition unit which transmits the electron counts to an electric signal (Figure 2.11). The DLD anode has two meanders. One is rotated by 90 degree with respect to the other one, and both are isolated from each other. The microchannel plate (MCP) stack as shown in Figure 2.11 amplifies incoming electrons by at least 10^7. More details about DLD and related data acquisition will be discussed in the next section.

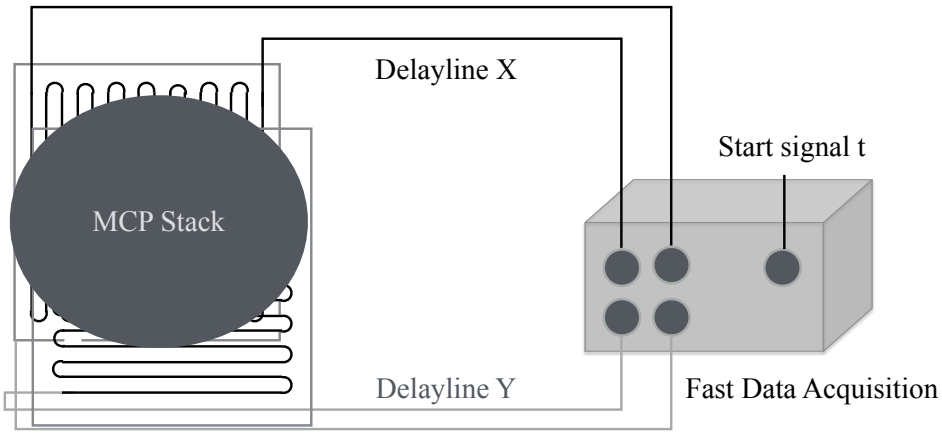

Figure 2.11: Schematic drawing of the basic assembly of a delayline detector

2.3.4 Basic Energetic Properties

Figure 2.12 is an example of the measurement of photoelectrons. The electron spectrometer and the sample are electrically connected to keep the Fermi level the same as the reference level. The binding energy of the electrons is defined by

$$E_{bin} = h\nu - E_{kin} - WF_{sample}\,. \tag{2.33}$$

The energy E'_{kin} (marked in Figure 2.12) is measured by the spectrometer and after the calibration of the work function of the spectrometer, the binding energy of the sample relative

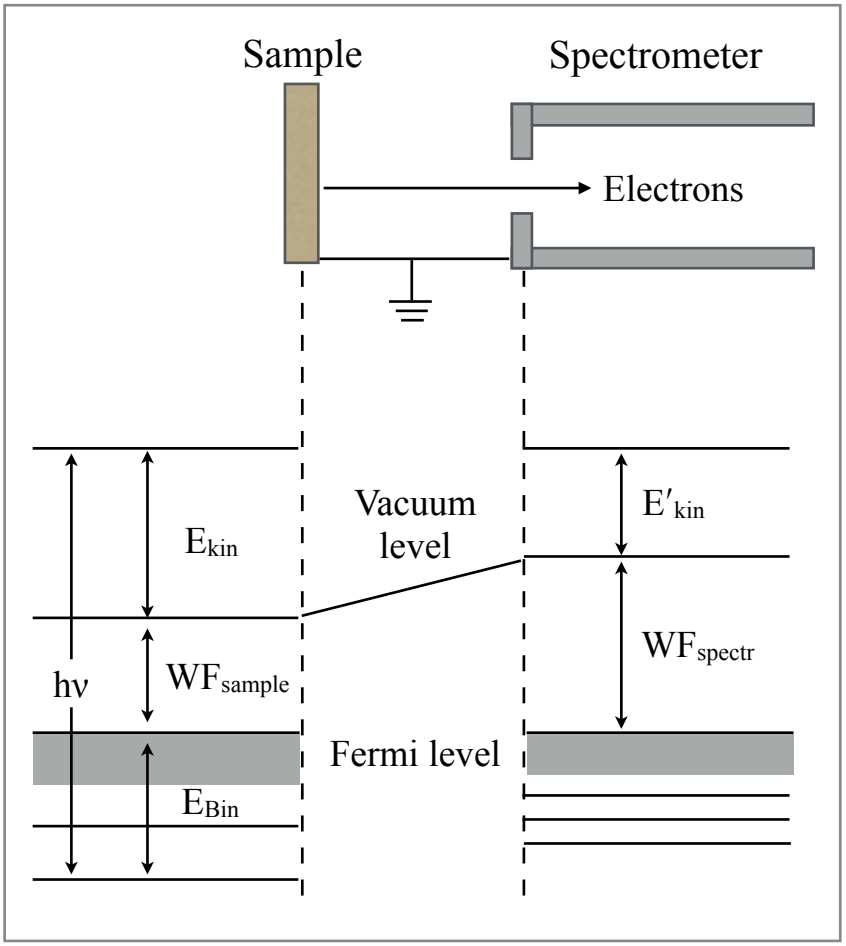

Figure 2.12: Energy scheme of the photoelectron spectroscopy

to the Fermi level can be determined without needing to know its work function, since

$$E_{kin} + WF_{sample} = E'_{kin} + WF_{spectr}\,. \tag{2.34}$$

Typical value of the analyzer work function is between 4 and 5 eV, and the precise calibration is generally required through the software to have the correct energy calibration for different materials.

2.4 DATA ACQUISITION AND PROCESSING

In this section, we discuss the details of the data collection for our two-dimensional angle-resolved images and time-resolved images. Moreover, the large data set processing is described comprehensively.

2.4.1 Principles of Detection

The trajectories of electrons possessing different energies within the HSA are passing through concentric circles. In a first-order approximation, the radial image position R of electrons

with kinetic energy E_k is given by

$$\frac{R - R_0}{R_0} = \frac{E_k - E_{pass}}{E_{pass}} \cdot \frac{D}{R_0}, \tag{2.35}$$

in which D is the HSA dispersion where the theoretical value of D is $D = 2 \cdot R_0$. The radial distance between neighboring exit slits ΔR is selected to meet the requirement of a constant kinetic energy difference between neighboring channels ΔE_k. The number of particles N reaching each collector is counted separately, and these numbers are stored and preprocessed in the data acquisition unit (shown in Figure 2.11).

The energy difference ΔE_k between neighboring channels at the distance ΔR is:

$$\Delta E_k = \frac{\Delta R}{D} \cdot E_{pass}, \ or \ E_{pass} = \frac{D}{\Delta R} \cdot \Delta E_k \,. \tag{2.36}$$

When the pass energy changes throughout the observed spectrum, a calculation of the detected energy range of the electrons is necessary. Thus a software routine calculates the electron number N in each channel at the nominal kinetic energy.

2.4.2 MPPE Spectrum Acquisition System

Figure 2.13 shows the control panel of the DLD, where the main parts are highlighted in red squares. As mentioned in the previous section, we need to set the values of E_{Kin} and E_{pass} to set the center energy and the energy diserpison, and the spectrum energy range is centered by the E_{Kin} value (eV) with the range of $\pm E_{pass}/10$ eV. To intiate the spectrum collecting process, the high voltage applied to the detector is critical for sensitive detection. The default value of the detector voltage is 1950 V, but after a test we established that a voltage of 1850 V is sufficient to obtain a good signal-to-noise 2D images. It is important to make the action of applying the high voltage very slowly (100 V/s) every time after baking the system while monitoring the pressure change of the chamber, since there might be some unexpected gas and particles absorbed in the analyzer which could cause extra charged particles hitting the MCP plate, which could cause damage.

For the precise measurement of the angle-resolved 2D image, the fine calibration of the spectrometer work function needs to be adjusted occasionally to ensure the accurate measurements under different settings of E_{Kin} and E_{pass}.

In the section 2.2, we introduced the principle of operation of our HSA. With certain selected E_{Kin} and E_{pass} values, entrance and exit slits as shown in Figure 2.10, we can

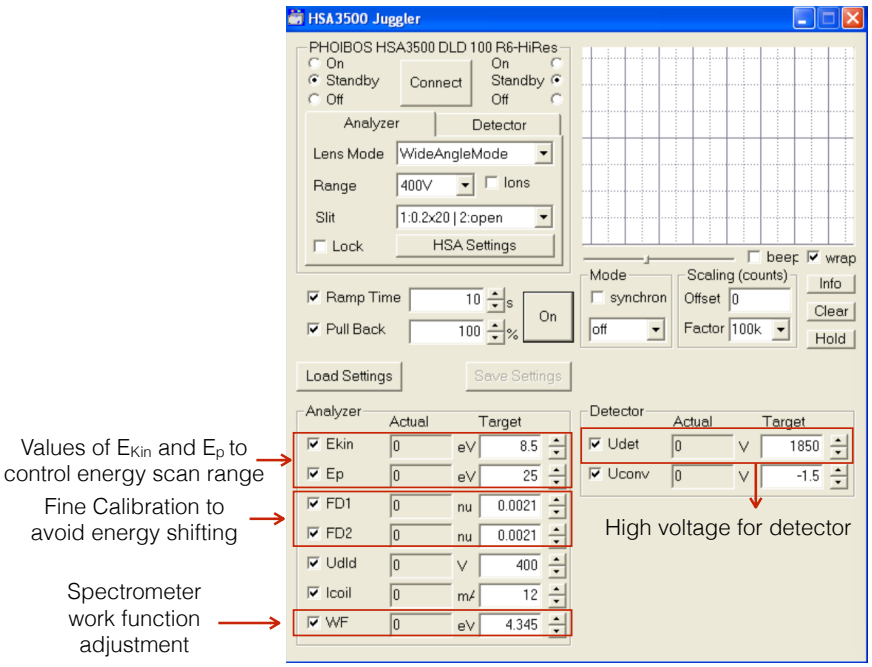

Figure 2.13: Control panel of the detector

obtain a 2D image of every single scan. The Figure 2.14 gives an illustration of one single scan. From this example we notice that the software could give the electron counts of the whole spectrum or selected range of the image and the maximum counts of the detector is 100×10^6/s, but in general we would not allow such large count rate since it could lead to a strong space charge effects and detector saturation, which would distort the 2D spectrum. Such large count rate would also rapidly degrade the multichannel plate detector. Rather than acquiring a large number of counts at once, a more practical mode of operation is to accumulate several hundreds of images (1 image per second) in order to get a better signal-to-noise ratio in the acquired spectrum. For example, for Cu(111) surface, to avoid

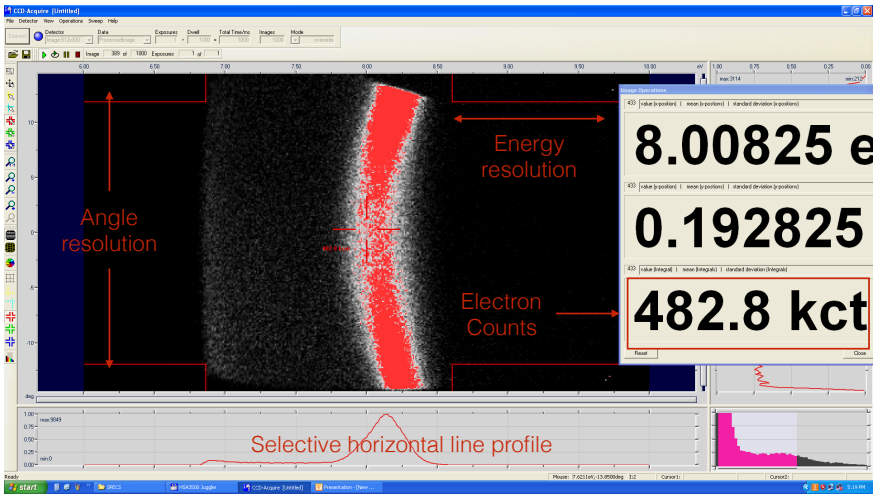

Figure 2.14: An example of the angle-resolved 2D spectrum measurement on Cu(111) surface

any distortion caused by large count rate, we kept the count rate around 40×10^6/s and accumulate 300 images to obtain a nice spectrum.

2.4.3 Pump-probe Measurements

The experimental setup for time-resolved measurements on ultrafast electron dynamics is shown in Figure 2.15. All the control panels and the data collection systems are programmed with LabVIEW, provided by SPECS. For pump-probe experiments we acquire 2D energy vs. momentum images as a function of the delay between pump and probe pulses. The pulse pairs with a variable delay are generated by the MZI. The scanning is performed by sending a scanning waveform from a Stanford Research Systems SRS345 arbitrary functional

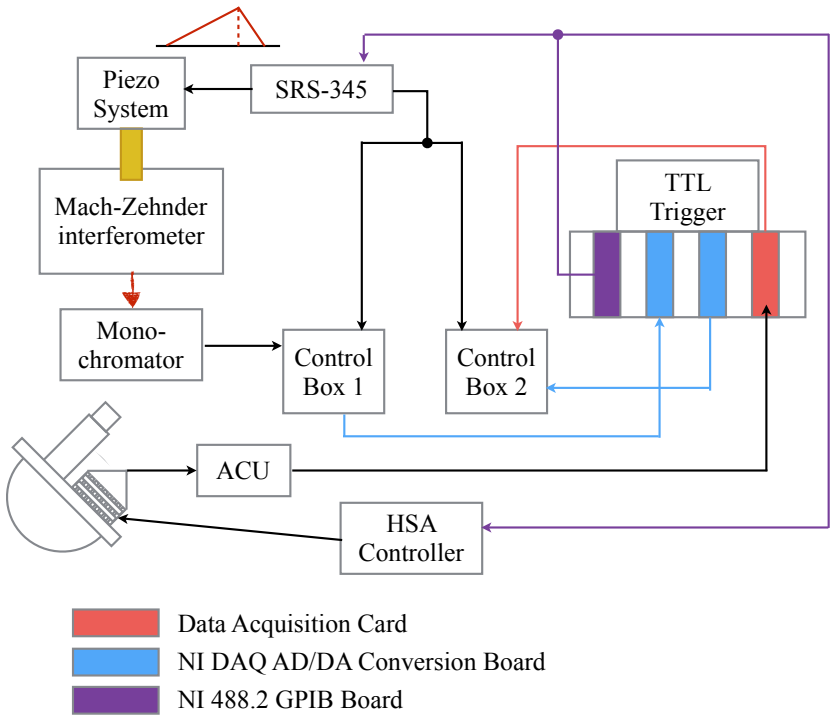

Figure 2.15: The electronic system for the interferometric two-pulse correlation data acquisition.

generator to the electrical controller of the piezoelectric actuator in the MZI. The driving waveform has an approximately sawtooth shape for slow forward and fast return scanning. The driving signal is amplified to drive a piezo actuator, which translates a pair of retro-reflecting mirrors on the flexure stage in MZI. The stage translation is as large as $\pm 100 \mu m$, which gives a variable delay of ± 350 fs. The delay time range can be adjusted by the function generator amplitude and the offset voltage can be used to set the start delay. As described in Figure 2.4, the MZI has two output beams. One is introduced to the UHV chamber as the excitation source for photoemission, and the other is focused into the monochromator, which is tuned to transmit the light at the intensity maximum (approximately the carrier wave) of the broadband input laser beam. The selected laser signal is detected by a fast-response photodiode, which records the interference fringes between the pump and probe pulses. The interference fringes are used to align the laser path through the MZI for the best alignment, as well as to calibrate the delay scanning. The alignment involves adjustment to obtain the maximum fringe visibility. During the experimental scanning, the sinusoidal interference signal gives precise time axis calibration and the reference for synchronized addition of multiple interferometric scans.

Multiple scans are performed repeatedly with the sawtooth driving waveform. The frequency of the wave is variable for different requirements of an experiment. Synchronously,

with the scanning, the photodiode voltage is read every 150 μs by the A/D board corresponding to record the reference interference signal with a typical delay interval of $0.05 - 0.2$ fs for every data point, and the interval range gives the option of how frequenlyt we want to collect the data. In Figure 2.15, the scheme of scanning and data acquisition is shown. First, the PC sends a command to one A/D-D/A board, requesting the control box 1 to acquire analog interference fringes from the photodiode. Then the wave is stored into different time bins. Since the displacement of the piezoelectric actuator is non-linear with the input voltage, the recorded fringes need to be linearized to convert the recorded calibration wave form into sine wave and determine the phase of the coherent photoemission signals. Second, and simultaneously with the calibration signal, another A/D- D/A board sends a TTL signal to control box 2 in order to trigger the ACU to start obtaining the 2D spectra. The spectrum scanning program is provided by SPECS written in LabView. There are two triggers in the collecting process. The first trigger tells the program to start and stop a single scan. These scans are accumulated for the same time interval as for the second trigger fringe signal within one period to form one image. After the acquisition is completed, all the 3D data files are summed using the time calibration to generate the common time axis. The spectrum scanning program is provided by SPECS written in LabView.

Because the detection system provides 2D angle-resolved spectra, with time-resolved

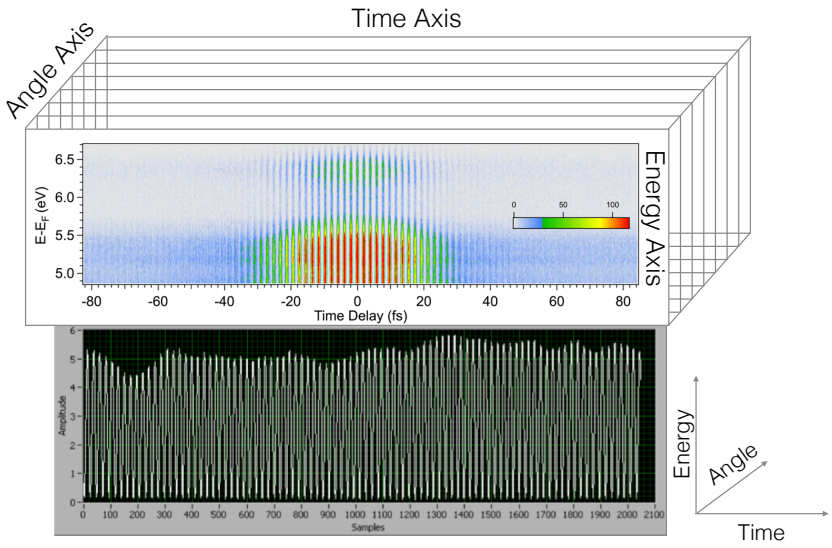

Figure 2.16: An illustration of 3D time-resolved data with signal synchronization. The interferometer is the cut at 0 degree.

measurement, one more dimension, time delay is added, which leads to a three-dimensional (3D) structure. Figure 2.16 gives a simple idea of the 3D data set, which contains selected energy window (eV), $\pm 15^o$ angle-resolved range and time delay scanning (fs). When analyzing the data, we select specific angles, because momentum is independent of energy and time, as shown in the figure 2.16.

3.0 BACKGROUND OF MULTI-PHOTON PHOTOEMISSION (MPP)

This chapter will cover the fundamental physical processes measured by time-resolved multi-photon photoemission (TR-MPP) spectroscopy including the multiphoton absorption processes at solid surfaces and their simulation by Optical Bloch Equation approach. The time-resolved interferometric spectroscopy is a very important technique, which has been developed recently for measuring the coherent charge carrier dynamics. As we discussed in Chapter 2, interferometric TR-MPP spectroscopy will be our primary method for the investigation of photoexcitation dynamics of both occupied and unoccupied states in different systems.

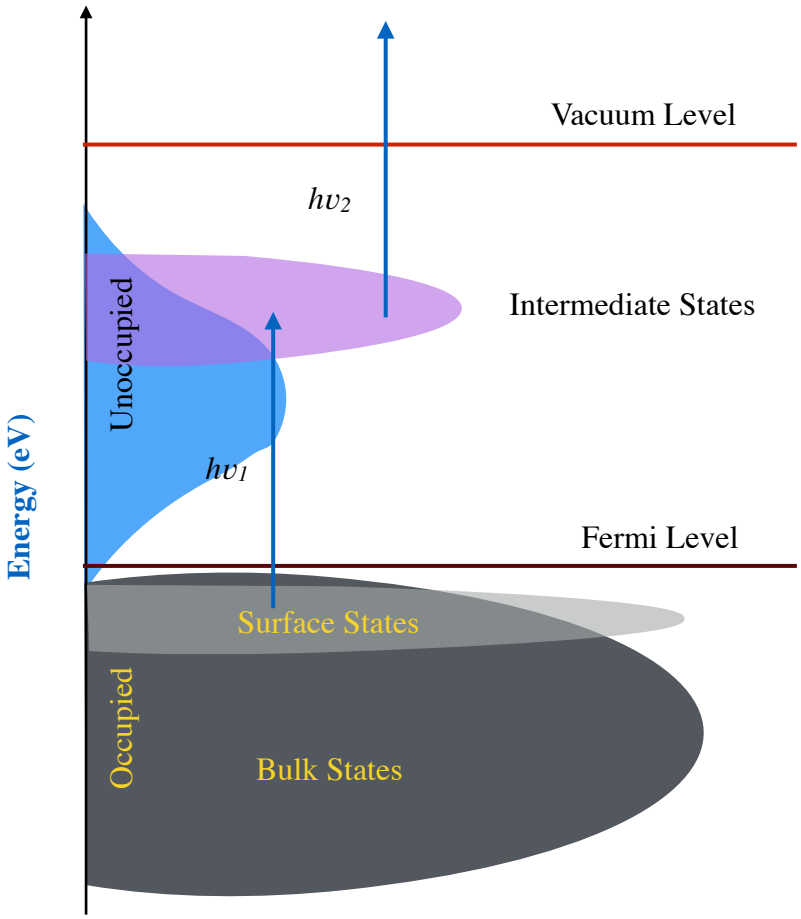

Figure 3.1: Excitation scheme in two-photon photo process.

3.1 DYNAMICS OF HOT ELECTRONS

3.1.1 Laser Pulse Induced Electron Distribution

The photoexcitation process of a metal surface can excite electrons from the occupied states below to the unoccupied states above the Fermi level to form an excited state electron distributions. The excitations can terminate at higher energy levels below or above the vacuum level. Figure 3.1 gives a typical electronic structure of a single crystal metal surface with both occupied and unoccupied states, and a simple two-photon photoexcitation (2PP) process is showing the population change where photons are exciting the electrons. For the unoccupied state with the energy E between the Fermi level and the vacuum level, the pump laser $\hbar\omega_1$ gives the electron sources by populating E from a lower energy level $E - \hbar\omega_1$ and $\hbar\omega_2$ depopulates E by further exciting the electrons from energy E to higher energy level $E + \hbar\omega_2$. In Figure 3.1 the higher state is the final state above the vacuum level and the electrons become free to get collected by the detector. In this case, the total photon excited electron contribution at the unoccupied state E can be estimated as:

$$H(k,t) = A \cdot I_p(t) \times [D(E-\hbar\omega_1)f(E-\hbar\omega_1)(1-f(E)) \\ -D(E)]f(E)(1-f(E+\hbar\omega_2))] \tag{3.1}$$

where $I_p(t)$ is the photon flux, $D(E)$ is the density of states (DOS), and $f(E)$ is the function of the Fermi-Dirac distribution.[65] As shown in Figure 3.1, detecting different electron energies, which are excited above the vacuum level gives the 2PP spectrum. The spectrum contains information on the joint DOS of the occupied and unoccupied states (marked as colored and grey features, respectively, in Figure 3.1), that are coupled by a two or more photon absorption process.

Moreover, as we briefly mentioned in Chapter 2, by splitting the femtosecond pulses into pump and probe beams with a time delay, we can measure the electron population dynamics in any targeted unoccupied states, which are observable in an MPP spectrum. The state population of the intermediate is time-dependent,[65] with a time dependence that can be described by a rate equation for energy and momentum dependent electron population

$$\frac{\mathrm{d}(n(k,t))}{\mathrm{d}t} = H(k,t) + \frac{\mathrm{d}(n(k,t))}{\mathrm{d}t}|_{e-e} + \frac{\mathrm{d}(n(k,t))}{\mathrm{d}t}|_{e-ph} + \{indirect\ process\}\,. \tag{3.2}$$

In Eq. 3.2, the first term describes the hot-electron distribution induced directly by the laser excitation; the second term gives the electron population decay process through electron-electron (e-e) scattering, where electrons excited onto the unoccupied state scatter with the electrons in occupied states;[66] and the third term describes the electron-phonon (e-ph) scattering, which is slower in general and transfers less energy than e-e scattering,[67] so in most cases it is not as important as the second term; the last term, indicated as *indirect process*, such as the Auger electron process, or the ultrafast interfacial charge transfer, can also affect the population dynamics under some circumstances.[19, 68, 69]

3.1.2 Fermi-Liquid Theory for Electron-Electron Scattering

The population decay of the electrons in excited states of metals due to the e-e scattering usually occurs on the femtosecond time scales, through the screened Coulomb interactions.[66] Figure 3.2 gives the scheme for describing the phase space for e-e scattering required by energy and momentum conservation according to the Fermi liquid theory.[66] An electron excited to an energy E above the Fermi level with the momentum $\vec{k}$ scatters with another electron below the Fermi level at an energy E_1 with the momentum $\vec{k_1}$. This scattering process generates to two secondary electrons above the Fermi level with momentua $\vec{k_2}$ and $\vec{k_3}$, which satisfy the energy and momentum conservation. The total e-e scattering rate for

electron at E is given by

$$\frac{\mathrm{d}f(k)}{\mathrm{d}t}|_{e-e} = (1 - f(k))S_e^+(k) + f(k)S^- + e(k) \tag{3.3}$$

where $f(k)$ and $1 - f(k)$ are the electron and hole occupation factors; $S_e^+(\vec{k})$ and $S_e^-(\vec{k})$ represent the electron scattering rates of getting into and out of the $\vec{k}$ state accordingly. These two rates can be written as

$$S_e^+(\vec{k}) = \frac{2\pi}{\hbar} \sum_{k_1,k_2,k_3} |M(k,k_1,k_2,k_3)|^2 (1 - f(k_1))f(k_2)f(k_3)\delta_k\delta_E, \tag{3.4}$$

and

$$S_e^-(\vec{k}) = \frac{2\pi}{\hbar} \sum_{k_1,k_2,k_3} |M(k,k_1,k_2,k_3)|^2 (-f(k_1))(1 - f(k_2))(1 - f(k_3))\delta_k\delta_E \tag{3.5}$$

where the delta functions δ_k and δ_E impose the momentum and energy conservation in an e-e scattering process, and $M(k,k_1,k_2,k_3)$ is the Coulomb scattering matrix element.

In order to estimate the e-e scattering rate, we need to calculate the screened matrix of $|M(k,k_1,k_2,k_3)|$, which is given by the screened Coulomb potential,

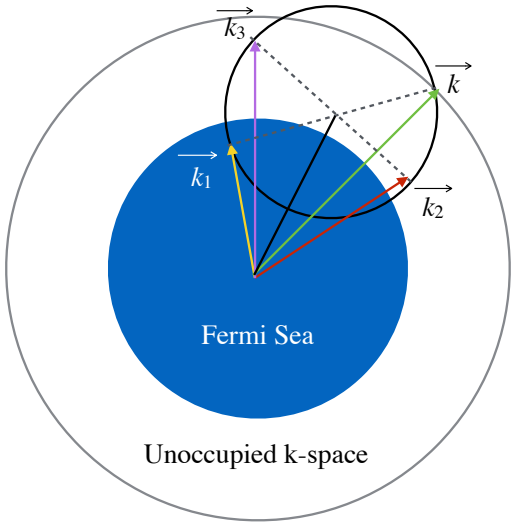

Figure 3.2: The e-e scattering process from the Fermi-Liquid theory. The inner circle represents the Fermi sea and the outer one represents the momentum $\vec{k}$ space.

$$|M|^2 = \frac{e^4}{q^4 \varepsilon_0^4 |\varepsilon(\vec{q}, E_{ex})|^2}, \tag{3.6}$$

where ε_0 is the vacuum dielectric constant, $\vec{q} = \vec{k} - \vec{k_2}$ and $E_{ex} = E(\vec{k}) - E(\vec{k_2})$ are the exchange terms of momentum and energy during the e-e scattering. The cross section gives the probability of the hot electron which initially has $E(\vec{k})$ in the momentum space scattering with another electron with $E(\vec{k_1})$ within the Fermi sea, leading to excitation two new electrons after the scattering above the Fermi level with energies of $E(\vec{(k_2)})$ and $E(\vec{(k_3)})$, respectively.[70]

According to the Thomas-Fermi approximation, the dielectric constant that determins the strength of the screened Coulomb interactionn in Eq. 3.6 can be approximated by

$$\varepsilon(\vec{q}, E_{ex} = 0) = \varepsilon_b(1 + \frac{q_s^2}{q^2}), \tag{3.7}$$

where $\varepsilon(\vec{q} = 0, E_{ex} = 0) = \varepsilon_b$ is given by the long wavelength static approximation for the tabulated dielectric constant of the metal. In Eq.(3.7), $q_s = \beta \cdot q_{TF}$ is the Thomas-Fermi screening wave vector $q_{TF} = \frac{e^2}{\varepsilon_0 \varepsilon_b} \sum_k \frac{\partial f(k)}{\partial E_k}$ and β is an adjustable parameter used to fit the experimental result.

The free-electron scattering matrix element assuming the Thomas-Fermi screening is then

$$|M|^2 = \frac{e^4}{q^4 \varepsilon_0^2 |\varepsilon[\vec{q}, E_{ex}]|^2} = \frac{e^4}{q^4 \varepsilon_0^2 \varepsilon_b^{0^2} (1 + \frac{\beta^2 e^2}{\varepsilon_0 \varepsilon_b^0 q^2} \sum_k \frac{\partial f(k)}{\partial E_k})^2} \,. \tag{3.8}$$

The overall e-e scattering rate at $T = 0K$ can be obtained by applying derivation in Eq. 3.4, Eq. 3.5 and Eq. 3.8 and integrating over the available k-space near Fermi surface region to obtain:[62]

$$\frac{1}{\tau_{ee}} = \frac{e^4 k_F^2}{16\pi^3 \hbar^4 \varepsilon_0^2 \nu_F^3 q_s^3} \times [\frac{2k_F q_s}{4k_F^2 + q_s^2} + \tan^{-1}(\frac{2k_F}{q_s})](E - E_F)^2 \,. \tag{3.9}$$

This Eq.3.9 is generally used to make a prediction of the energy dependence of the electron decay rates, through screened Coulomb interactions in different metals. The lifetimes of the hot-electrons are described by an inverse-square law dependence of the electron energy with respect to the Fermi level. As the electron energy approaches the Fermi energy, the electron scattering time tends to infinity because the phase space vanishes, and as an electron tends to higher energies, the scattering time decreases with the inverse squared dependence on energy:

$$\tau_{ee} \propto \frac{1}{(E - E_F)^2} \,. \tag{3.10}$$

The free electron Fermi-liquid theory (FLT) only gives an upper limit for e-e scattering rates in real metals, because hot electrons near the Fermi level are significantly screened by the virtual valance band excitations and the ionic nuclear cores. Thus, the screening length calculation in Eq.3.7 can be revised as following when the band structure (especially the metal d-band) and the density of state (DOS) at the Fermi level are considered:

$$q_s = q_{TF} = \left(\frac{e^2}{\varepsilon_0} D(E_F) \right)^{\frac{1}{2}} \,. \tag{3.11}$$

Ogawa et al. applied both the free electron FLT and the band structure correction to

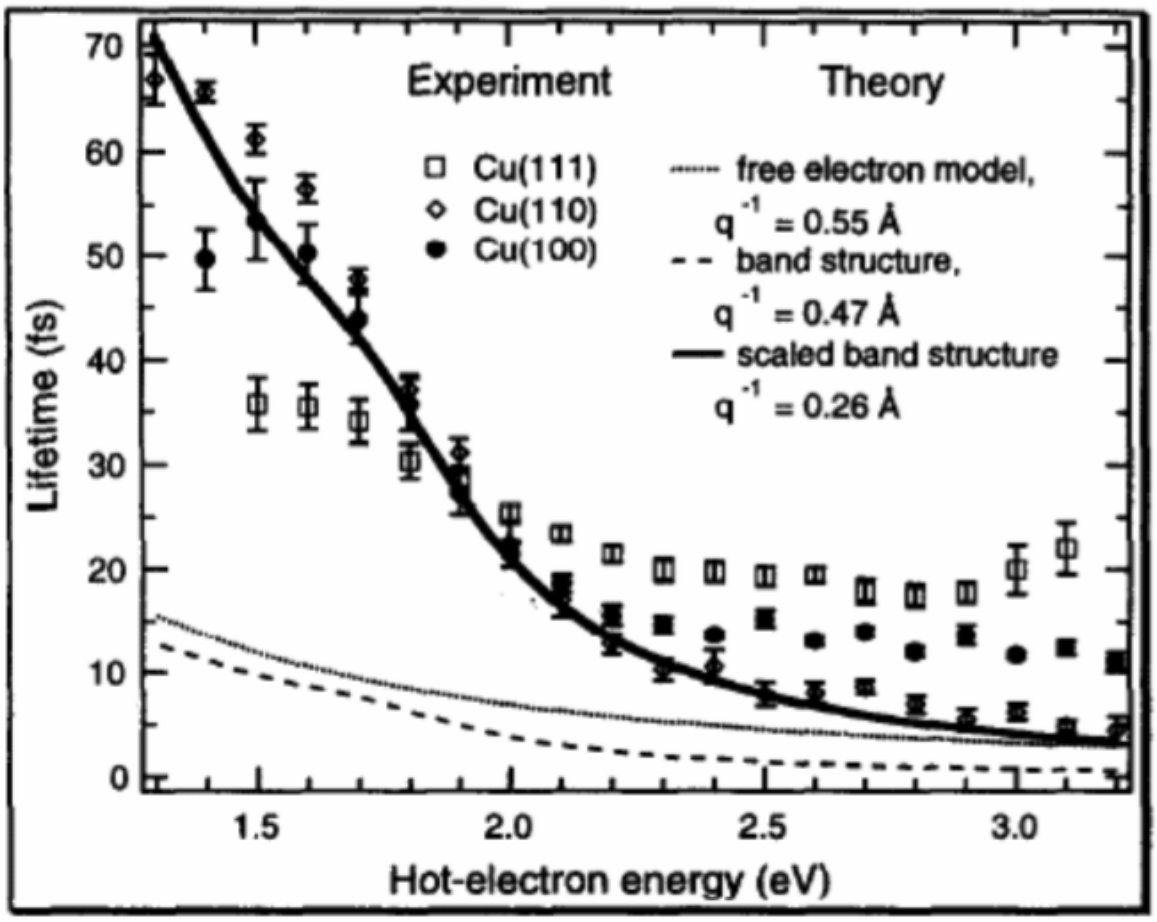

Figure 3.3: The experimental measurements of hot-electron lifetimes for the low index surfaces of single crystal Cu with theoretical calculations, through free electron FLT model and the band structure calculation.[18]

calculate the hot electron lifetimes and compare them with the experimental data. In the free-electron model, they used is 0.55 for the screening length q_{TF}^{-1} and 0.27 instead in the band structure calculation through Eq. (3.11). The band structure calculation method gives better results for the hot-electron lifetimes of the low index surfaces of Cu shown in Figure 3.3. For applying FLT calculation to a realistic prediction of the hot-electron lifetimes, free electron approximation and the electronic band structure corrections are implemented. As a result FLT could reproduce the experimental results in low energy range (0.3∼2.2 eV).[22, 71]

3.1.3 Other Electron Scattering Pathways

In last section, e-e scattering rate was described as one of the factors which determines the electron decay time range for the intermediate states in an mPP process. In some cases, there are other processes which may have influence on the intermediate states lifetime, which need to be considered.

Figure 3.4 gives several different electron excitation pathways at Cu(111) surface. One direct interband excitation process is available from the occupied *d*-bands located between 2 to 5 eV below the Fermi level to the unoccupied upper *sp*-band, which is marked as process A in Figure 3.4. With one photon energy of $\hbar\nu = 3.6eV$, this process creates the electrons up to a threshold value E_{thres} of 1.6 eV. Moreover, the electrons also can be excited by an indirect

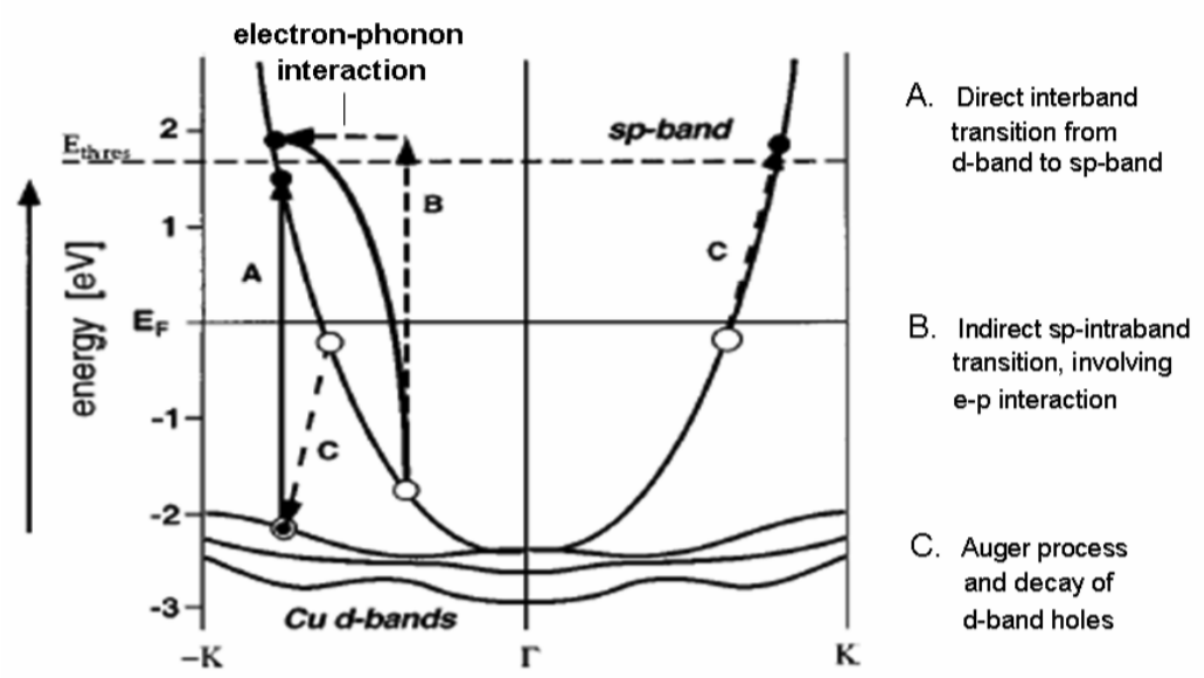

Figure 3.4: Other electron excitation mechanism in Cu surfaces[19]

sp-intraband transition, denoted as process B in Figure 3.4. In case B, the electron has to be scattered within a defect in the crystal lattice or through a phonon to satisfy momentum conservation. Due to the differences in the DOS and the priority of the excitation, process A is much more likely to happen than process B, and larger optical cross section, process A will generate a large amount of *d*-band holes. Once the *d*-band holes are generaged, the process C denoting the Auger decay mechanism, can significantly contribute to the generation of the secondary hot electrons.

Due to the different nature of the generation processes, the generation rate of hot electrons excited via interband (process A) or intraband (process B) transitions are defined by the time duration of the laser pulse. In the case of the decay of d-band holes by the Auger recombination, the hot electrons generated by process C can be generated with a time decay. Thus, when the Auger decay generates hot electrons the delayed rise of hot electrons has to be considered for the accuracy of the hot electron lifetime determination.[19, 72]

3.2 DESCRIPTION OF THE OPTICAL BLOCH EQUATIONS SIMULATION OF INTERFEROMETRIC TWO-PULSE CORRELATION DATA

In this section, I will describe how I use Optical Bloch Equations (OBE)[62, 73, 74] to simulate interferometric two-pulse correlation data for an mPP process. I will use the three-level system as an example of how to write out the density matrix elements.

Figure 3.5b gives the schematic excitation for three-photon absorption system, with three common excitation scenarios and Figure 3.5a shows how the dynamics parameters that are assigned for the population decay time and the decoherence times. A three-photon photoemission (3PP) process, which is most relevant to my experiments, can be described by a four energy level scheme: **0** is the initial energy level below the Fermi level, and could be an occupied bulk or surface state, which provides the needed electrons in the following excitation; the energy level **1** and **2** are between the Fermi level and the vacuum, and can be a real unoccupied or just a virtual state; and **3** is the final energy corresponding to a free electron state above the vacuum level. With our tunable NOPA system, the photon energy can be specifically tuned to satisfy the resonance condition from the initial to an unoccupied state (the first scheme in Figure 3.5b) or between two different unoccupied states (the second

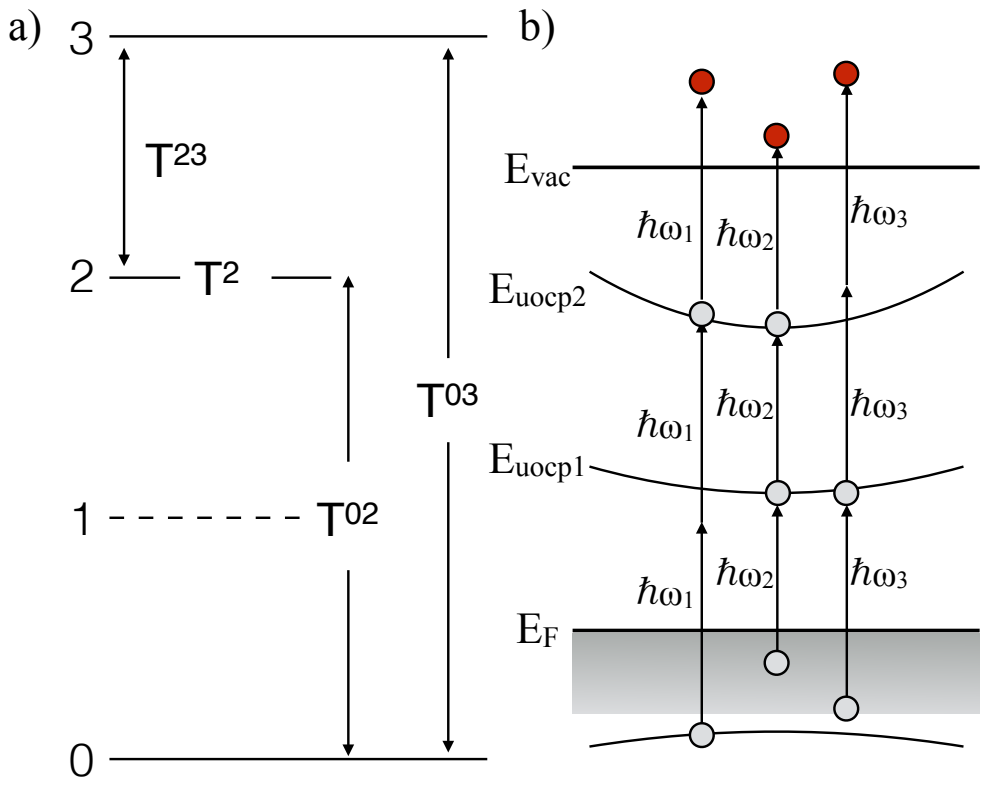

Figure 3.5: **a)**The schematic assignment of the dynamics parameters in the OBE. **b)**Three possible excitation processes in 4 energy level system (more details in the text).

scheme in Figure 3.5b) to enhance the coherent excitation process. Another situation is if we want to explore an unknown unoccupied state itself, we can easily tune the photon energy to be off resonant excitation (the third scheme in Figure 3.5b) to focus on this state only. Some examples of these different excitation processes will be discussed in the next chapter.

Now consider an electronic system with the discrete energy states by using a set of normalized orthogonal basis ϕ_k, where the non-perturbated Hamiltonian is:

$$H_0\phi_k = E_k\phi_k = \hbar\omega_k\phi_k \,. \tag{3.12}$$

The laser pulse excitation introduces a time-dependent perturbation term to the Hamiltonian which couples the eigenstates of the system. Now the total Hamiltonian is written as $H(t) = H_0 + H'(t)$, and by using the same original basis set, the time dependent wave function introduced by the perturbation term is:

$$\Psi(t) = \sum_k a_k(t)\phi_k = \sum_k e^{-i\cdot k\cdot\omega_l t} c_k(t)\phi_k. \tag{3.13}$$

This wave function is described in a rotating coordinate system with an angular frequency ω_l, which is the carrier frequency of the laser beam.[75]

By solving the time dependent Schrödinger equation of

$$i\hbar\frac{\partial\psi(t)}{\partial t} = H(t)\psi(t), \tag{3.14}$$

we obtain that

$$\sum \phi_k[c_k(t)(-ik\omega_l)e^{-ik\omega_l t} + \dot{c_k}(t)e^{-ik\omega_l t}] = \frac{-i}{\hbar}\sum c_k(t)(H_0 + H'(t))\phi_k e^{-ik\omega_l t}\,. \tag{3.15}$$

Multiplying the complex conjugate ϕ_k^* on both side of the Eq.3.15 and integrating in the wave space, then we can get obtain and equation of motion for the coefficients c:

$$\dot{c_n} = -i(\omega_n - n\omega_l)c_n - \frac{i}{\hbar}\sum_k H'_{nk}e^{i(n-k)\omega_l t}c_k, \tag{3.16}$$

where the matrix element $H'_{nk} = \int \phi_n^* H'(t)\phi_k \mathrm{d}^3 r$ and the perturbation term could be estimated in the electric dipole approximation:

$$H'(t) = -e\cdot r\cdot E(t) = -e\cdot r\cdot A(t)cos(\omega_l t)\,. \tag{3.17}$$

Considering a four-level system, as shown in Figure 3.5a, it couples by a three-photon

transition and the coefficients in Eq.3.16 are:

$$
\begin{aligned}
\frac{\partial c_0(t)}{\partial t} &= -i\omega_0 c_0 - \frac{i}{\hbar}[E_1(t)cos(\omega_l t) + E_1(t-\delta)cos(\omega_l(t-\delta))] \cdot e^{-i\omega_l t} c_1 \\
\frac{\partial c_1(t)}{\partial t} &= -i(\omega_1 - \omega_l)c_1 - \frac{i}{\hbar}[E_2(t)cos(\omega_l t) + E_2(t-\delta)cos(\omega_l(t-\delta))] \cdot e^{-i\omega_l t} c_2 \\
&\quad - \frac{i}{\hbar}[E_1(t)cos(\omega_l t) + E_1(t-\delta)cos(\omega_l(t-\delta))] \cdot e^{-i\omega_l t} c_0 \\
\frac{\partial c_2(t)}{\partial t} &= -i(\omega_2 - \omega_l)c_2 - \frac{i}{\hbar}[E_3(t)cos(\omega_l t) + E_3(t-\delta)cos(\omega_l(t-\delta))] \cdot e^{-i\omega_l t} c_3 \\
&\quad - \frac{i}{\hbar}[E_2(t)cos(\omega_l t) + E_2(t-\delta)cos(\omega_l(t-\delta))] \cdot e^{-i\omega_l t} c_1 \\
\frac{\partial c_3(t)}{\partial t} &= -i(\omega_3 - \omega_l)c_3 - \frac{i}{\hbar}[E_3(t)cos(\omega_l t) + E_3(t-\delta)cos(\omega_l(t-\delta))] \cdot e^{-i\omega_l t} c_2, \qquad (3.18)
\end{aligned}
$$

in which δ is the time-delay between the pump and probe pulses. In the above set of differential equations, the amplitudes E_n indicate the transition coefficients between energy level n-1 to n, and we will use the amplitudes again to describe the Hamiltonians later. If the excitation processes involves a virtual state like the first one in Figure 3.5b, the transition coefficient related to this virtual state is much smaller than for a real state, and in most situation, it is considered as a very small value.

In order to describe the process of multiphoton photoemission, we prefer to formulate the problem in terms of the density operator elements $\rho_{mn} = c_m c_n^*$, in which the diagonal elements ρ_{nn} gives the population at the energy level of n, and the off-diagonal elements

ρ_{mn} correspond to oscillatings coherences between the energy states of m and n. Taking the first-order derivative of ρ_{mn} relative to t, we can obtain

$$\frac{\partial \rho_{mn}}{\partial t} = \frac{\partial (c_m(t) c_n^*(t))}{\partial t} = \frac{\partial c_m(t)}{\partial t} c_n^*(t) + c_m(t) \frac{\partial c_n^*(t)}{\partial t}, \tag{3.19}$$

where:

$$\begin{aligned} \dot{c_m c_n^*} = i(\omega_n - n\omega_l)\rho_{mn} + \frac{i}{\hbar} H'_{n+1,n} e^{i\omega_l t} \rho_{m,n+1} \\ + \frac{i}{\hbar} H'_{n,n-1} e^{-i\omega_l t} \rho_{m,n-1} \end{aligned} \tag{3.20}$$

$$\begin{aligned} \dot{c_m c_n^*} = -i(\omega_m - m\omega_l)\rho_{mn} - \frac{i}{\hbar} H'_{m,m-1} e^{i\omega_l t} \rho_{m-1,n} \\ - \frac{i}{\hbar} H'_{m,m+1} e^{-i\omega_l t} \rho_{m+1,n} \,. \end{aligned} \tag{3.21}$$

The initial populations of the unoccupied states are zero and electrons excited into these states will decay back to zero. In additional to the population decay, the optical excitation also produces coherence oscillations at single ($\hbar\omega$) , two- ($2\hbar\omega$) or three-photon ($3\hbar\omega$) frequencies caused by the dipole coupling. As indicated in Figure 3.5a, we assign T_n as the population decay time for state n and T_{mn} as the decoherence time between states m and n.[76] For the four level system, the density matrix is a 4×4 Hermitian matrix, where the off-diagonal elements are complex conjugates.

Thus, there are only 10 independent elements instead of 16. The diagonal elements can be described as:

$$\frac{\partial \rho_{11}}{\partial t} = -\frac{\rho_{11}}{T_1} - \frac{i}{\hbar} H'_{10}\big(e^{i\omega_l t}\rho^*_{10} - e^{-i\omega_l t}\rho_{10}\big) - \frac{i}{\hbar} H'_{21}\big(e^{-i\omega_l t}\rho_{21} - e^{i\omega_l t}\rho^*_{21}\big) \tag{3.22}$$

$$\frac{\partial \rho_{22}}{\partial t} = -\frac{\rho_{22}}{T_2} - \frac{i}{\hbar} H'_{21}\big(e^{i\omega_l t}\rho^*_{21} - e^{-i\omega_l t}\rho_{21}\big) - \frac{i}{\hbar} H'_{32}\big(e^{-i\omega_l t}\rho_{32} - e^{i\omega_l t}\rho^*_{32}\big) \tag{3.23}$$

$$\frac{\partial \rho_{33}}{\partial t} = -\frac{\rho_{33}}{T_3} - \frac{i}{\hbar} H'_{32}\big(e^{i\omega_l t}\rho^*_{32} - e^{-i\omega_l t}\rho_{32}\big) \tag{3.24}$$

$$\frac{\partial \rho_{00}}{\partial t} = -\frac{\partial \rho_{11}}{\partial t} - \frac{\partial \rho_{22}}{\partial t} - \frac{\partial \rho_{33}}{\partial t}, \tag{3.25}$$

and the off-diagonal elements are:

$$\frac{\partial \rho_{10}}{\partial t} = -[i(\Delta_1 - 0\omega) + \frac{1}{T_{01}} + \frac{1}{2T_1}]\rho_{10} - \frac{i}{\hbar} H'_{10} e^{i\omega_l t}(\rho_{00} - \rho_{11}) - \frac{i}{\hbar} H'_{21} e^{-i\omega_l t}\rho_{20} \tag{3.26}$$

$$\frac{\partial \rho_{21}}{\partial t} = -[i(\Delta_2 - \Delta_1) + \frac{1}{T_{12}} + \frac{1}{2T_1} + \frac{1}{2T_2}]\rho_{21} - \frac{i}{\hbar} H'_{21} e^{i\omega_l t}(\rho_{11} - \rho_{22}) - \frac{i}{\hbar} H'_{32} e^{-i\omega_l t}\rho_{32} + \frac{i}{\hbar} H'_{10} e^{-i\omega_l t}\rho_{20} \tag{3.27}$$

$$\frac{\partial \rho_{32}}{\partial t} = -[i(\Delta_3 - \Delta_2) + \frac{1}{T_{23}} + \frac{1}{2T_2} + \frac{1}{2T_3}]\rho_{32} - \frac{i}{\hbar} H'_{32} e^{i\omega_l t}(\rho_{22} - \rho_{33}) + \frac{i}{\hbar} H'_{21} e^{-i\omega_l t}\rho_{31}, \tag{3.28}$$

$$\frac{\partial \rho_{20}}{\partial t} = -[i(\Delta_2 - 0\omega) + \frac{1}{T_{02}} + \frac{1}{2T_2}]\rho_{20}$$
$$- \frac{i}{\hbar} H'_{21} e^{i\omega_l t} \rho_{22} - \frac{i}{\hbar} H'_{32} e^{-i\omega_l t} \rho_{30} + \frac{i}{\hbar} H'_{10} e^{i\omega_l t} \rho_{31} \tag{3.29}$$

$$\frac{\partial \rho_{31}}{\partial t} = -[i(\Delta_3 - \Delta_1) + \frac{1}{T_{13}} + \frac{1}{2T_1} + \frac{1}{2T_3}]\rho_{20}$$
$$- \frac{i}{\hbar} H'_{32} e^{i\omega_l t} \rho_{21} + \frac{i}{\hbar} H'_{21} e^{i\omega_l t} \rho_{32} + \frac{i}{\hbar} H'_{10} e^{-i\omega_l t} \rho_{30} \tag{3.30}$$

$$\frac{\partial \rho_{30}}{\partial t} = -[i(\Delta_3 - 0\omega) + \frac{1}{T_{03}} + \frac{1}{2T_3}]\rho_{30}$$
$$- \frac{i}{\hbar} H'_{32} e^{i\omega_l t} \rho_{20} + \frac{i}{\hbar} H'_{10} e^{i\omega_l t} \rho_{31}, \tag{3.31}$$

where

$$H'_{10}(t-\delta) = E_1(t) cos(\omega_l t) + E_1(t-\delta) cos(\omega_l (t-\delta))$$
$$= A_1 \big[e^{-(t/T_0)^2} cos(\omega_l t) + e^{-((t-\delta)/T_0)^2} cos(\omega_l (t-\delta)) \big] \tag{3.32}$$

$$H'_{21}(t-\delta) = A_2 \big[e^{-(t/T_0)^2} cos(\omega_l t) + e^{-((t-\delta)/T_0)^2} cos(\omega_l (t-\delta)) \big] \tag{3.33}$$

$$H'_{32}(t-\delta) = A_3 \big[e^{-(t/T_0)^2} cos(\omega_l t) + e^{-((t-\delta)/T_0)^2} cos(\omega_l (t-\delta)) \big], \tag{3.34}$$

and $\Delta_1 = 1\omega - \omega_l$, $\Delta_1 = 2\omega - 2\omega_l$ and $\Delta_3 = \omega_3 - 3\omega_l$ are the corresponding first-, second- and third order resonance detuning frequencies.

In general, for n-level energy system, the elements can be summarized as:

$For\ m > n,$

$$\begin{aligned}\frac{\partial \rho_{mn}}{\partial t} = &-[i(\omega_m - \omega_n - m\omega_l + n\omega_l) + \frac{1}{T_{nm}} + \frac{1}{2T_m} + \frac{1}{2T_n}]\rho_{mn} \\ &- \frac{i}{\hbar} H'_{m,m-1} e^{i\omega_l t} \rho_{m-1,n} - \frac{i}{\hbar} H'_{m+1,m} e^{-i\omega_l t} \rho_{m+1,n} \\ &+ \frac{i}{\hbar} H'_{n+1,n} e^{i\omega_l t} \rho_{m,n+1} + \frac{i}{\hbar} H'_{n,n-1} e^{-i\omega_l t} \rho_{m,n-1} \end{aligned} \tag{3.35}$$

$and\ for\ m = n,$

$$\begin{aligned}\frac{\partial \rho_{nn}}{\partial t} = &-\frac{\rho_{nn}}{T_n} - \frac{i}{\hbar} H'_{n,n-1}\left(e^{i\omega_l t}\rho^*_{n,n-1} - e^{-i\omega_l t}\rho_{n,n-1}\right) \\ &- \frac{i}{\hbar} H'_{n+1,n}\left(e^{-i\omega_l t}\rho_{n+1,n} - e^{i\omega_l t}\rho^*_{n+1,n}\right). \end{aligned} \tag{3.36}$$

For the fitting procedure, we need to choose reasonable initial values for the incoherent and coherent decay time and the suitable values for the excitation transition amplitudes, according to the previous experience and related published work. The fitting details will be discussed in the next section.

3.3 SIMULATION PROCEDURE

In this section, I will explain how to simulate the experimental data by solving the OBE to obtain the critical decay parameters described in last section

3.3.1 Decomposition of I2PC

As briefly mentioned in section 2.2.1, the second-order autocorrelation of a Gaussian laser pulse can be decomposed into three components and each one contains the pulse information at different resonance frequency. Here I will describe how to extract this information on photoexcitation dynamics from our experimental interferometric two-pulse correlation (I2PC) data using a similar procedure. Although the I2PC signals of multi-photon photoemission are similar to the autocorrelation of the laser, they contain more information on the hot electron population and polarization dynamics, which causes deviations from the autocorrelation scans. The laser pulses interacting with the sample surface induces linear or nonlinear polarizations, which could oscillate coherently at the different orders of photon frequency, and meanwhile the photon-excited electrons decay incoherently through e-e inelastic scattering. The coherent oscillations with linear or nonlinear polarization bring the interference at 1ω, 2ω and 3ω frequencies, and the incoherent population decay is phase independent

process, as shown in Figure 3.5a

By assuming Gaussian shaped pulses with pulse width of τ_p,

$$\overrightarrow{E(t)} \propto \exp(-4\ln 2(\frac{t}{\tau_p}))^2 \cos(\omega t), \tag{3.37}$$

The third order autocorrelation can be described as:

$$G_3(\delta) = \int_{-\infty}^{\infty} [(E(t) + E(t+\delta))^3]^2 \mathrm{d}t, \tag{3.38}$$

With the same concept as in Section 2.2, the third order autocorrelation can also be decomposed into four parts corresponding to different orders of frequency,

$$G_3(\delta) \approx Constant(I_{0\omega} + I_{1\omega} + I_{2\omega} + I_{3\omega}), \tag{3.39}$$

where:

$$I_{3\omega}(\delta) = \frac{8c}{\lambda} \sqrt{\left[\int_{\delta-\lambda/8c}^{\delta+\lambda/8c} I(\delta) cos(3\omega\lambda) \mathrm{d}\delta\right]^2 + \left[\int_{\delta-\lambda/8c}^{\delta+\lambda/8c} I(\delta) sin(3\omega\lambda) \mathrm{d}\delta\right]^2} \tag{3.40}$$

$$I_{2\omega}(\delta) = \frac{4c}{\lambda} \sqrt{\left[\int_{\delta-\lambda/4c}^{\delta+\lambda/4c} I(\delta) cos(2\omega\lambda) \mathrm{d}\delta\right]^2 + \left[\int_{\delta-\lambda/4c}^{\delta+\lambda/4c} I(\delta) sin(2\omega\lambda) \mathrm{d}\delta\right]^2} \tag{3.41}$$

$$I_{1\omega}(\delta) = \frac{2c}{\lambda} \sqrt{\left[\int_{\delta-\lambda/2c}^{\delta+\lambda/2c} I(\delta) cos(1\omega\lambda) \mathrm{d}\delta\right]^2 + \left[\int_{\delta-\lambda/2c}^{\delta+\lambda/2c} I(\delta) sin(1\omega\lambda) \mathrm{d}\delta\right]^2} \tag{3.42}$$

$$I_{0\omega}(\delta) = \frac{c}{\lambda} \int_{\delta-\lambda/2c}^{\delta+\lambda/2c} I(\delta) \mathrm{d}\delta \,. \tag{3.43}$$

Here I is used instead of S because it is for general case indicating all the experimental interferometric signals we obtain.

In order to extract these envelopes from the experimental interferometric signals, there are several ways to fit or simulate by programing. In my procedure, I use one method called *windowed Fourier transformation*. In general, we can apply the Fourier transformation (FT) to I2PC signals to transform the whole time axis to the photon energy axis (frequency domain), and in this way in principle there are components of $0*\hbar\omega_l$, $1*\hbar\omega_l$, $2*\hbar\omega_l$ and $3*\hbar\omega_l$, in which $\hbar\omega_l$ is the photon frequency. With the similar methods, by selecting a time "window" and applying the FT to this window, the envelopes can be extracted for this central time spot in this window, as shown in figure. For every single time interval spot, we use the same way to select the same size of a window and obtain the envelopes information, leading to several sets of discrete points at different frequencies for the whole time axis. Sometimes the "window" can be a rectangular or gaussian pulse, however since the time window is very small, the results would be similar.

With the discrete envelope data sets, by fitting them with Gaussian function of $f(x) = a * exp(\frac{-(x-b)^2}{c^2})$, in which a, b and c are the parameters from the fitting, and c describes the variance of the data set. For a Gaussian shape, the parameter c gives the measure of full width at the half maximum (FWHM) with the relation of $FWHM = 2c\sqrt{ln2}$, and

this parameter is the only one we need to take care of. One critical way to check if the simulation gives the best description of the experimental result is to compare the fitted c from simulation result to the experimental one.

3.3.2 Fitting and selecting procedure

Figure 3.6 gives the flow chart for how the fitting and selecting program works. The blue parts are the initial procedure of decomposing the experimental data to obtain the data sets and parameters of the envelopes at different frequencies. The green parts are very time-consuming, since the program needs to solve a set of $\frac{(n+2)(n+1)}{2}$ ordinary differential equations (ODE), with energy level of n. Every time the program gets one simulation result and it needs to be decomposed and compared to the experimental parameters to examine whether the simulation gives a reasonable result. There are two things to check. One is comparing the simulated discrete envelope data set to the experimental one, by the method of Least Square fit (LSF) or two-sample test. If this test supports that the simulation is good, then the next one is to compare the fitted Gaussian parameters to confirm the first test is right. If, however, the first test does not show that the simulation is good, then the step of adjusting the time parameter compare the difference of the simulated c_{sim} and the experimental c_{exp}. This way of choosing adjust step can make sure the program takes as few

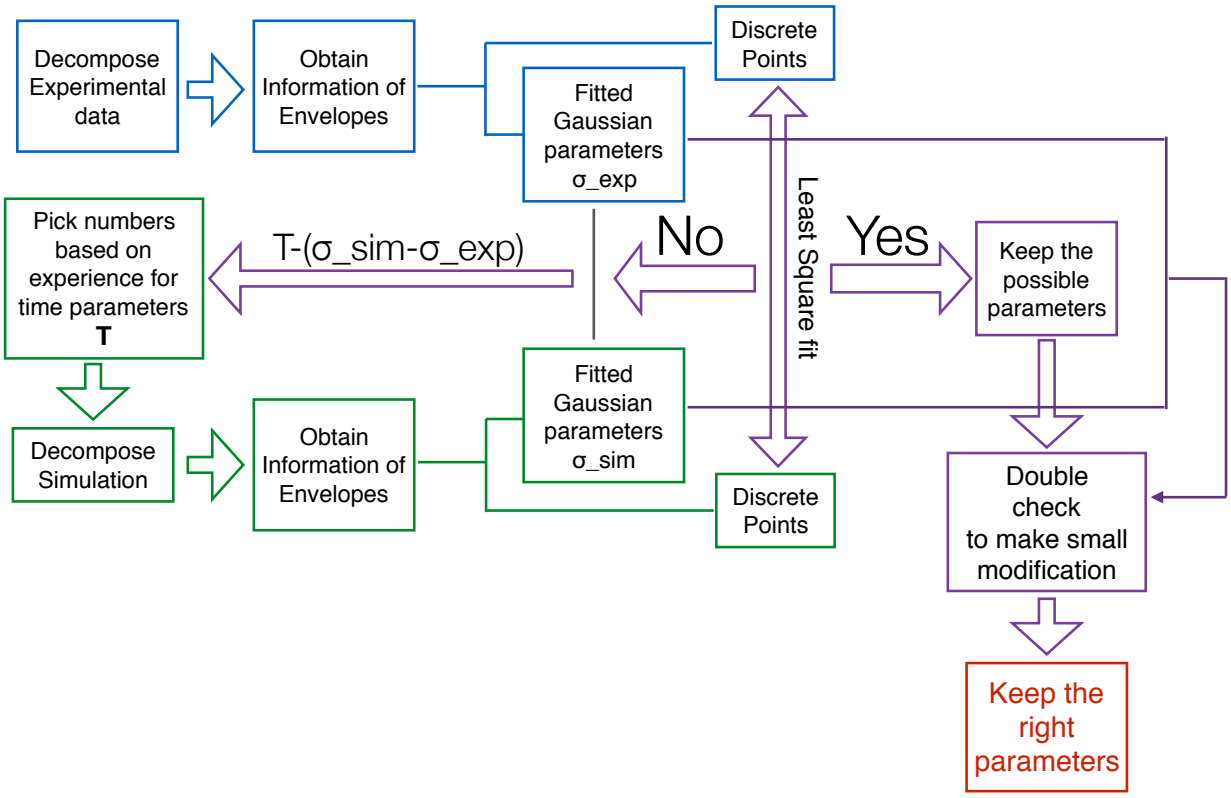

Figure 3.6: The flow chart shows the fitting and selecting procedure to obtain the critical time parameters like the indicated ones in Figure 3.5.

iterations as possible to reach the final results. The whole program written in MATLAB is shown in Appendix A.

4.0 ELECTRONIC STRUCTURE AND DYNAMICS OF CHEMISORBED ALKALI ATOMS ON RU(0001)

This chapter gives a full view of the chemisorbed alkali atoms on clean transition metal surface, including the mPP spectrum and photoexcitation dynamics. This system demonstrates all of the experimental procedures and key concepts of surface mPP spectroscopy, The main topic is spectroscopy of rubidium (Rb) and cesium (Cs) atoms on Ru(0001) surface. The study is an extension of previous studies of alkali atoms on noble metal surfaces.[12, 14]

4.1 EXPERIMENTAL METHODS

In this section the experimental methods will be introduced in detail, with the example of alkali/Ru(0001) system. In the next two chapters the methods are similar and I will only describe the particular details.

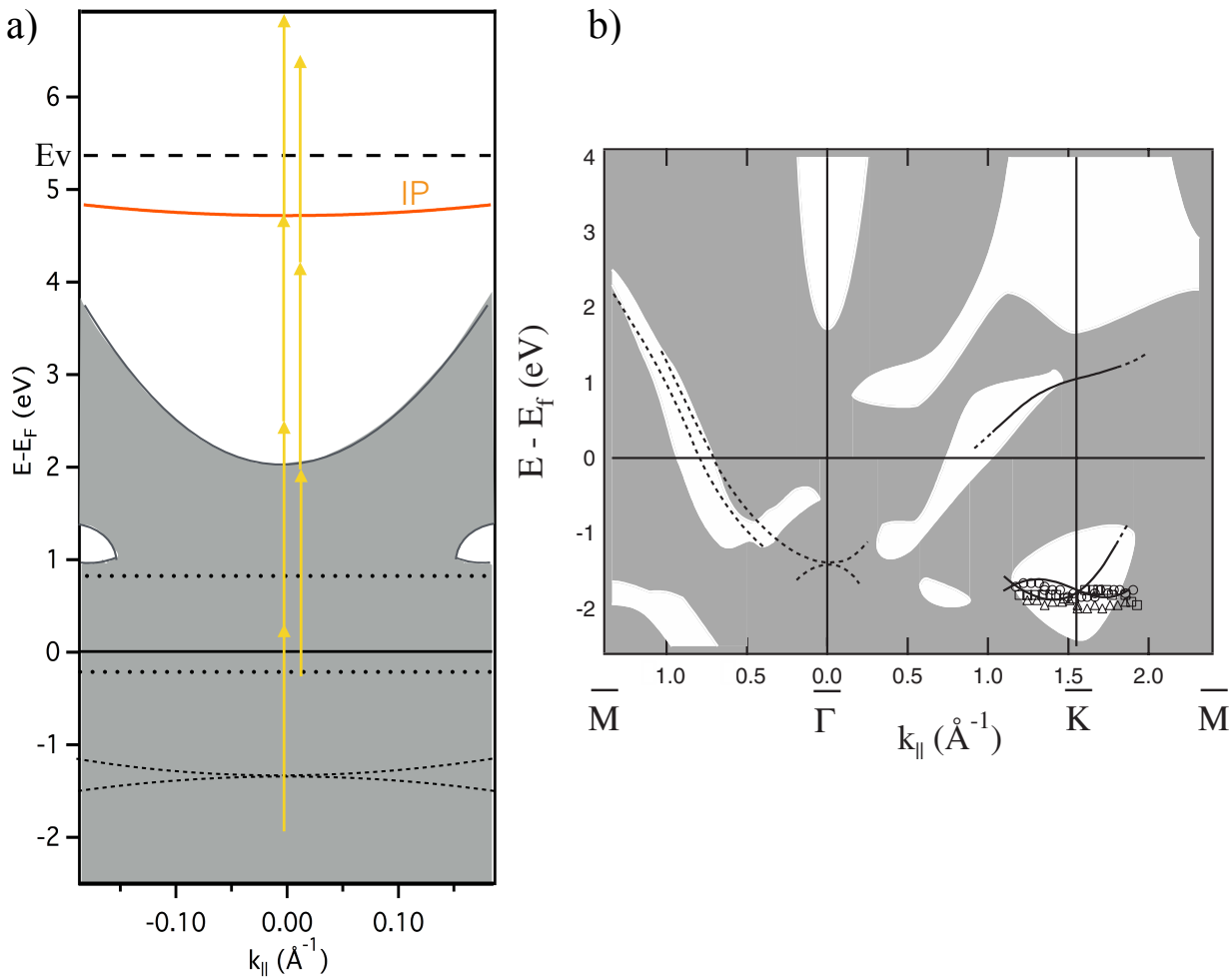

Figure 4.1: **a)** The surface-projected band structure as a function of $k_{||}$ showing the 3PP and 4PP excitation processes on clean Ru(0001) surface, with $\hbar\omega$=2.17 eV light. The dashed or dotted horizontal lines indicate the d bands of Ru(0001) from **b)**. **b)** The calculated or experimental band structure of Ru(0001) surface.[5, 6, 7]

Multidimensional coherent multi-photon photoelectron spectroscopy experiments [77] are performed in a commercial UHV chamber with a base pressure of $<10^{-10}$ mbar. The Ru(0001) surface is prepared by repeated cycles of Ar ion sputtering and annealing at 1100 K in UHV. After preparation, the sample is cooled down to ∼90 K by liquid nitrogen and then exposed to an effusive Cs or Rb atomic beam from commercial alkali atom getter sources (SAES). The alkali atoms coverage is estimated from the observed work function decreasing during the deposition using published calibration data.[78, 79, 80] The deposition is performed at the same position to eliminate any potential effects.[78, 79, 80]

MPP spectra are excited with the NOPA system, which is pumped by a Clark MXR Impulse fiber laser oscillator-amplifier system. The NOPA operates at a 1.25 MHz repetition rate with ∼20 fs pulses and typical pulse energy of <60 nJ.[77] The fundamental output of the NOPA and its second harmonic can be tuned from 900 to 270 nm corresponding to 1.38-4.59 eV photon energy.[81] The pulse is compensated for positive dispersion in the optical path using multiple bounces from a pair of matched negative dispersion mirrors. The pulse duration is measured and optimized at the position of the sample by autocorrelation measurement using interferometric time-resolved (ITR) 3PP signal from a polycrystalline Ta sample, which has a nearly instantaneous response.[82]

Angle-resolved (AR) mPP spectra are recorded with the Specs Phoibos 100 electron

energy analyzer as described in Chapter 2, which is used in the $\pm 15^{\circ}$ angular acceptance mode. The images of photoelectron energy $vs.$ momentum $[E(k)]$ are acquired in an electron counting mode using the delay-line detector. During the alkali atom deposition, mPP spectra (a combination of 3PP and 4PP) are recorded sequentially to characterize the σ- and π-resonances and the work function decrease. The deposition is terminated when the work function is reduced to the point where the signal from 2PP starts to overwhelm that from 3PP and 4PP. After the spectroscopic characterization, the photodynamics of alkali atom excitation and relaxation are investigated by ITR-3PP. In this experimental mode, the delay between identical pump-probe pulses, which are produced in a self-made Mach-Zehnder interferometer (MZI), are scanned with a <50 as time-step resolution; at each step an $E(k)$ image is acquired.[62, 76, 77] Multiple pump-probe scans are acquired and accumulated for signal averaging to generate a three-dimensional (3D), $E(k,t)$ movie of the coherent electron dynamics at alkali/Ru(0001) surfaces.

4.2 SPECTROSCOPIC FEATURES ON ALKALI/RU(0001) SURFACE

In this section, I will describe the main spectroscopic features which are the band structure of Ru(0001) surface and the alkali-induced resonances, that have been introduced in Chapter

1.

4.2.1 Clean Ru(0001) surface

Figure 4.1(a) shows the surface projected band structure of the Ru(0001) surface for a range of momenta around $k_{||}$=0 Å^{-1} that we investigate. Based on electronic structure calculations, inverse photoemission, and 2PP spectroscopy, at the Γ point the Ru(0001) surface has a projected band gap that opens at ∼2 eV and extends to at least 6 eV above the Fermi level, E_F (Figure 4.1(b)).[5, 6, 83, 84] Near E_F, the d-bands have been reported at -0.1 and 1 eV at the Γ point.[85, 5, 86] Band structure calculations also predict a d-band at -1.3 eV; these various features may have a role in mPP processes.[5, 7] The work function of Ru(0001) is reported to be 5.4-5.5 eV.[5, 83] Because the alkali atom σ-resonances are expected to occur in the low coverage limit at ∼2 eV below the vacuum level, E_v, their coincidence with the band gap is favorable for studies of alkali atom spectroscopy and dynamics. Figure 4.1 also shows some possible excitation pathways for 3PP and 4PP *via* the n=1 image potential state (IP) on the bare Ru(0001) surface.

Before the alkali atom deposition, the mPP spectrum from the clean Ru(0001) surface is recorded as shown in Figure 4.2(a). The work function Φ of the clean Ru(0001) surface is found to be 5.37 eV. The mPP spectrum is dominated by two spectroscopic features: *i*) the

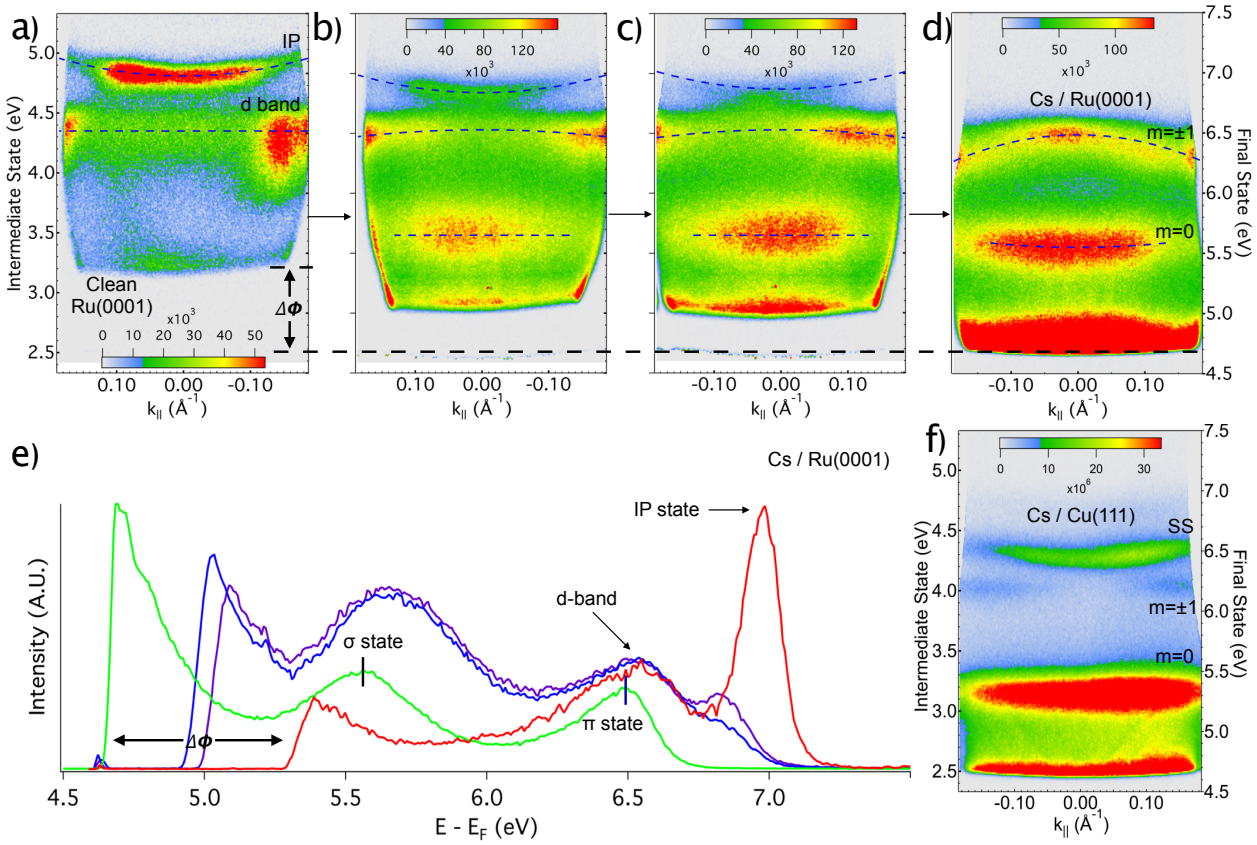

Figure 4.2: **(a)-(d)** 3PP and 4PP spectra of the Ru(0001) surface excited $\hbar\omega$=2.17 eV during the continuous deposition of Cs atoms starting from zero coverage. The spectra show the penultimate state energy (left axis) and the final photoelectron energy relative to E_F (right axis) *vs.* the parallel momentum, $k_{||}$. $\Delta\Phi$ gives the work function change before and after the deposition. The dashed straight or parabolic lines give the best fitting dispersions of specific bands. In **(a)** the fitting of the IP state gives m^*=1.1±0.02m_e and in **(d)** the masses obtained for m=0 and m=±1 are m^*=1.8±0.05m_e and -0.65±0.05m_e, respectively. **(e)** The line profiles of **(a)-(d)** that are taken at $k_{||}$=0 Å^{-1}. **(f)** The 3PP spectrum with $\hbar\omega$=2.29eV excitation of Cs/Cu(111) surface is given to contrast with the Cs/Ru(0001) surface. SS indicates the occupied Shockley surface state of Cu(111).

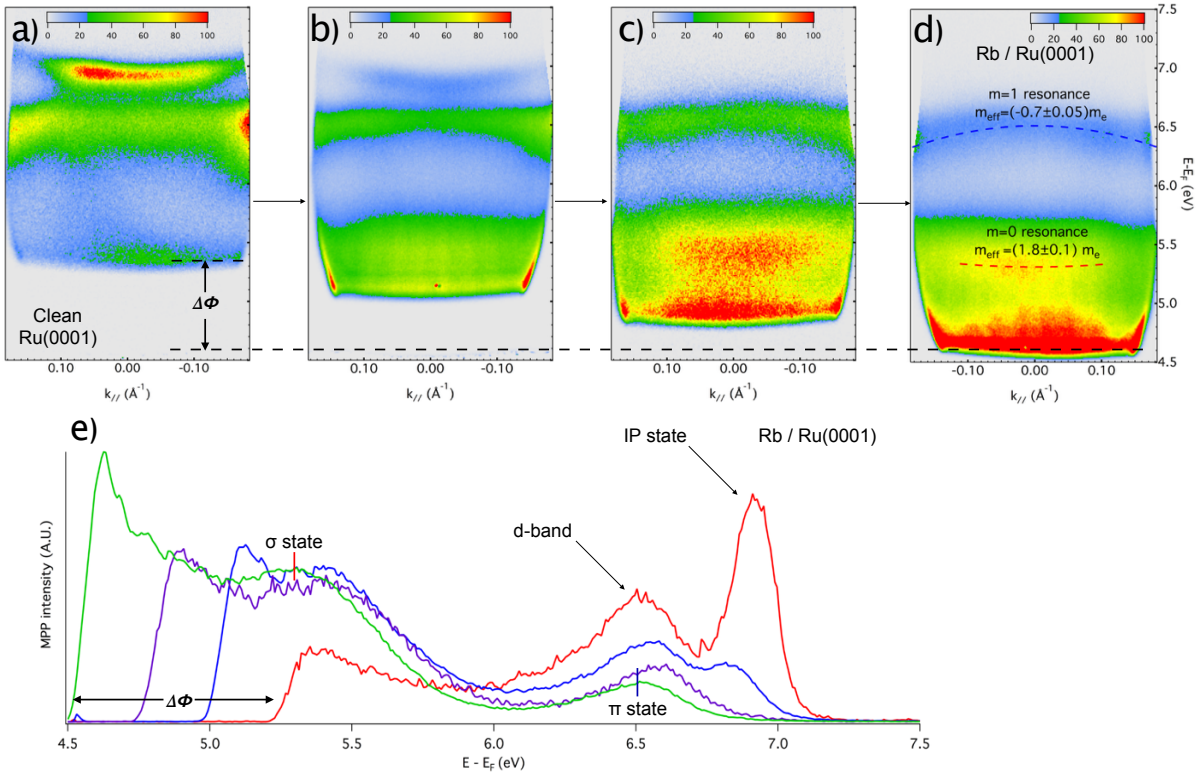

Figure 4.3: Similar to Figure 4.2 **(a)-(d)** 3PP and 4PP spectra of the Ru(0001) surface excited $\hbar\omega$=2.17 eV during the continuous deposition of Rb atoms starting from zero coverage. In **(a)** the fitting of the IP state gives m^*=1.1±0.02m_e and in **(d)** the masses obtained for m=0 and m=±1 are m^*=1.8±0.05m_e and -0.7±0.1m_e, respectively. **(e)** The line profiles of **(a)-(d)** that are taken at $k_{||}$=0 Å^{-1}.

n=1 image potential state (IP), which is the penultimate level in 4PP; and ii) a d-band, [85] which is an initial state in 3PP located at -0.1 eV below E_F. When the Ru(0001) surface is clean and well-ordered, the strongest feature in the mPP spectrum (Figure 4.2(a)) is the IP state; its intensity is stronger than the occupied d-band, even though the d-band is excited by a lower order process. The IP state binding energy with respect to the vacuum level is ∼0.58±0.04 eV, which is slightly smaller than the literature value of ∼0.64±0.03eV, [83] and its dispersion is consistent with the effective mass, m^*=1.1±0.02m_e, where m_e is the free electron mass.

4.2.2 Alkali atom resonances on Ru(0001) surface

Figure 4.2(a)-(d) shows two-dimensional $E(k)$ distribution images measured with 571 nm (2.17 eV) corresponding to three- and four-photon excitation during deposition of Cs onto Ru(0001) surface. Cross sections through the $E(k)$ distributions for the normal emission ($k_{||}$=0 Å^{-1}) are shown in Figure 4.2(e) for more quantitative visualization of the data. The $k_{||}$ measurements are taken along the Γ-K direction. The Cs adsorption causes substantial changes in the mPP spectra (Figure 4.2(b)-(d)); the work function progressively decreases as the coverage of Cs atoms increases (marked as ΔΦ in Figure 4.2(b)-(d)). The work function is reduced by formation of a surface dipole layer, which introduces an additional

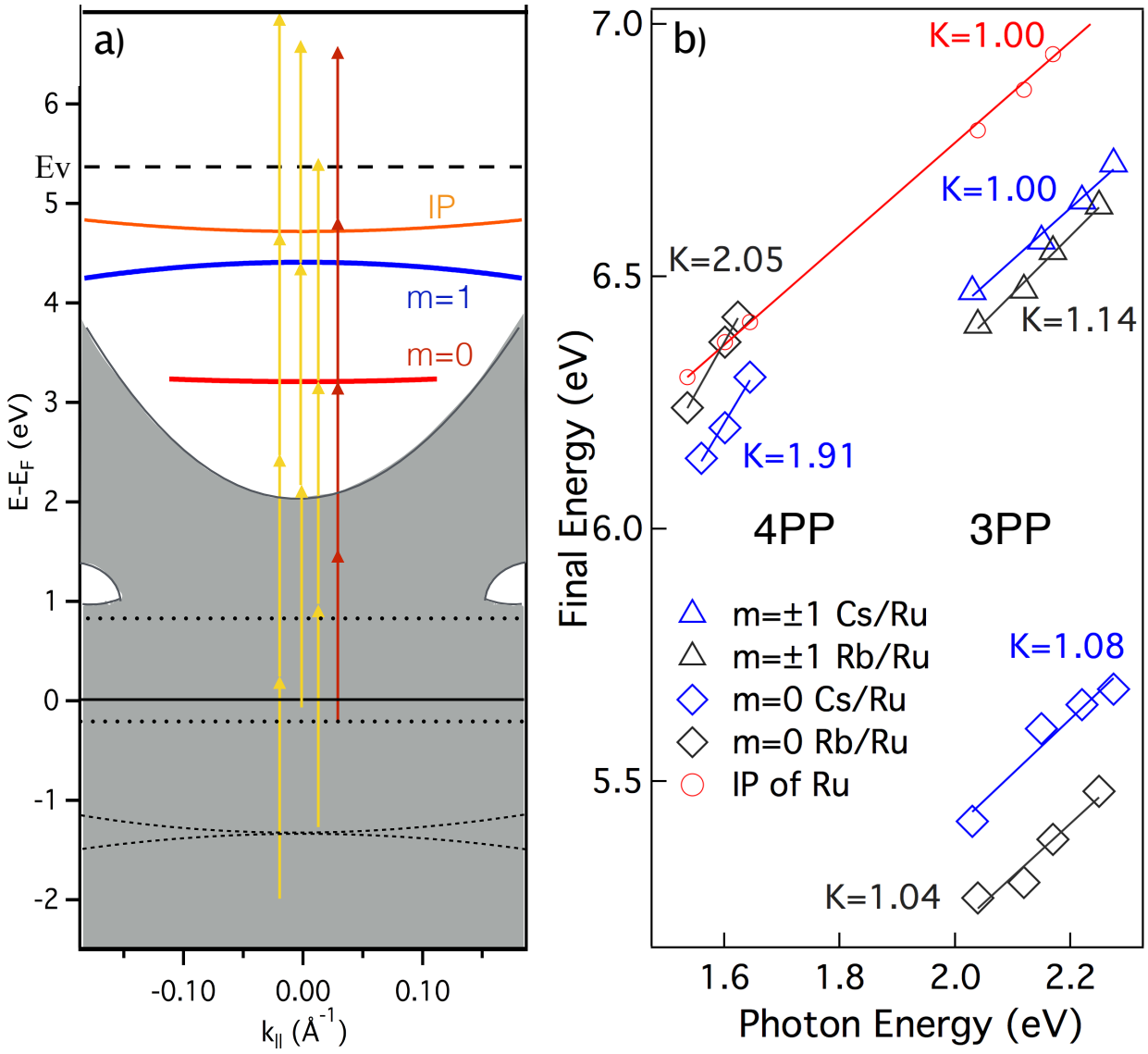

Figure 4.4: **(a)** The surface-projected band structure as a function of $k_{||}$ showing the 3PP and 4PP excitation processes through the alkali-induced resonance intermediate states. The yellow arrows show the possible transitions from the d-band of substrate Ru to m=0 and m=±1 states with $\hbar\omega$=2.17 eV light and the red arrows give the excitation processes with $\hbar\omega$=1.64 eV light. **(b)** The final states energies of various spectroscopic features are plotted as a function of photon energy and fitted to linear functions. The slopes from fitting are marked in the figure correspondingly and the intercepts are summarized in Table I for m=0 and m=±1 states. For the reference, the IP state of Ru(0001) is also plotted.

potential for transport of electrons through the surface.[27, 29, 87] Furthermore, adsorption of Cs also causes the IP state intensity to wane and the σ- and π-resonances to wax. By comparing the work function change with the literature calibration curves for Cs/Ru(0001), [78, 79, 80] we estimate the maximum coverage in our measurements to approach 0.02 ML. Because Rb^+ has approximately the same size as Cs^+, we expect it to have very similar calibration curve.[79, 80] For comparison with the alkali atom electronic structure on noble metal surfaces, we also show a single 3PP $E(k)$ image for Cs/Cu(111) with <0.01 ML coverage that is obtained under similar conditions as for Cs on Ru(0001) substrate (Figure 4.2(f)).

By contrast with the previous 2PP spectroscopic measurements of alkali atoms on noble metals, which were obtained with 3.1 eV excitation, the 3PP and 4PP scheme with visible light (1.54-2.17 eV) enables both the σ- and π-resonances to be observed within the same nonlinear order of excitation in the zero alkali atom coverage limit. Moreover, higher order mPP spectra appear to select more effectively the coherent excitations of surface states over bulk hot electron processes.[77]

Because we are detecting the alkali resonances via an mPP process, it is important to establish their position in the multi-photon absorption ladder. This is done by plotting the measured final state energy of the resonance *vs.* the photon energy and evaluating the

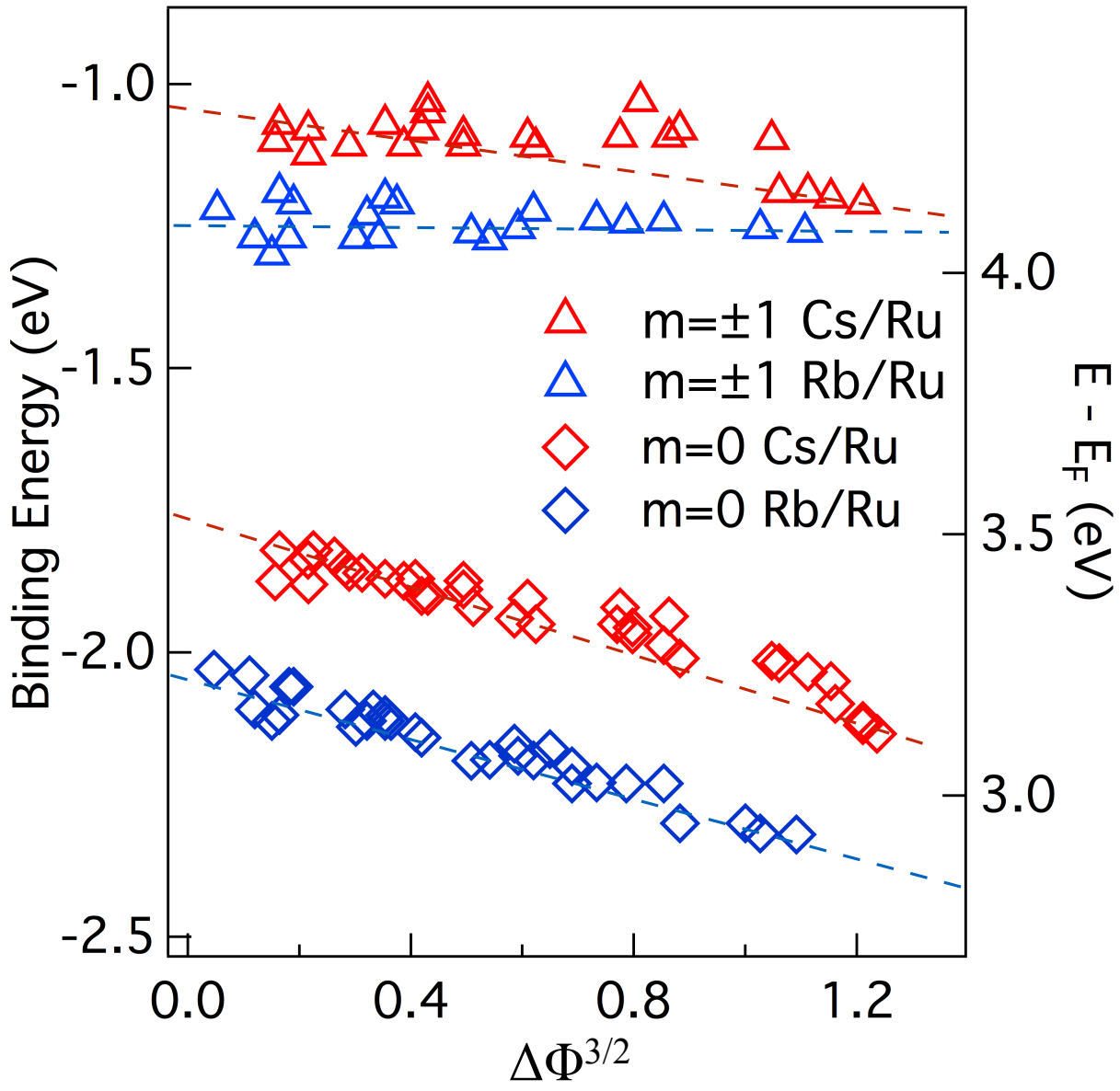

Figure 4.5: The binding energies of m=0 and m=±1 σ- and π-resonances relative to the vacuum level of the clean Ru(0001) surface (left axis) and E_F (right axis) for Rb and Cs on Ru(0001) surface, plotted versus work function change to the power of 3/2 ($\Delta\Phi^{3/2}$). Dashed lines are linear fits to the data.

resulting slope and intercept from a linear fit to the data. For reference, in Figure 4.4(b) we first consider the n=1 IP state on the clean Ru(0001) surface because being close to E_v it always takes one photon to detect in both the 3PP and 4PP schemes. In Figure 4.4(b) we also plot the final state energies of the σ- and π-resonances for the excitation with 1.54-2.27 eV photon energy pulses. In the 5-7 eV range of the final states, the resonances are detected in either by 3PP or 4PP processes depending on the excitation wavelength. In the case of 3PP ($\hbar\omega$>1.8 eV), the excitation photon energy is sufficient to excite the σ- and π-resonances by a two-photon transition, followed by single photon photoemission. Hence the plots have a slope of ∼1. In the case of excitation for 1.54<$\hbar\omega$<1.8 eV, the photoemission occurs by 4PP and their detection requires two photon adsorption; hence the slope in Figure 4.4(b) is ∼2. Based on this analysis, we can estimate that the σ- and π-resonances of Cs participate in the mPP processes as intermediate states at 3.22 and 4.35 eV for the 0.015ML alkali coverage of the measurements in Figure 4.4(b)

To remove the effect of the surface dipole potential on the σ- and π-resonance energies at a finite alkali atom coverage we must extrapolate the results to zero alkali coverage.[12, 14, 64] The change in the σ-resonance with increasing coverage is evident in Figure 4.2(b)-(d). In the case of Cu(111) and Ag(111) surfaces we have shown that the σ-resonance energy decreases linearly with respect to $\Delta\Phi^{3/2}$.[12, 14, 27, 64, 88] In Figure 4.5 we plot the σ- and π-resonance

energies for Cs and Rb on Ru(0001) surface *vs.* $\Delta\Phi^{3/2}$, and indeed find a linear trend. The dependence of the π-resonance energy on the alkali atom coverage has not been measured previously: here we find it to decrease in energy but with a much weaker dependence on the coverage than the σ-resonance. Because we expect that it should also respond to the dipole potential, this result suggests that another factor has a counteracting influence, as we will explain below.

From the linear fits to the data in Figure 4.5 (dashed lines) we can extrapolate the σ- and π-resonance energies for Cs/Ru(0001) at the zero coverage limit to be 3.59 and 4.32 eV with respect to E_F, and -1.78 and -1.05 eV with respect to E_v. The corresponding analysis for Rb/Ru(0001) gives 3.33 and 4.13 eV with respect to E_F, and -2.04 and -1.24 eV with respect to E_v. Therefore, $\sigma - \pi$ splittings for Cs and Rb are 0.73 and 0.80 eV on the Ru(0001) surface. For comparison, the zero coverage $\sigma - \pi$ splitting for the Cs on Cu(111) surface in Figure 4.2(f) is 0.87$\pm$0.02 eV. The observed $\sigma - \pi$ splittings for the Ru and Cu substrates in Figure 4.2(f) and Figure 4.5 are also comparable to the calculated zero coverage splittings for noble metal surfaces, [13, 89] although they are higher than 0.3-0.7 eV that we reported for higher alkali coverages on the Cu(111) and Ag(111) surfaces.[13, 14] This discrepancy can be attributed to the overlap between the alkali resonances and the bands of the substrate, as well as lower experimental resolution of the previous experiments; [13, 14] the mPP excitation

Table 1: The energies of σ- and π-resonances relative to E_F. m^* denotes the effective masses for the states from experiments and DFT calculations for the 6×6 Rb overlayer structure on Ru(0001). The binding energies relative to E_v are in the parenthesis.

	E 0.015ML[1]	E Zero limit[2]	$m^*_{experimental}$	$m^*_{theoretical}$
m=0 Rb	3.12 eV	3.33 (-2.04) eV	$1.8m_e$	$2.1m_e$
m=0 Cs	3.22 eV	3.59 (-1.78) eV	$1.8m_e$	$1.5\ m_e$
m=±1 Rb	4.07 eV	4.13 (-1.24) eV	$-0.7m_e$	$-0.7m_e$
m=±1 Cs	4.36 eV	4.32 (-1.05) eV	$-0.65m_e$	$-0.8m_e$

and photoelectron imaging used in the present experiments provide more accurate splittings. For reference, the free atom ns to np excitation energies, i.e. the D-lines of Cs and Rb in the absence of surface perturbation, are 1.39 and 1.56 eV. Thus, the larger splitting for Rb may be due to the larger s-p the atomic splitting. The resonance energies from the excitation wavelength and alkali coverage dependent measurements are reported in Table 1.

4.2.3 Alkali resonance band formation on Ru(0001) surface

An unexpected feature of the σ- and π-resonance spectra in Figure 4.2(b)-(d) is that they form dispersive bands with effective masses that depend on the coverage. The dashed lines in Figure 4.2(b)-(d) indicate the band dispersions that are obtained by fitting parabolic

curves to the peak maxima for different values of $k_{||}$. Similar dispersions are observed for the Rb/Ru(0001) surface. Fitting of σ- and π-bands in Figure 4.2(d) gives effective masses of m^*=1.8±0.1m_e and -0.65±0.05m_e, respectively. At lower coverages, in Figure 4.2(b) and 4.2(c), the σ-band is still non-dispersive, whereas the π-band effective mass is -1.1m_e.

The observation of highly dispersive alkali atom bands at low coverages on Ru(0001) surface is surprising because for noble metals the corresponding resonances are non-dispersive even for coverages up to 0.1 ML.[13] Clearly the alkali orbitals are able to interact at very low coverages on the Ru(0001) substrate. We observe a transition with coverage in the 2D spectra of Figure 4.2 from where the angular intensity distributions reflect the localized orbital character of the m=0 and m=±1 σ- and π-resonances, to a regime where angular band dispersion portend the delocalized orbital character. Specifically in Figure 4.2(b)-(d) there is a progression where the node and anti-node in the angular photoemission distributions for the π- and σ-resonance, respectively, disappear and are replaced by the band dispersions, which become stronger as the alkali coverage is increased. Thus, the orbital parentage of the two resonances is manifested in the spectra through a transitional regime where they change from the localized to a delocalized character. In the case of Cu(111) substrate we observe the localized character under similar experimental conditions. Thus the comparison between angular distributions for Ru(0001) and Cu(111) surfaces in Figure 4.2(d) and 4.2(f) shows

that the properties of the substrate significantly influence the σ- and π-resonance orbital interactions.

The observed effective masses are consistent with characteristics of bands formed by the in-plane σ-bonding of s and p orbitals.[90, 91] The m=0 orbitals are bonding, have the band minimum at the Γ point, and their Bloch wave function has no nodes at $k_{||}$=0 Å^{-1}. By contrast, the m=$\pm$1 orbitals are antibonding, have the maximum at the Γ point, and their Bloch wave function has the maximum number of nodes. Thus, the band dispersions of alkali induced states on Ru(0001) surface provide consistent evidence for the orbital origin of the σ- and π-resonances as the photoemission angular distributions for alkali covered noble metal surfaces, except for the former the electronic wave functions are delocalized, whereas for the latter they are localized. We will address the origin of these differences through electronic structure calculations.

In our analysis of the band dispersions we assume that the interaction between alkali atoms at low coverage is purely repulsive due to dipole-dipole interaction, for which there is overwhelming evidence based on real and reciprocal space measurements.[33, 78, 79, 80, 92, 93] Although Cs and Rb are bound by more than 3 eV at low coverage by ionic forces, the barriers for surface diffusion are in a few meV range.[80, 94] All measurements of the work function change *vs.* alkali atom coverage for Ru(0001) surface show a smooth change

that is characteristic of increasing density of a hexatic liquid, rather than coverage dependent order-disorder phase transitions that have been documented in few cases for alkali chemisorption.[33, 47] Moreover, we do not believe that there is preferential decoration of step edges at low coverage, based on STM measurements of Cs on noble metal surfaces at comparable coverages.[92, 93]

Based on the above analysis we note that there are two factors affecting the σ- and π-resonance energies at finite alkali atom coverages. First, the increasing strength of the dipole potential as the alkali atom coverage increases should lower the σ- and π-resonance energies by approximately the same amount. Second, the band formation at the Γ point stabilizes the bonding σ-resonance and destabilizes the anti-bonding π-resonance. The orbital interactions increase with the coverage because the magnitude of the effective mass decreases and the band curvature at the Γ point increases. Therefore, the two factors should enhance the stabilization of σ-resonance and counteract the stabilization of the π-resonance at the Γ point. We believe that the strong negative dispersion of the π-resonance explains in part the different coverage dependent tunings of the σ- and π-resonance energies in Figure 4.5.

Another aspect of 3PP spectra in Figure 4.2(b)-(d) is the large width of the σ-resonance for both the Cs and Rb/Ru(0001) surfaces. The origin of the width could be the coupling of the surface resonance to the resonant bulk bands for finite values of $k_{||}$, as can be expected

from Figure 4.1. For example, such broadening was found for Cs/Cu(100), where the σ-resonance is similarly close to the bulk band edge.[53, 56, 83] An additional factor that may influence the σ-resonance width are possible resonances in optical transitions involving the d-bands of the substrate. Specifically, an unoccupied d-band with significant width has been reported at 0.9 -1.0 eV above E_F in both the inverse photoemission and 2PP spectra of clean and graphene modified Ru(0001) surface.[85, 86] It is possible that the σ-resonance is excited by a one-photon transition from this intermediate d-band, as suggested in Figure 4.4, and therefore, the observed spectral width has contributions from the joint density of the coupled states in the 3PP process, rather than reflecting a very fast decay of the σ-resonance.

4.3 THEORETICAL ANALYSIS OF THE ALKALI-RU BONDING AND BAND FORMATION

In this section, I will present the theoretical explanation for the unexpected band formation of alkali on Ru(0001) system. The electronic structure and interactions of alkali/Ru surfaces is calculated based on the density function theory (DFT).

The band formation of the σ- and π-resonances at coverages where thorough space electronic interactions are expected to be too weak for electron delocalization suggests that the

substrate could mediate them. This points to a different character of alkali atom bonding to a transition metal surface Ru(0001) than was found for noble metals.[89, 95, 96, 97]

To further understand the differences in alkali atom interactions with Ru(0001) and Cu(111) surfaces, we performed first principles electronic structure calculations for both Rb and Cs on Ru(0001) surface. The results of both alkali atoms are essentially the same and we will describe only the results for Rb on Ru(0001) to explain the details in the following text. DFT calculations are not expected to predict accurately the resonance energies of alkali atoms on metal surface because the image potential is not included.[12, 98] Because the image potential is homogeneous within the 2D surface, however, we expect the errors in predicting band dispersions to be insignificant. Therefore, DFT calculations provide useful information on the comparative tendency of the σ- and π-resonances to form bands on the Ru(0001) and Cu(111) surfaces. The calculated effective masses for both Rb and Cs on Ru(0001) surface are presented in Table 1 and the band structure of Rb/Ru is depicted in Figure 4.6.

DFT calculations are carried out using plane-wave basis sets with a cut off energies of 250 eV for both Rb and Cs on Ru(0001) surface and 340 eV for Rb/Cu(111) using the generalized gradient approximation with PBE functional [99] as implemented in Vienna Ab initio simulation package (VASP).[100, 101, 102] The projector augmented wave method is

used to describe the electron-ion interaction.[103] A 6-layer slab model is used with a vacuum of 26 Å to avoid the interlayer interaction. Because the unit cell is as large as 16.2×16.2 $Å^2$, the Brillouin zone is sampled only at the Γ point.

We use a 6×6 super cell to simulate the surface, which contains 36 Ru atoms per layer: this corresponds to 0.03 ML Rb coverage. Rb atoms are in the hcp position, as dictated by previous low energy electron diffraction studies.[33] Relative to the clean Ru(0001) surface, the calculated work function decrease is 1.0 eV, which is comparable to experiments. In Figure 4.6(c) we show the surface projected band structure of Rb/Ru(0001). By comparing the projected density of states to the Rb covered Ru(0001) surface with the clean one, we identified the bands with contributions from the s- and $p_{x,y}$-orbitals of Rb around the Γ point; these bands are marked with red and blue dots in Figure 4.6(c). The σ- and π-resonance are located at 2.5 and 3.3 eV above E_F. As we discussed above, we expect these energies to be only in qualitative agreement with experiment. The dispersion, however, is meaningful and in agreement with the experiment. As expected, the σ-resonance band has a positive dispersion and the π-resonance band a negative one. We obtain the theoretical effective masses from parabolic fits to the band dispersions. For the σ-resonance, the effective mass is $2.1m_e$, whereas for the π-resonance it depends on momentum. Specifically, it is $-0.7m_e$ along Γ-K and $-1.9m_e$ along Γ-M, whereas in Figure 4.2 we measure along the Γ-K. For

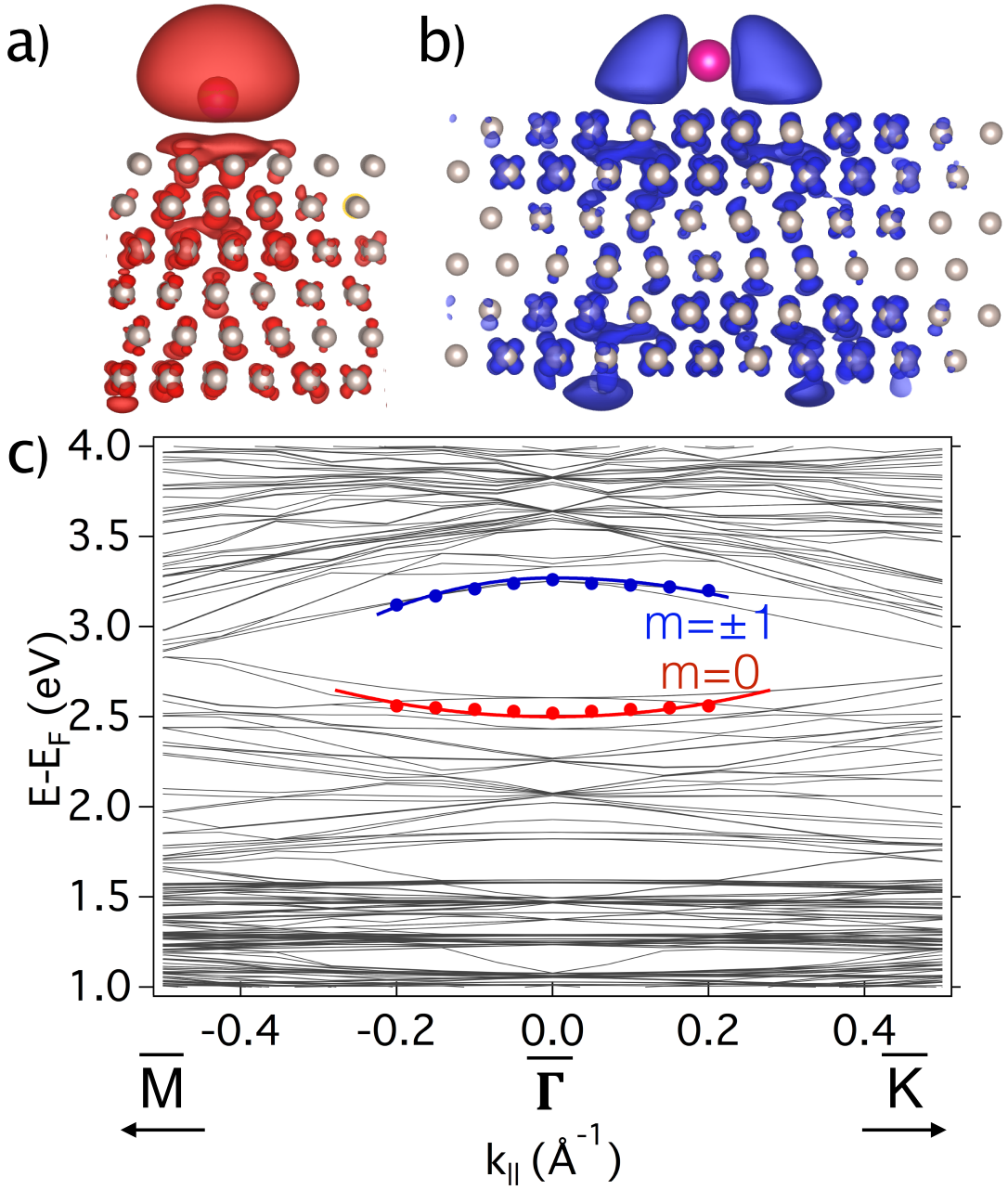

Figure 4.6: **(a)** and **(b)** The spatial orbital distributions of the m=0 and m=±1 σ- and π-resonances of Rb atom on Ru(0001) surface. **(c)** The calculated electronic band structure of Rb on Ru(0001) using a 6×6 super cell. The red and blue dots and lines indicate the calculated σ- and π-resonance bands.

comparison, we have also calculated the band structures of Rb in atop position on Cu(111) using a 6×6 super cell, and find both the σ- and π-resonances to be non-dispersive shown in Figure 4.7. The same result is obtained when Rb is placed in a hollow site on Cu(111) surface.

The surface band structure results obtained by DFT calculations confirm that there is substrate mediated interaction between low-density alkali atoms for the Ru(0001) but not for the Cu(111) surface. To understand this substrate effect, in Figure 4.6(a) and (b) we plot the spatial distribution of orbitals that contribute to the σ- and π-resonances of Rb/Ru(0001) system. As in the case of alkali atoms on noble metals, the σ-resonance has main contributions form the 5s and $5p_z$ orbitals, which hybridize in the presence of the surface. For the π-resonance the dominant contributions are from the Rb $5p_x$ and $5p_y$ orbitals, which hybridize with the Ru $3d_{xz}$ and $3d_{yz}$. The hybridization of Rb with the Cu(111) and Ru(0001) surfaces is different, however. For the adsorption of Rb on on Ru(0001) one can see significant contribution from the d orbitals of Ru(0001) to both the σ- and π-resonances (Figure 4.6(a) and (b)). By contrast, for Cu(111) there is only small contribution from the s and p orbitals in Figure 4.7. For both surfaces we expect that the resonant sp-bands of the substrates interact weakly with the adsorbates due to presence of the band gaps. The difference between Ru(0001) and Cu(111) are the energies and bandwidths

of the d-bands. For Ru, the 4d-bands extend from -6.0 eV to as high as 1.5 eV relative to E_F according to our DFT calculations. In the case of Cu, the 3d-bands spread from -5.0 to -2.0 eV below the E_F; they are fully occupied and have a narrower bandwidth than for Ru(0001).[104] Therefore the empty 4d-bands on Ru(0001), are much closer in energy to the alkali induced resonances, and are more diffuse than the 3d-bands of Cu(111). This enables more effectively hybridization of the σ- and π-resonances via the interactions with the d-bands of the Ru(0001) substrate. This explains the strong substrate mediated dispersion of the σ- and π-resonances, and points to a different character of alkali chemisorption on transition metals as compared with the noble metals.

4.4 ULTRAFAST PHOTOEXCITATION DYNAMICS

In this section, I will describe interfereometric measurements of phase and energy relaxation in 3PP processes involving excitation of the Cs and Rb resonances. The procedures for analysis of interferometric two-pulse correlation measurements (I2PC) was described in Chapters 2 and 3.

We explored the photoexcitation dynamics for both the alkali induced resonances of Cs and Rb by recording I2PC scans.[77] Figure 4.8(a) shows an experimental 2D interferogram

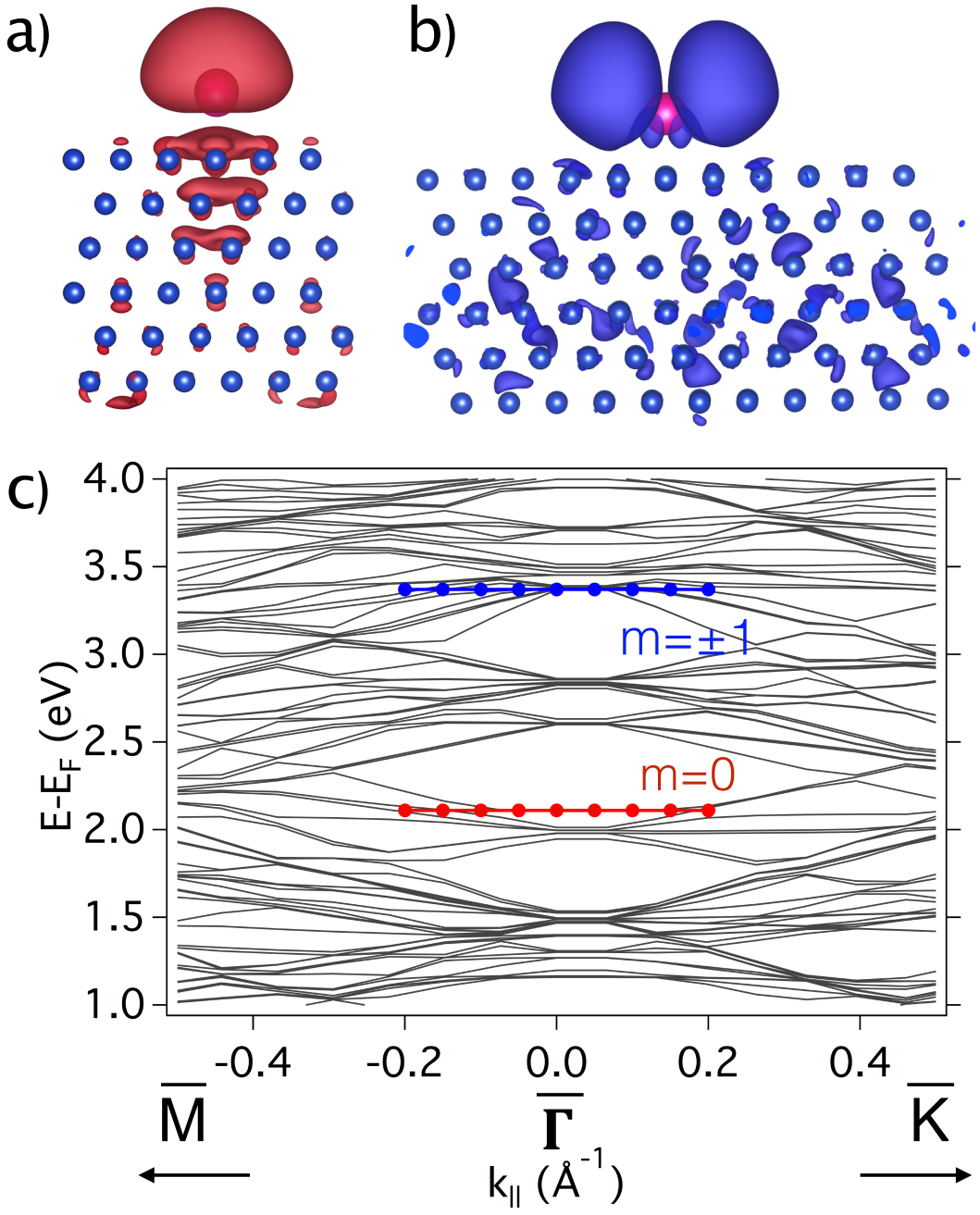

Figure 4.7: (color online) **(a)** and **(b)** The spatial orbital distributions of the m=0 and m=±1 σ- and π-resonances of Rb atom on Cu(111) surface. **(c)** The calculated electronic band structure of Rb on Cu(111) using a 6×6 super cell. The red and blue dots and lines indicate the calculated σ- and π-resonance bands.

for $k_{||}$=0Å^{-1}, which is extracted from a 3D $E(k,t)$ movie for the Cs/Ru(0001) system under approximately the same conditions as in Figure 4.2(d) using 2.14 eV excitation. Figure 4.9(a) and 4.9(b) shows cross sections through the data in Figure 4.8(a) at the energies of the σ- and π-resonances, which are indicated by the red and blue lines through Figure 4.8(a). These I2PC scans reflect the electron dynamics associated with the coherent and incoherent 3PP excitation pathways involving the σ- and π-resonances.

A graphic way to evaluate the polarization and population dynamics associated with the 3PP process in Figure 4.8(a) is by performing a Fourier transform (FT) of the data with respect to time. The result of this analysis gives the 2D FT images of the coherent linear and nonlinear polarization involved in the 3PP process *vs.* the final state energy, which are shown in Figure 4.8(b)-(d); The FT signal has components from the incoherent population dynamics ($0*\hbar\omega_l$), the coherent polarization at the fundamental frequency ($1*\hbar\omega_l$), and at its second harmonic frequency ($2*\hbar\omega_l$), which are plotted *vs.* the photoelectron energy. The $3*\hbar\omega_l$ component, which also contributes to the 3PP process, is too weak to consider in the present analysis. The $0*\hbar\omega_l$ component is sensitive to the incoherent population dynamics of electrons promoted to the intermediate states, whereas the $1*\hbar\omega_l$ and $2*\hbar\omega_l$ components reflect the linear and second-order nonlinear polarizations that contribute to the coherent pathways in the 3PP process.

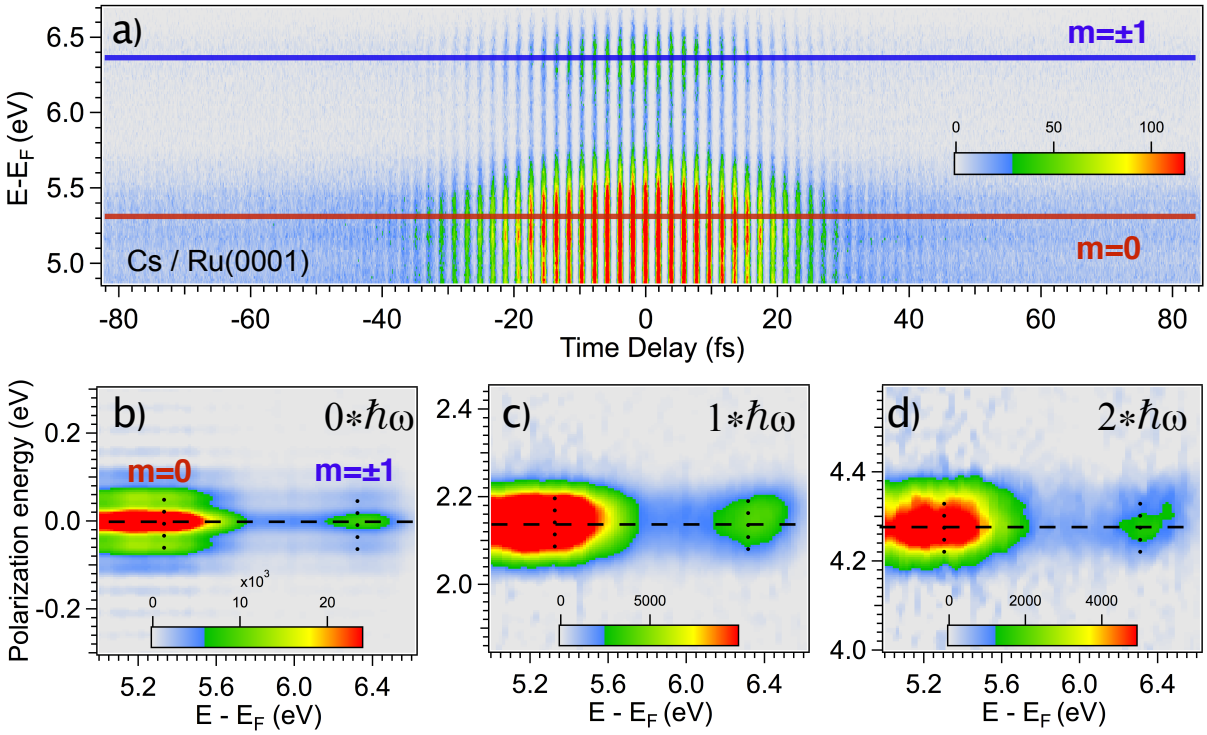

Figure 4.8: (color online) **(a)** An interferogram representing a cut through a 3D movie $[E(k,t)]$ of mPP from Cs/Ru(0001) surface for $k_{||}$=0 Å^{-1}. The measurement is performed with $\hbar\omega$=2.14 eV for ∼0.015 ML Cs/Ru(0001) at 90 K. The red and blue lines indicate the energies of m=0 and m=±1 σ- and π-resonances where cuts through the interferogram give the I2PC scans in Figure 4.9. **(b)-(d)** The 2D photoelectron spectra obtained by Fourier transforming interferometric scan in **(a)** showing individually components at zero frequency **(b)** and first **(c)** and second **(d)** harmonics of the laser frequency $\hbar\omega$. The horizontal dashed lines indicate the laser energy $\hbar\omega$ with different polarization orders. The vertical dotted lines indicate the final energy of σ- and π-resonances.

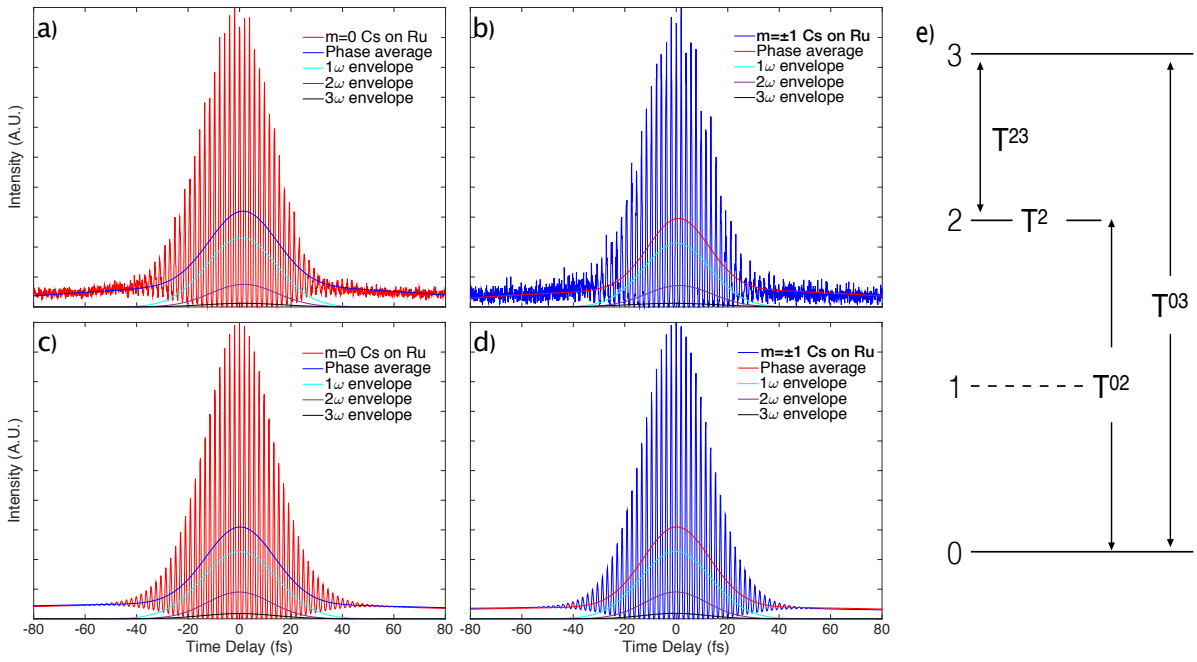

Figure 4.9: (color online) **(a)** and **(b)** I2PC scans for the σ- and π-resonances obtained from the interferogram in Figure 4.8(a) for Cs/Ru(0001). The signal is decomposed into envelopes of components oscillating with different frequencies (see text in details), which are used to fit the polarization and population decay parameters. **(c)** and **(d)** The simulated I2PC signals for these two resonances form a fit to an OBE model. **(e)** The diagram of four-level excitation.

The 2D plots give a correlation between populations and polarization frequencies excited in the sample and the final photoelectron state spectra where the mPP process terminates.[77] In a purely coherent process the slope by which a 2D spectral feature tilts should reflect the order of the coherent process. For example, in a 3PP process from an initial state that is localized in energy, we expect a coherent three-photon absorption to have a slope of 1/3 in Figure 4.8(e) because three photons corresponding to polarization at a particular energy (abscissa) sum to generate the signal at the corresponding final state energy (ordinate). In the case of inhomogeneous broadening, however, for example if the initial state is a d-band, which disperses with perpendicular momentum, different polarization energies within the laser pulse can contribute to the same final state energy. As a result, the 2D spectra do not tilt and a vertical cross section through a 2D spectrum at $1 * \hbar\omega_l$ just reflects the laser spectrum. The 2D spectra can also be influenced by dephasing in the intermediate states, which leads to loss of phase memory in the mPP process. In this case, the 2D spectra have tilted and horizontal contributions from the coherent and the dephased processes.[77]

Examining the 2D spectra for the linear and second-order polarizations in Figure 4.8(c) and 4.8(d) we find them to be essentially flat except for the π-resonance at the highest final state energies. Based on the projected band structure in Figure 4.4(a), we can assert that the σ-resonance is excited from d-bands at <1 eV below E_F possibility via a resonance with

Table 2: The polarization and population decay parameters from the OBE simulation in Figure 4.8.

	T^2 (fs)	T^{23} (fs)	T^{02} (fs)	T^{03} (fs)
m=0 Rb	40	11	10	16
m=0 Cs	39	8	6	4
m=±1 Rb	24	3	14	17
m=±1 Cs	22	3	9	13

an unoccupied d-band at 0.9-1 eV above E_F. The coupling to the dispersive bulk bands probably contributes to the inhomogeneous broadening and hence explains in part the lack of tilting of the σ-resonance signal in the 2D spectra in Figure 4.8(c) and 4.8(d). In the case of the π-resonance the slight tilting of the 2D spectra can be attributed to excitation from a narrow region about E_F. Because the phase space for electron-electron (e-e) scattering goes to zero at E_F and T=0, and grows rapidly with $(E - E_F)^2$ dependence away from E_F, [72, 83, 82] the polarization associated with excitation from or to E_F is expected to dephase relatively slowly. Similar reduced dephasing rate for initial states near E_F is commonly observed in I2PC scans.[73] Therefore, we expect the two-photon coherence excited from the substrate bands at E_F to the π-resonance to be somewhat protected from the effects of inhomogeneous broadening and e-e scattering.

In Figure 4.9 we analyze the alkali resonance photoexcitation dynamics with the optical Bloch equation (OBE) approach. We note that the OBE approach is only rigorous in for an isolated system where local field effects are not important, and that it is difficult to treat inhomogeneous broadening that is inherent to a solid state or surface system.[75, 77] Therefore, here we assume a minimal system for OBE simulation with the understanding that the extracted dephasing times are effective parameters, and should not be taken as a precise measurement of dephasing of the alkali atom σ- and π-resonances. The excited state population lifetimes are more meaningful, except that the parameters could be associated with either the intermediate d-band or alkali resonance states, which are excited by one or two photon processes. In this case we assume that the bulk d-band lifetime is shorter than the alkali surface state lifetime; this assumption is grounded in extensive literature on the electron relaxation in metals and metal surfaces.[62, 86, 105, 106]

The OBE simulation is based on the data for Cs/Ru(0001) in Figure 4.9(a) and 4.9(b), which corresponds to the I2PC cross sections from Figure 4.8(a) at the σ- and π-resonance energies for $k_{||}$=0 Å^{-1}. The I2PC results are similar for other photoemission angles. The corresponding simulated I2PC simulation results are given in Figure 4.9(c) and 4.9(d). The energy level scheme and the key parameters for the simulation are given in Figure 4.9(e). We use a four level scheme, where "0" and "3" are the initial and the final states, "1" is

virtual, and "2" is the alkali atom resonance. Treating "1" as a virtual state is reasonable if the intermediate d-band dephasing an population decay are much faster than for the alkali resonances. The main parameters in the simulation are T^2, the alkali resonance population decay time, and T^{23}, T^{02}, and T^{03}, the dephasing times of the linear, second-order, and third-order polarizations. The simulation is performed using similar analysis method as in Ref. [62], where the I2PC signal is decomposed into the phase average, and the envelopes of the ω, 2ω and 3ω oscillations. In order to simulate the experimental I2PC scans, the OBE calculation is performed until the calculated envelopes reproduce the experimental ones. In the simulation, the autocorrelation of the laser pulse is decomposed with the same method as described above, and the pulse duration is $\sim$20 fs based on the analysis from the envelopes for the polycrystalline molybdenum sample holder. For the non-oscillating wings of in the autocorrelation trace, we consider that the laser has a liner chirp. To obtain the information of the population and coherent decay of the alkali resonances more precisely, we include linear chirp term into the electric field of our laser pulse. Table 2 presents the best fit parameters for Cs/Ru(0001) data in Figure 4.9 and that obtained for Rb/Ru(0001) under similar coverage and laser excitation conditions.

The fitting results give approximately 40 and 20 fs lifetime for the Cs and Rb σ- and π-resonances on Ru(0001). With the caveat that these lifetimes could contain a contribution

from the d-bands of Ru(0001), we believe that these results are determined with an uncertainty of ∼10 fs based on the sensitivity of the values on how the simulations are performed. The lifetimes of the σ-resonances are are similar, though faster, than those measured for the Cu(111) surface where a non-exponential decay due to the nuclear motion on the excited state potential surface was consistent with a 50 fs lifetime.[55, 105] We expect a shorter lifetime for alkali atoms on Ru(0001) surface because the large density of states of the occupied and unoccupied d-bands can enhance decay channels via inelastic electron scattering with respect to the Cu(111).[37] As far as the dephasing times are concerned, we cannot exclude that the parameters are not significantly affected by systematic errors, such as the incomplete characterization of the laser pulse. Further experiments, such as the temperature dependence of the dephasing rates, would be necessary to confirm their physical significance.

5.0 THE ELECTRONIC STRUCTURE AND PHOTOEXCITATION DYNAMICS OF ALKALI ATOMS ON CU(111)

This chapter describes the electronic structure of chemisorbed alkali atoms (Rb and Cs) on clean the noble metal Cu(111) surface. As mentioned in the previous chapter, the electronic structure of alkali atoms on noble metals was studied previously with 3.1 eV excitation and with 1D (energy) photoelectron detection. The ability to tune the excitation and image energy-momentum photoelectron dispersions reveals new aspects of this well studied chemisorption system.

5.1 EXPERIMENTAL PROCEDURES

The experimental methods used here are similar to those in the previous chapter on the alkali/Ru(0001) system. The clean Cu(111) surface is prepared by repeated cycles of Ar^+

sputtering and annealing at 850 K in ultrahigh vacuum (UHV). The Rb or Cs atom coverage is estimated to be below 0.01 monolayer (ML) for most of the reported spectra, based on the observed work function change.[12, 107] At these coverages we can assume that alkali atoms are not interacting with each other on the surface; they form a hexactic liquid phase due to the dipole-dipole repulsion.

The photoexcitation source for the mPP measurements is the NOPA system as for the Rb expreiments. p-Polarized light is focused onto the Cu(111) surface to a spot of $\sim$100 μm diameter. The angle between the incident beam and the axis of the analyzer is fixed at 45°. As we discussed before, the analyzer has an angular acceptance of $\pm$15°; for a broader angular coverage, the sample can be rotated perpendicular to the optical plane. Angle-resolved photoemission spectra are recorded with the Specs Phoibos 100 electron energy analyzer equipped with a 3D delay-line detector, as described in Chapter 2. The momentum dispersion direction is in the optical plane; this causes the optical transition moments for positive and negative parallel momentum, $k_{||}$, to be different, and therefore the angular mPP intensity distributions to be asymmetric.[108]

5.2 SPECTROSCOPIC FEATURES ON ALKALI/CU(111) SURFACE

In this section, I will describe the spectroscopic features of the alkali/Cu(111) system, for different excitation wavelengths.

5.2.1 Clean Cu(111) Surface

The angle-resolved mPP spectrum of the clean Cu(111) surface is presented in Figure 5.1(a) for excitation by $h\nu$=1.92eV (645nm) light. The corresponding surface-projected electronic structures of clean Cu(111) and Cs/Cu(111) with possible excitation pathways for 3PP and 4PP processes are shown in Figure 5.2(b).

For the clean Cu(111) surface, the spectrum is dominated by two characteristic peaks: i) the occupied Shockley surface state (SS), and ii) the unoccupied n=1 image potential state (IP), marked in Figure 5.1(a).[109] The work function of Cu(111) is found to be 4.82 eV. The SS is located within the L-projected band gap of the copper surface with a band minimum of $\sim$-0.29$\pm$0.03 eV relative to E_F at the center of the surface Brillouin zone; its band dispersion corresponds to an effective mass m^*=0.4$\pm$0.02m_e, where m_e is the free electron mass.[18, 76] SS is excited via a non-resonant 3PP process for the 1.92 eV excitation light. The IP state is excited from the bulk sp-band by a 4PP process. A fit of the IP state dispersion yields

an effective mass m^*=0.9±0.02m_e and binding energy of 0.7±0.03eV relative to the vacuum level, E_v, in good agreement with the previous work.[21, 110] Since IP state photoemission is a higher-order process that for the SS, it appears with weaker intensity in 5.1(a).

5.2.2 Alkali atom resonances on Cu(111) surface

Figure 5.1(a)-(d) shows two-dimensional $E(k)$ distribution images measured with 645 nm (1.92 eV) three- and four-photon excitation during the deposition of Cs onto Cu(111) surface. Cross sections through the $E(k)$ distributions for the normal emission ($k_{||}$=0 Å^{-1}) are shown in Figure 5.1(e) for more quantitative visualization of the data. Upon adsorption of < 0.01 ML Cs onto a clean Cu(111) surface, we observe two new features, which are indicated as m=0 [12, 52, 105] and m=±1 [13] accordingly in 5.1(b). On depositing more Cs on the Cu(111) surfaces, these two features get stronger and more dominant. In angle resolved spectra, they do not disperse with electron momentum parallel to the surface, which is expected for a state localized on Cs or Rb adatoms. We already noted that this behavior contrasts our previous work of the alkali atoms on Ru(0001).[111] Based on the previous 2PP studies of alkali/Cu(111) and alkali/Ag(111) surfaces, these two features are assigned to antibonding σ-resonance (m=0) and π-resonance (m=±1), and these assignments provide the symmetries of these two features. As described in previous work, π-resonance has the minimum intensity

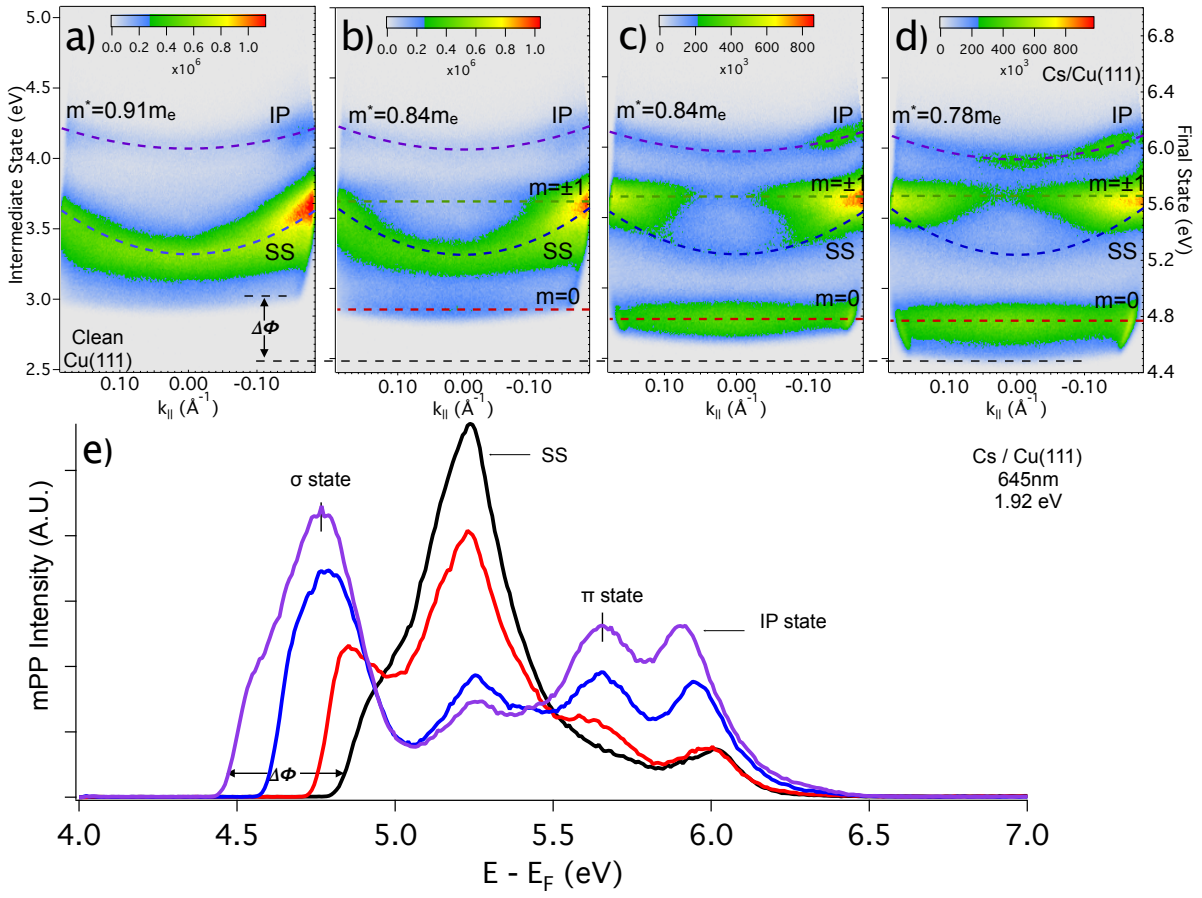

Figure 5.1: **(a)-(d)** 3PP and 4PP spectra of the Cu(111) surface excited $\hbar\omega$=1.92 eV during the continuous deposition of Cs atoms starting from zero coverage. The spectra show the penultimate state energy (left axis) and the final photoelectron energy relative to E_F (right axis) *vs.* the parallel momentum, $k_{||}$. $\Delta\Phi$ gives the work function change before and after the deposition. The dashed straight or parabolic lines give the best fitting dispersions of specific bands. In **(a)** the fitting of the IP state gives the effective mass marked in each figure, while the SS has m^*=0.4±0.02m_e. **(e)** The line profiles of **(a)-(d)** that are taken at $k_{||}$=0 Å^{-1}.

at $k_{||}$=0, the Γ point, which is clearly shown in Figure 5.1(d).[13] In addition, for large parallel momenta in angle resolved spectra, with photon energy of $\hbar\omega$=1.92eV, it is possible to drive a resonant transition from SS to m=±1 state by a two photon transition, which enhances the π-resonance signal, as shown in Figure 5.2(b).

Moreover, the alkali atoms being ionized upon chemisorption form strong dipoles. These dipoles create a surface dipole field, which affects the mPP spectra. The energies of σ- and π-resonances depend on the alkali atom coverage through interaction with the surface dipole field. Moreover, the dipole field also reduces the work function Φ of the substrate, according to $\Delta\Phi^{3/2}$.[13, 64] To address the energy positions of σ- and π-resonances, the mPP spectra are recorded as Cs coverage increased; and the line profiles of these spectra taken at $k_{||}$=0 Å^{-1} are summarized in Figure 5.3. To remove the effect of the surface dipole potential on the σ and π-resonances energies, we extrapolate the results to zero alkali coverage. In Figure 5.4 we plot the σ- and π-resonance energies for Cs and Rb on Cu(111) surface *vs.* $\Delta\Phi^{3/2}$, and indeed find a linear trend.

From the linear fits to the data in Figure 5.4, we can obtain the σ-resonance energy for Cs and Rb on Cu(111) at the zero coverage limit to be 2.90 and 2.85 eV with respect to E_F accordingly, and the π-resonance energy for both Cs and Rb is 3.74 eV with respect to E_F. Therefore σ - π splittings for Cs and Rb are 0.84 and 0.89 eV, which are comparable

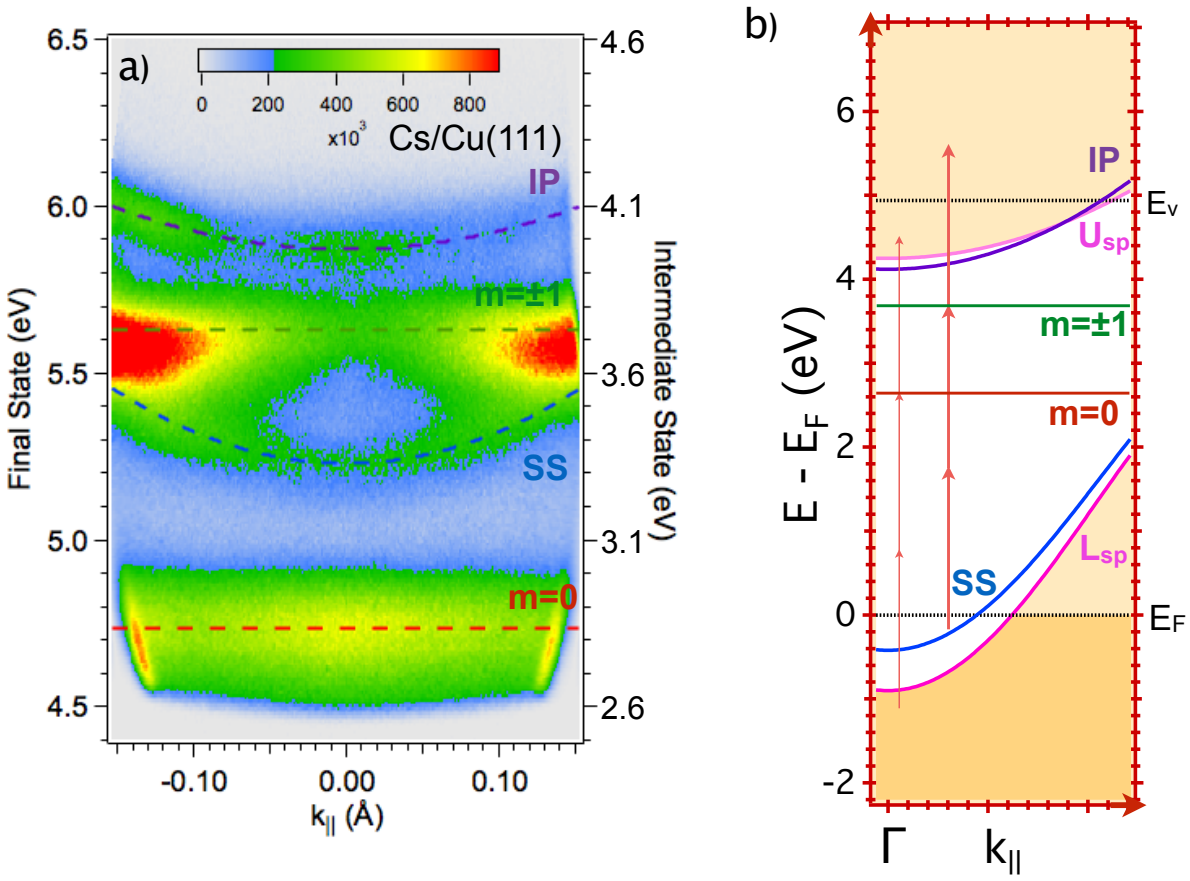

Figure 5.2: **(a)**The 3PP/4PP spectrum with $\hbar\omega$=1.91eV excitation of Cs/Cu(111) surface. **(b)**The surface-projected band structure as a function of $k_{||}$ showing the 3PP and 4PP excitation processes through the alkali-induced resonance intermediate states. The regular red arrows show the possible transitions from bulk of the Cu substrate to m=0 with $\hbar\omega$=1.91eV and the bold red arrow gives the resonant transitions from SS to $m = \pm 1$ at higher $k_{||}$.

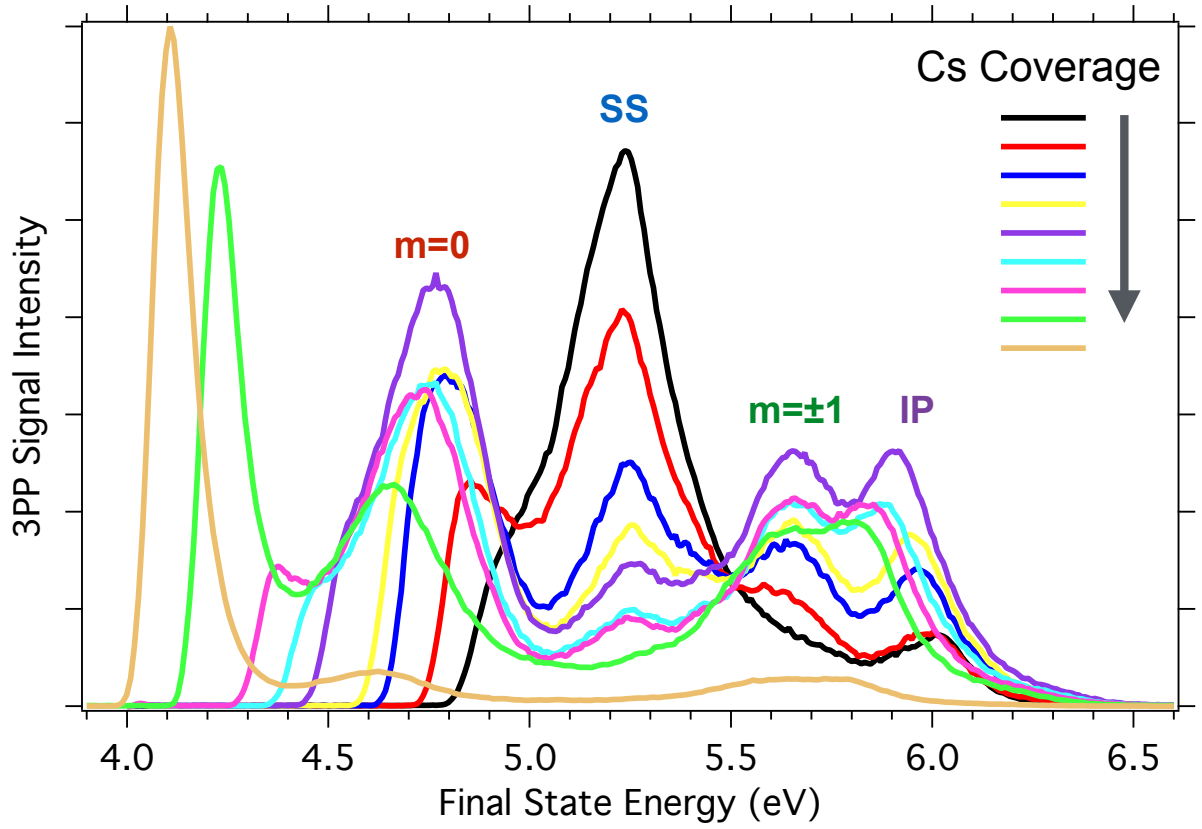

Figure 5.3: The series of line profiles of 3PP spectra taken at $k_{||}$=0 $\mathring{A}^{-1}$ as Cs coverage increases

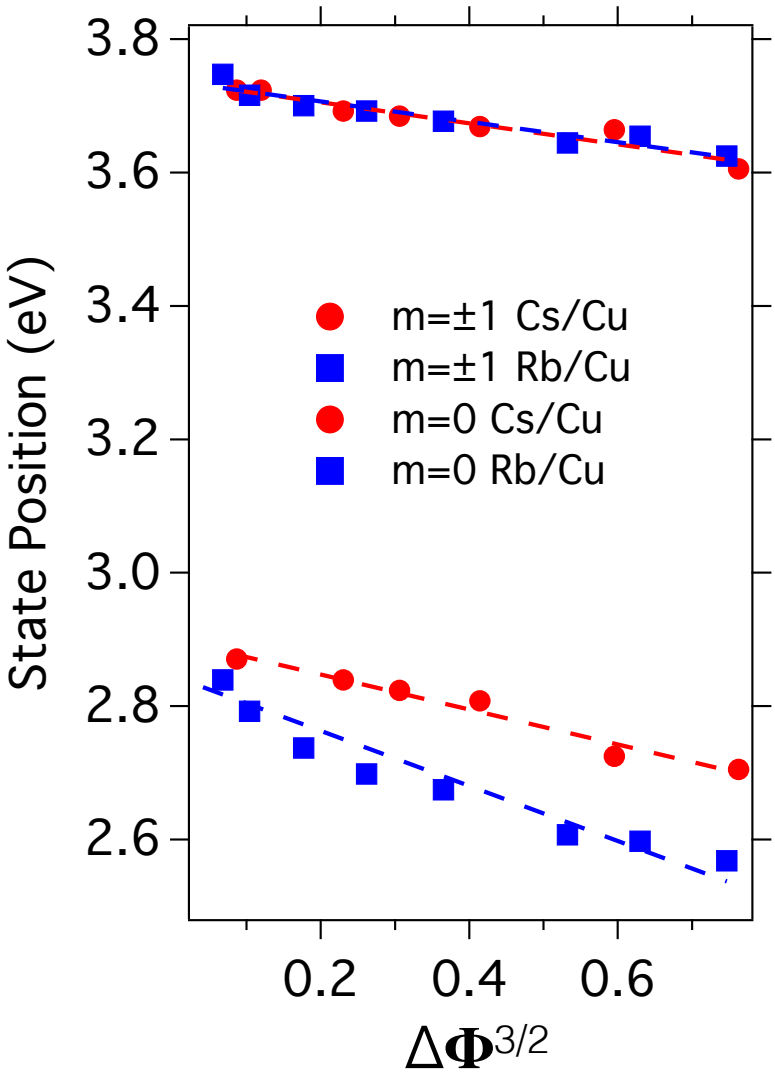

Figure 5.4: The binding energies of m=0 and m=±1 σ- and π-resonances relative to the E_F for Rb and Cs on Cu(111) surface, plotted versus work function change to the power of 3/2 ($\Delta\Phi^{3/2}$). Dashed lines are linear fits to the data.

to the calculated zero coverage splittings for noble metal surfaces.[12, 14] To compare with the alkali atoms on Ru, the σ-resonance energies for Cs and Rb on Ru(0001) at the zero coverage limit are 3.59 and 3.33 eV with respect to E_F and the π-resonance energies are 4.32 and 4.13 eV. Thus the splitting for Cs and Rb on Ru(0001) are 0.73 and 0.80 eV, which are smaller than the ones on Cu(111).

5.3 ULTRAFAST PHOTOEXCITATION DYNAMICS

Furthermore, we explored the photoexcitation dynamics for both the alkali induced resonances of Cs and Rb by recording interferometric two-pulse correlation measurements (I2PC). Figure 5.5(c) shows an experimental 2D interferogram for $k_{||}$=0 Å^{-1}, which is extracted from a 3D $E(k,t)$ movie for the Cs/Cu(111) system and the corresponding mPP spectra is in Figure 5.5(a) using the $\hbar\omega$=1.97 eV excitation. Figure 5.5(d)-(g) shows cross sections through the data in Figure 5.5(c) at the energies of SS, IP, σ- and π-resonances, which are indicated by different color lines through Figure 5.5(c). These I2PC scans reflect the electron dynamics associated with the coherent and incoherent 3PP excitation pathways.

Similar to the analysis in Chapter 4, a series of Fourier transforms (FT) are performed to the 2D interferometric spectra with respect to time. The result of this analysis gives

the 2D FT images of the coherent linear and nonlinear polarization involved in the 3PP process *vs*. the final state energy at different $k_{||}$ points, which are shown in Figure 5.5(h). The FT signal also includes components from the incoherent population dynamics ($0 \times \hbar\omega_l$), the coherent polarization at fundamental frequency ($1 \times \hbar\omega_l$), and at its second harmonic frequency ($2 \times \hbar\omega_l$), which are ploted *vs*. the photoelectron enegy in each image. Here the ($3 \times \hbar\omega_l$) is too weak to consider in this analysis. As mentioned above, at higher angle, a resonant transition occurs from SS to π-resonance, which gives the strongest signal in the righthand side of Figure 5.5(h).

In addition, Figure 5.6 gives another example of Rb on Cu(111) system under photon energy $\hbar\omega$=1.97 eV. Figure 5.6 is taken for the same experimental parameters as Figure 5.5 and analyzed in the same way. However, other than the information I described above, more features are observed. The dashed arrows in Figure 5.6(b) and (c) point out the extra frequency components taken at σ-resonance in the 2D FT images at different $k_{||}$ points, which are not at the integer multiples of the laser frequency. These satellite components correspond roughly to $\frac{1}{3} \times \hbar\omega_l$, $\frac{2}{3} \times \hbar\omega_l$ and $\frac{5}{3} \times \hbar\omega_l$. More evidence can be observed in the I2PC scans of the σ-resonance in Figure 5.6(e) and (f) (red line profiles). Here the interferometric two-pulse correlations (I2PCs) do not follow the third-order autocorrelation of a Gaussian pulse or some modification of it due to finite polarization dephasing as the other two states.

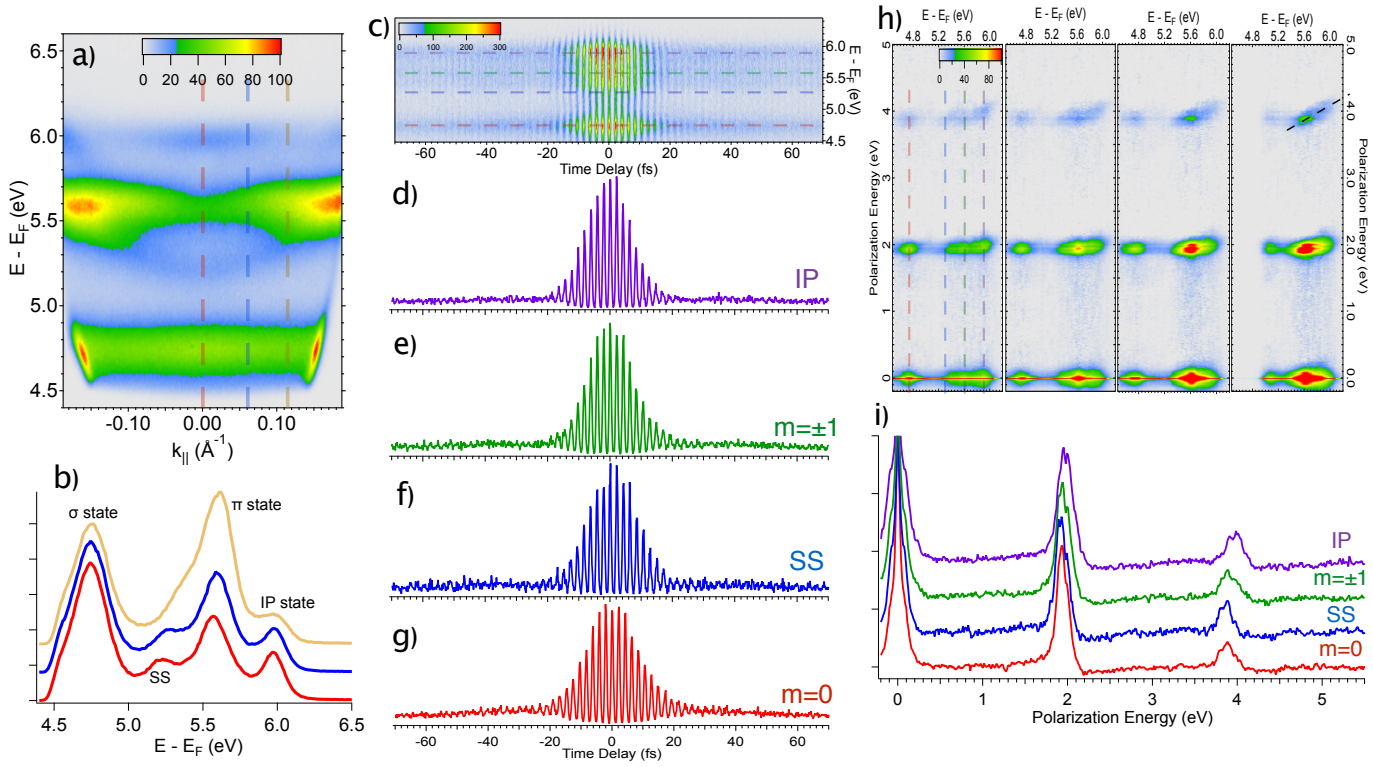

Figure 5.5: **(a)**The 3PP/4PP spectrum with $\hbar\omega$=1.97 eV excitation of Cs/Cu(111) surface. **(b)**The line profiles taken at different $k_{||}$ marked in **(a)**. **(c)**The interferogram representing the cut through a 3D movie $[E(k,t)]$ of **(a)** from Cs/Cu(111) surface for $k_{||}$=0 Å^{-1}. **(d)-(g)** I2PC scans for the states, including σ- and π-resonances, marked in **(c)**. **(h)** The 2D photoelectron spectra obtained by Fourier transforming interferometric scan taken at different $k_{||}$. **(g)** The line profiles for different state energies marked in the 2D photoelectron spectra to show the components at zero, first and second harmonics of the laser frequency $\hbar\omega_l$.

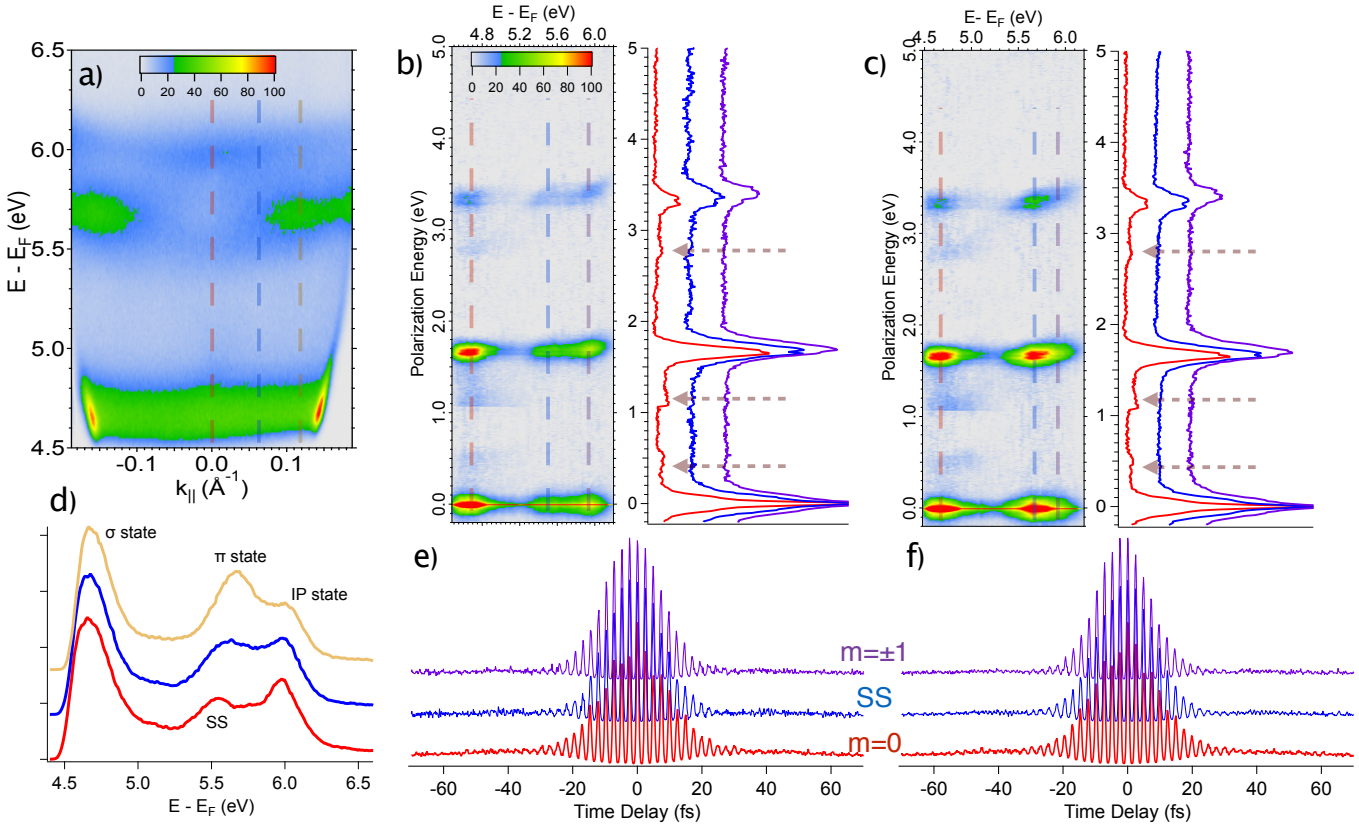

Figure 5.6: **(a)**The 3PP/4PP spectrum with $\hbar\omega$=1.97 eV excitation of Rb/Cu(111) surface. **(d)**The line profiles taken at different $k_{||}$ marked in **(a)**. **(b)** and **(c)** The 2D photoelectron spectra obtained by Fourier transforming interferometric scan from Cs/Cu(111) surface for $k_{||}$=0 Å^{-1} and $k_{||}$=0.12 Å^{-1} with the line profiles at different state energies on the right side correspondingly. The dashed arrows are pointing to the extra features other than the component peaks at zero, first and second harmonics of the laser frequency $\hbar\omega_l$. **(e)-(f)** I2PC scans for the states marked in **(b)** and **(c)**.

Moreover, there is obvious coherent beating every three optical cycles, in agreement with the denominator of the non-integer multiples of the laser frequency. This coherent beating is responsible for the extra non-integer frequency components in the 2D spectra noted above. Apparently, the excitation pulses create frequency components of the coherent polarization that are outside the laser bandwidth only in the case of the 3PP through the σ-resonance. This is an apparent violation of energy-time uncertainty, and will be addressed in the next chapter.

6.0 POLARIZATION BEATING OF CHEMISORBED ALKALI ATOMS ON CU(111)

In this chapter, I will discuss the details of polarization beating phenomena and multi-electron dynamics process upon charge transfer excitation of alkali/Cu(111) that I mentioned in last chapter.

6.1 ULTRAFAST PHOTOEXCITATION RESULTS

The angle-resolved mPP spectrum of the Rb/Cu(111) surface is presented in Figure 6.1(a) for excitation with $\hbar\omega$=1.91 eV (650 nm) light; the surface coverage of Rb is estimated to be <0.01 ML. The corresponding surface-projected electronic structures and possible excitation pathways for 3PP and 4PP processes are shown in Figure 6.1(b). Similar to the Cs/Cu(111) system, at high emission angles, there is a two-photon resonant transition is from SS to

π-resonance, which is marked with bold red arrows in Figure 6.1(b). Note that the most intense feature in the spectrum of Figure 6.1(a) is the σ-resonance, for which there is no resonant excitation pathway from surface state of Cu(111). The excitation mechanism of σ-resonance is the main topic of this chapter.

Figure 6.2(a) shows the experimental 2D interferogram for $k_{||}$=0 Å^{-1} using $\hbar\omega$=1.91 eV excitation, which is extracted from a 3D $[E(k,t)]$ movie for the Rb/Cu(111) surface shown in Figure 6.1(a). Figure 6.2(b)-(e) give the cross sections through the data in Fig 6.2(a) at the energies of the SS, IP, σ- and π-resonances peaks, which are marked by different color lines. These I2PC scans reflect the electron dynamics associated with the coherent and in coherent 3PP excitation pathways. The immediately notable aspect of the I2PC of the σ-resonance in Figure 6.2(e) is that the polarization oscillation amplitudes are modulated, such that they deviate dramatically from the envelope of the third-order autocorrelation function for the same pulse.

The arrows in Figure 6.2(e) point to every third fringe, which have enhanced amplitude with respect to their neighboring fringes. Thus the modulation of the polarization oscillations occurs every three cycles, or with a period of 6.5 fs. In order to analyze further, a series of Fourier transforms is performed on the 2D interferometric spectra with respect to time for different emission angles. The result of this analysis gives the 2D FT images of the coherent

linear and nonlinear polarization involved in the 3PP process *vs.* the final state energy at different $k_{||}$ points, shown in Figure 6.3. Other than the dominant components of the spectra at the integers of fundamental frequency, which must appear for a 3PP process, there are three additional satellite components corresponding roughly to $\frac{1}{3} \times \hbar\omega_l$, $\frac{2}{3} \times \hbar\omega_l$ and $\frac{5}{3} \times \hbar\omega_l$. The denominator of 3 explains why every third fringe is enhanced to produce the observed polarization beating behavior in Figure 6.2(e). The 2D-FT spectra in Figure 6.3 further show that the satellite frequency components only appear for the σ-resonance excitation pathway, and they are essentially independent of the photoelectron $k_{||}$. The latter fact is expected because the σ-resonance excitation is localized on the Rb atom and therefore its 3PP spectral peak is non-dispersive.

To gain a deeper understanding of the polarization beating phenomenon, I investigate whether it is specific to a certain photoexcitation energy range. Therefore, the same two-pulse correlation measurements are performed for different photon energies (wavelengths). Figure 5.5, 6.2 and 6.4 present three measurements for Rb/Cu(111) and Cs/Cu(111) surface at 1.97, 1.91 and 1.84 eV (630, 650 and 675 nm), respectively. Because 675 nm is almost at the upper boundary of our THG pumping range, the spectra and I2PC scans are not as good as the other two wavelengths. I use the Cs and Rb spectra interchangeably, because the polarization beating phenomenon is observed for both in a rather similar manner. This

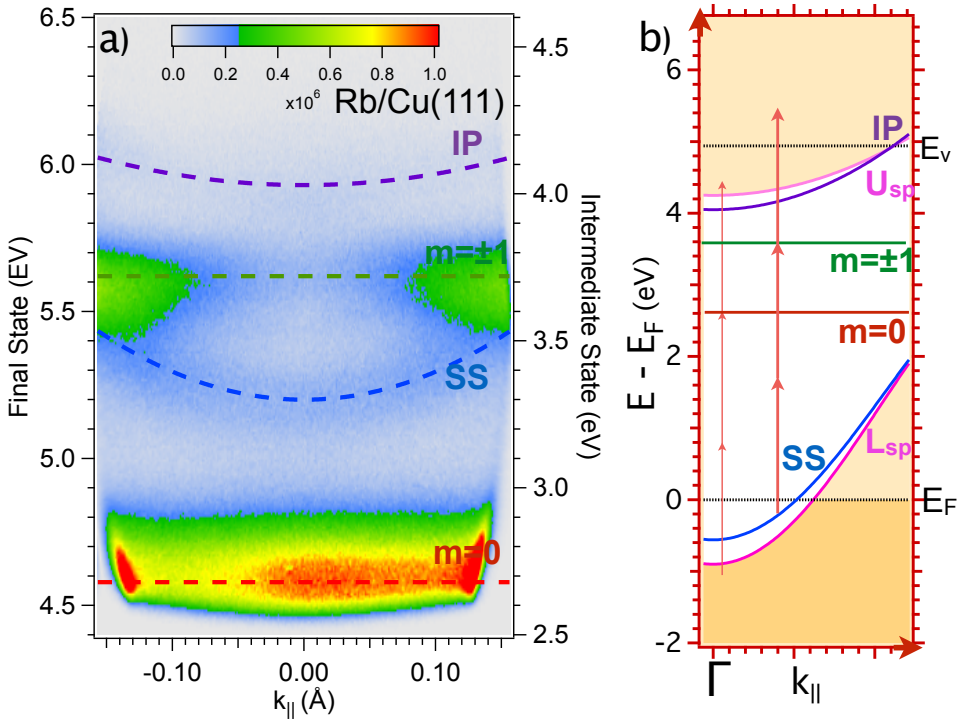

Figure 6.1: **(a)**The 3PP/4PP spectrum with $\hbar\omega$=1.91eV excitation of Rb/Cu(111) surface. **(b)**The surface-projected band structure as a function of $k_{||}$; the white region corresponds to the projected band gap. The thin red arrows show the possible transitions from bulk of substrate Cu to m=0 with $\hbar\omega$=1.91eV and the bold red arrows gives the resonant transitions from SS to $m = \pm 1$ at higher $k_{||}$.

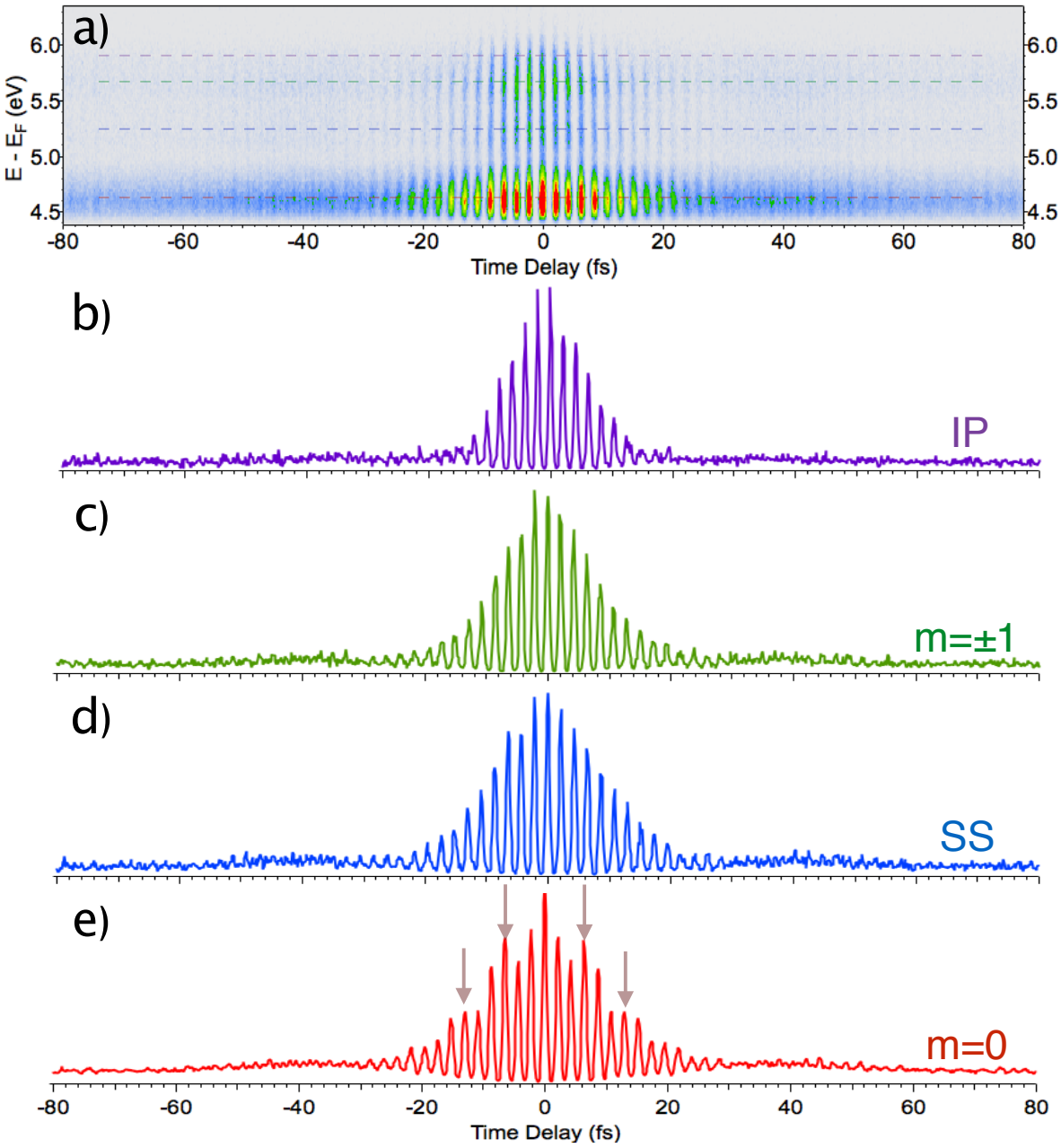

Figure 6.2: **(a)** The interferogram representing the $k_{||}$=0 Å^{-1} cut through a 3D movie $[E(k,t)]$ of Figure 6.1(a) from Rb/Cu(111) surface. **(b)-(e)** I2PC scans for the states marked in **(a)**. Arrows in **(e)** indicate the polarizaton beatings.

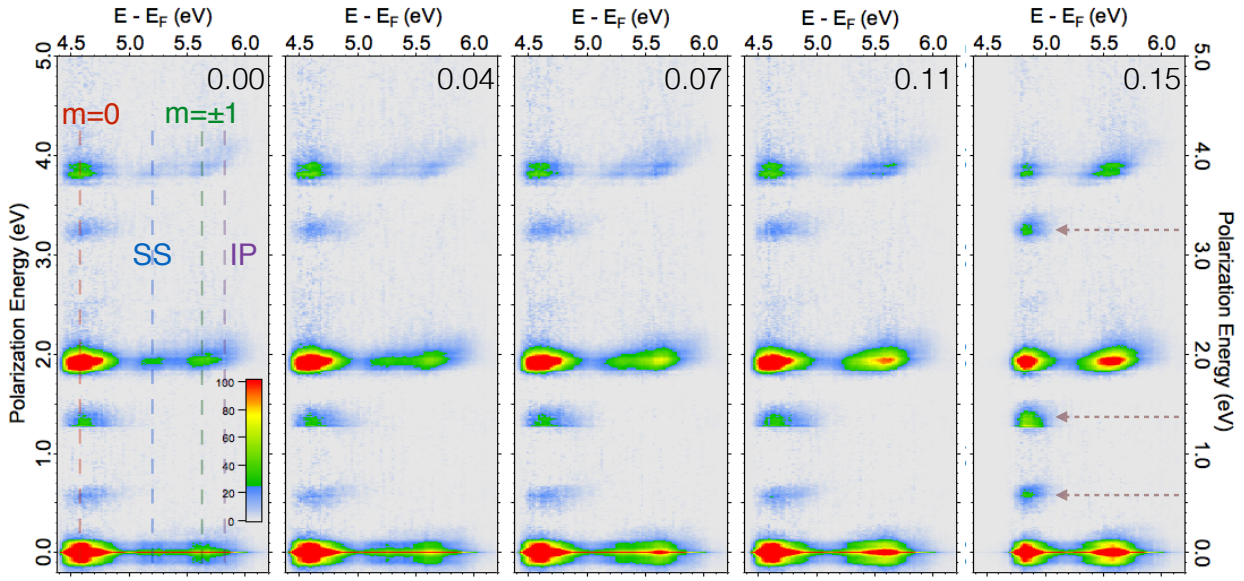

Figure 6.3: The 2D photoelectron spectra obtained by Fourier transforming interferometric scan from Figure 6.2 taken at different $k_{||}$ marked on the right top corner in each figure. The vertical dashed lines indicate the spectral features and the horizontal dashed arrows point to the satellite components, which are only observed for m=0.

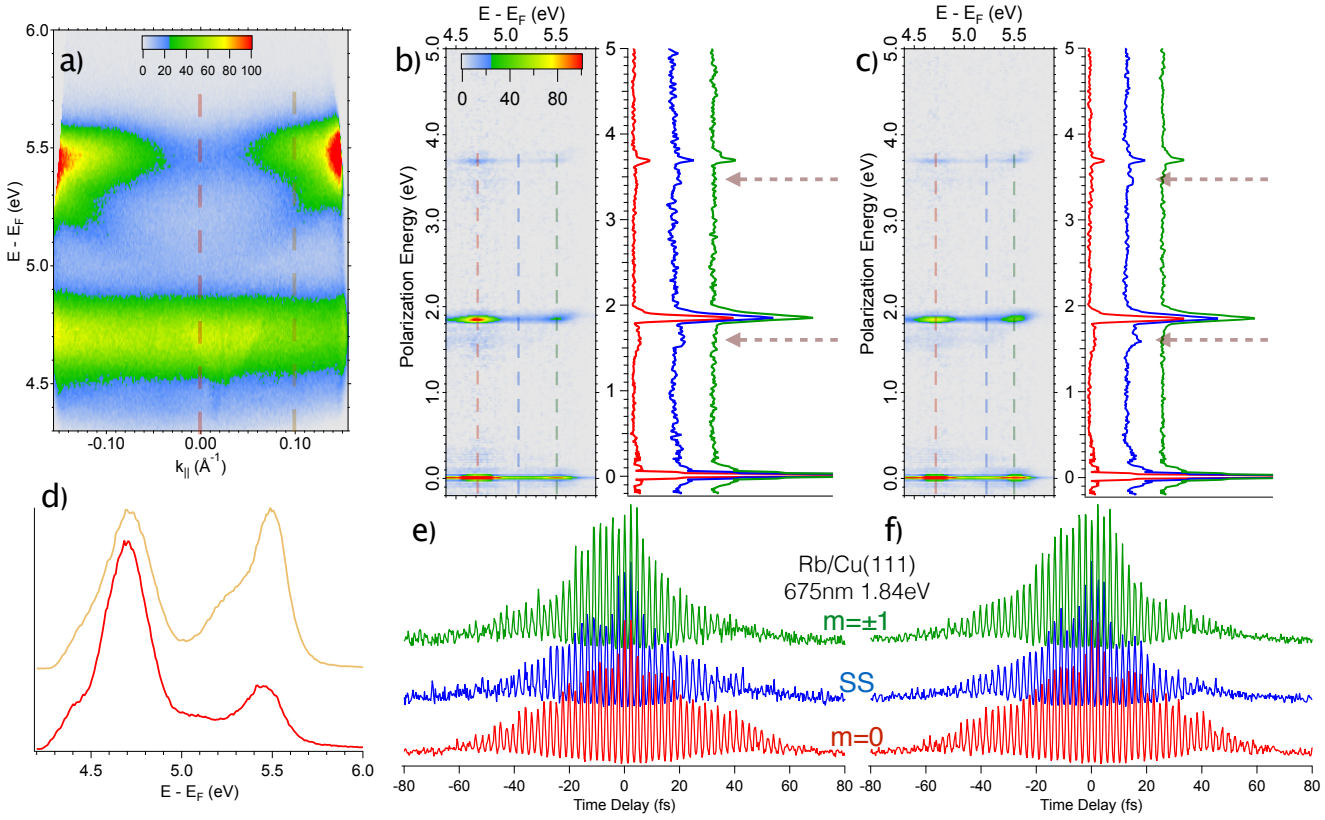

Figure 6.4: **(a)**The 3PP/4PP spectrum with $\hbar\omega$=1.84 eV excitation of Rb/Cu(111) surface. **(b)** and **(c)** The 2D photoelectron spectra obtained by Fourier transforming for interferometric scan from Rb/Cu(111) surface for $k_{||}$=0 Å^{-1} and $k_{||}$=0.12 Å^{-1}, corresponding line profiles at different state energies on the right side. **(d)**The line profiles taken at different $k_{||}$ marked in **(a)**. **(e)** and **(f)** I2PC scans for the data in **(b)** and **(c)**. The polarization beating gives the anomalous intensity for the first two cycles at time zero.

fact provides a hint that the beating phenomenon is at least in part due to the substrate. As described above, for $\hbar\omega$=1.91 eV excitation, the first satellite component is around $\frac{1}{3} \times \hbar\omega_l$. However for $\hbar\omega$=1.84 eV excitation, the first component is clearly below $\frac{1}{3} \times \hbar\omega_l$. In another words, the satellite components move closer to the main integer laser polarizations, which causes the beating to be slower and less pronounced. The smaller shift of the satellite peaks from the integer peaks is also consistent with a smaller detuning of the virtual two-photon state excited from SS from the SS to σ-resonance two-photon resonant excitation. By contrast, for excitation with $\hbar\omega$=1.97 eV light, the satellite peaks are not observed for Cs, and the cross sections through the 2D spectra for the integer peaks have asymmetric Fano-type lineshapes.

Additionally, as described in Chapter 4 and Chapter 5, as the alkali covrage is increased, the energies of the alkali induced resonances as well as the work function also decrease. Thus, it is important to evaluate the relevance of alkali atom coverages on the polarization beating behavior. Figure 6.5(a)-(c) shows the 2D spectra from different coverages of Cs/Cu(111), with the corresponding work functions marked in each figure. Figure 6.5(d) shows the effect of coverage change by plotting the line profiles from the 3PP spectra normalized to the highest intensity σ-resonance peak. The spectra show that all of the surface states experience similar shift, and therefore the detuning of the virtual two-photon state from the

σ-resonance remains relatively constant. Significantly, from Figure 6.5(e) we can see that, at $\hbar\omega$=1.91 eV, through different coverages, the quantum beating signals are very similar for the different Cs coverages.

Before discussing the origin of the satellite polarization component, I present another mode of analysis. Figure 6.6 presents a series of 2D photoelectron spectra obtained by Fourier filtering the interferograms for the Cs/Cu(111) surface with $\hbar\nu$=1.91 eV excitation. Here, the interferograms using filters at the dominant integer and fractional components are presented with a color scale that indicates the intensity of the signals at different polarization energies. The plots are presented for different emission angles corresponding to 0, 6, and 12°. It can be seen that the integer components contribute to all features in the spectra, as expected, but the fractional components are only seen for the σ-resonance. The observed behavior in this analysis is consistent with the 2D spectra, and provides some estimate of how fast each component decays. In the next section, I will discuss the origin of the polarization beating and the associated satellite signals in the 2D spectra.

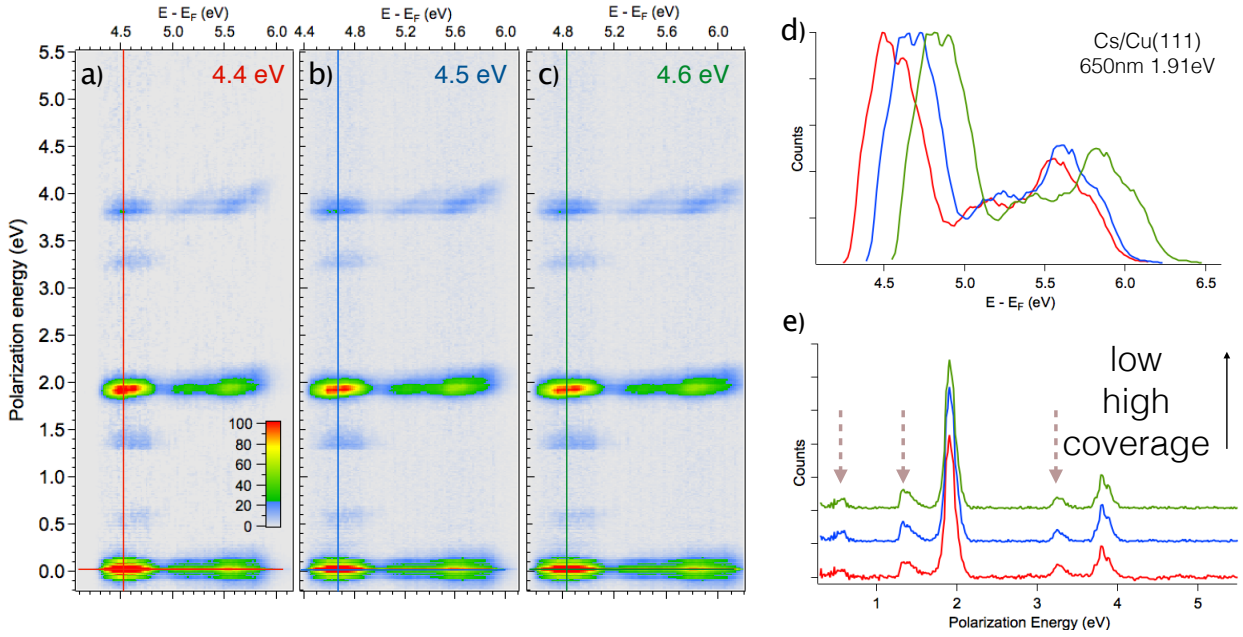

Figure 6.5: **(a)-(c)** The 2D photoelectron spectra obtained by Fourier transforming interferometric scan from Cs/Cu(111) surface for $k_{||}$=0 Å^{-1} at different Cs coverages. The numbers at the upper right corner indicate the work function of the Cs adsorbed Cu(111) surface. **(d)** The line profiles of 3PP spectra at different coverages. **(e)** The line profiles from **(a)-(c)** at the σ-resonance.

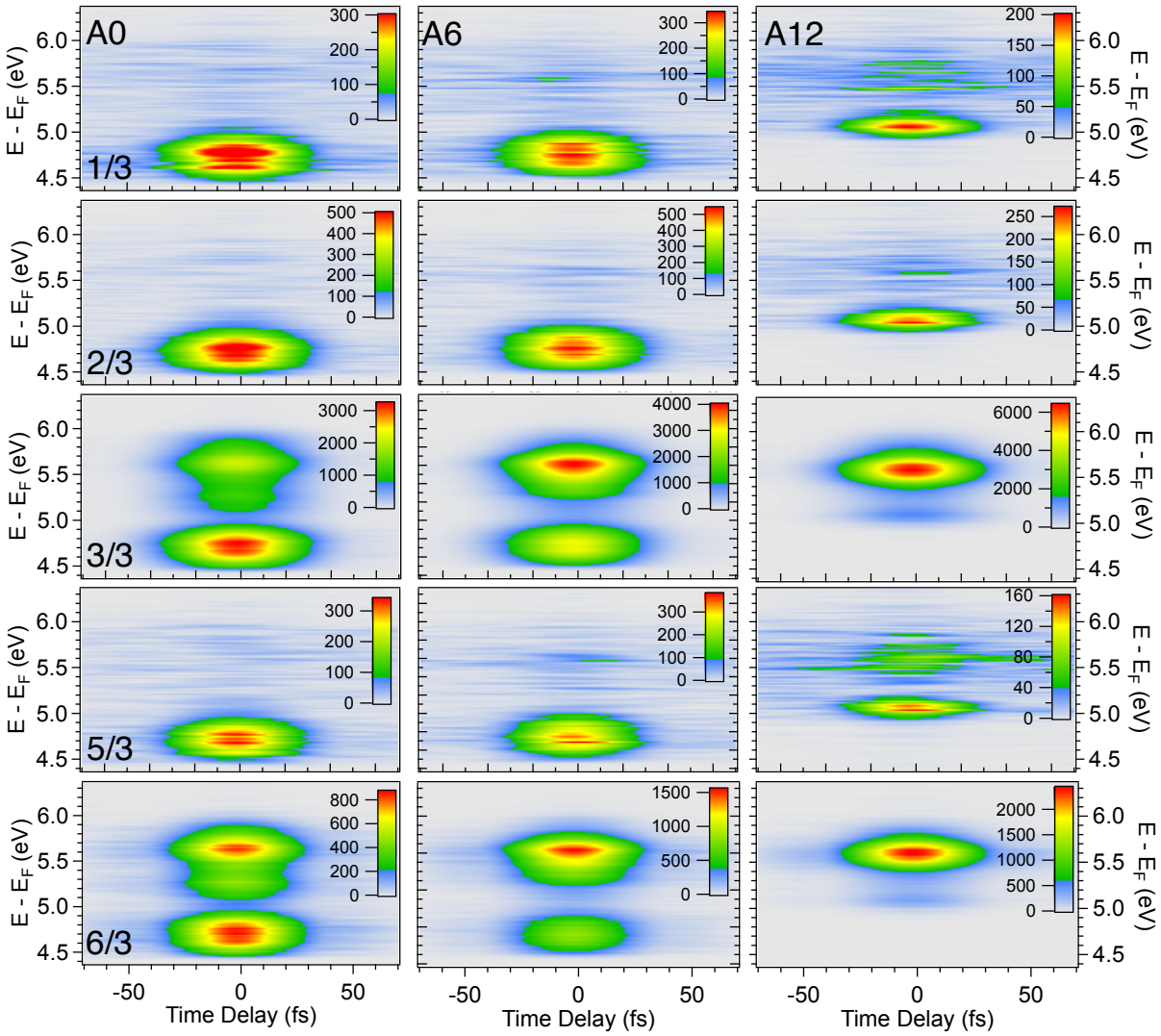

Figure 6.6: Fourier filtered correlation scans at harmonics (3/3 and 6/3) of the laser frequency and subharmonics (1/3, 2/3, and 5/3) from Cs/Cu(111). A0/A6/A12 are the spectra at different emission angle and the numbers at the lower left corner are the fractions of the fundamental laser frequency ($\hbar\omega$).

6.2 MULTI-ELECTRON DYNAMICS

In this section, I will describe the multi-electron (ME) dynamics process driven by the Coulomb screening for the alkali/Cu(111) system that are responsible for the excitation of the σ-resonance.

Figure 6.7 describes the screening response of a metal surface to the Coulomb fields of an alkali atom in its proximity. The Coulomb field of the positive core of an alkali atom creates a negative image charge in the substrate. At the same time, the ns valence of electron alkali atom creates a positive image charge at the surface. The ns electron feels both of the image charges, which are attractive for the own image and repulsive for the core image. The two potentials are written as:

$$V_{IP} = -\frac{1}{4z} \tag{6.1}$$

$$V_{\Delta} = \frac{1}{\sqrt{(R_{ads}+z)^2 + |\rho|^2}} \approx \frac{1}{2z} \sim 1.5eV, \tag{6.2}$$

where ρ is the distance between the atom core and ns electron, and z is the distance between the atom and the image plane, and R_{ads} is the adsorption distance of alkali cation from the

surface plane. Adding the potentials and averaging over ρ gives the net potential experienced by the ns electron of $\frac{1}{4z}$. This net repulsion lifts the ns electron energy level above the Fermi level, so that upon chemisorption alkali atoms are ionized. Using the R_{ads} of Rb and Cs on Cu(111) surface, the Coulomb field experienced by ns electron is ∼1.5 eV.[12]

From the mPP spectra of Rb and Cs on Cu(111) surfaces (Figure 6.1(b) and Figure 5.2(a)), the σ-resonance has the highest intensity, although the only resonant transition in this region is from SS to π-resonance. The polarization beating with a period of ∼6.5 fs with laser pulse ∼20 fs shows up at the σ-resonance in the interferometric pump-probe measurements, which seemingly violates the energy-time uncertainty, as shown in Figure 6.2(e). Because the laser does not have the bandwidth to coherently excite the satellite polarization features. Upon photoexcitation, one electron is excited from SS to a two-photon virtual state, which is detuned by ∼0.65 eV from the σ-resonance. σ-resonance can be excited if a scattering process causes a decay of the virtual state within its lifetime of ∼1 fs, which is implied by its detuning. A fast and efficient scattering of the virtual state can be expected because the virtual state electron creates a Coulomb field of 1.5 eV, corresponding to the creation of a neutral alkali atom at the position of the chemisorbed cation. This Coulomb field elicits fast screening response of the 2D electron gas represented by the Shockley surface state. Thus, the screening response to the virtual state creates

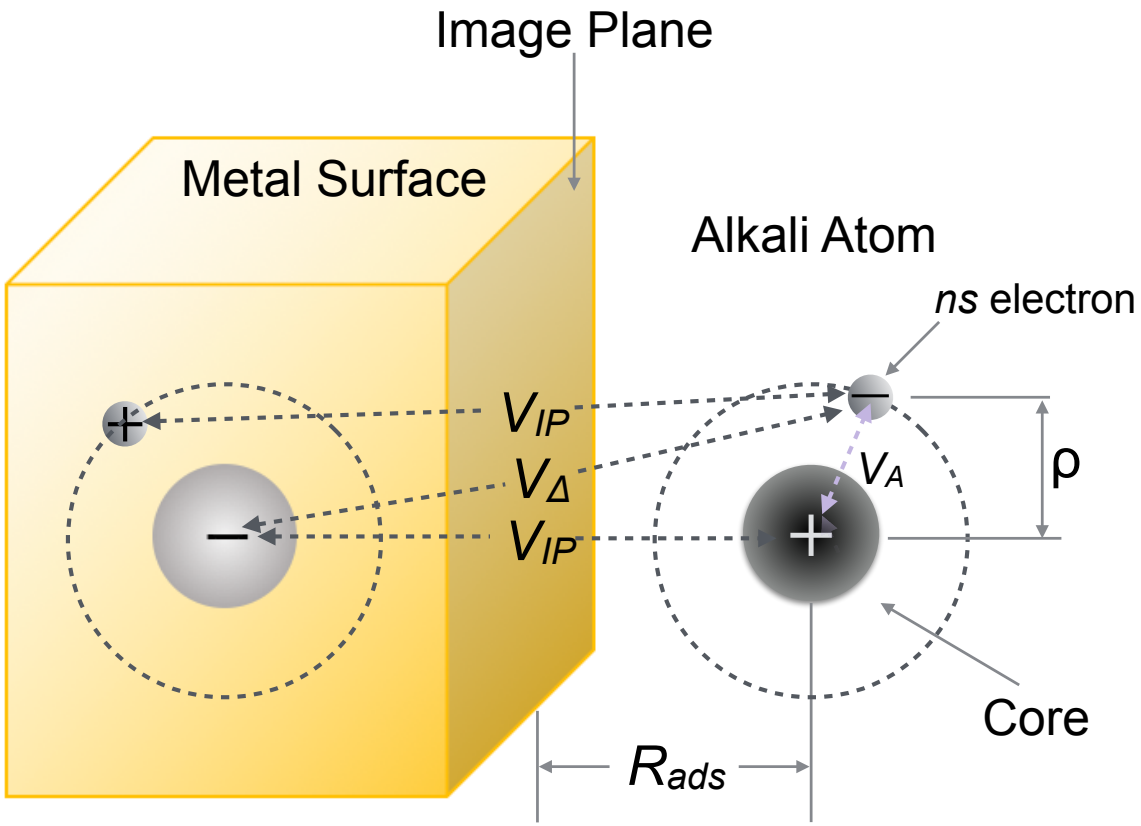

Figure 6.7: The scheme of Coulomb screening when an alkali atom approaches the metal surface.

secondary excitations within SS that terminate at E_F. The two-photon transitions of a single electron excites a ME transition, which populates the σ-resonance and simultaneously excites the screening charge density in the 2D electron gas. For the ME process to be coherent and efficient, the Coulomb interaction must be larger than the detuning of the virtual state and occur within an optical cycle, which is satisfied by the 1.5 eV Coulomb energy. Thus, we propose that the polarization beating is the signature of the ME process associated with the screening response of the Shockley surface state.

So how do we explain the satellite components at approximately $1/3, 2/3$ and $5/3$ sub-harmonics of $\hbar\omega$, which cannot be excited directly since they are out of the range of laser pulses bandwidth. These components give the proof of the ME process in the coherent excitation via the σ-resonance. Figure 6.8(d) shows the possible ME excitation at different photon energies. The virtual two-photon state above σ-resonance excited from SS is detuned by $1/3\hbar\omega$ to the σ, which leads to the components at $2/3\hbar\omega$ and $5/3\hbar\omega$ frequencies, if one assumes that the scattering occurs after one- or two-photon absorption. The two-photon excitation terminating at the σ-resonance is possible if $1/3\hbar\omega$ energy can be transferred efficiently to other excitations on a time scale $\sim$1 fs. For the excitation with $\hbar\omega$=1.91 eV, the Fermi energy of SS is approximately $1/3\hbar\omega$, and therefore the whole Fermi sea can participate in the screening response corresponding to the green arrow in Figure 6.8(d). If

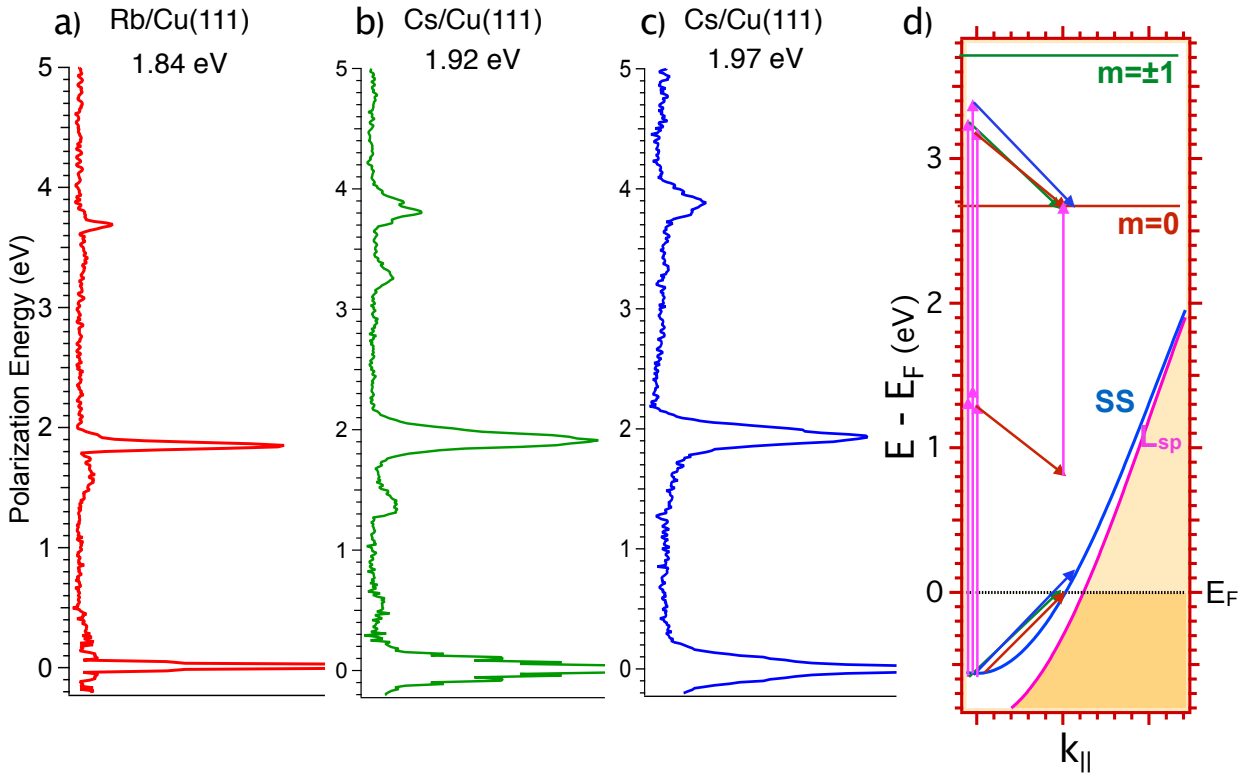

Figure 6.8: **(a)-(c)** The cross sections through 2D spectra at different photon energies for the σ-resonance of Cs and Rb on Cu(111), which show how the satellite polarization changes with photon energy. They show how at different photon energy, the multi-electron excitation affects the coherent response. **(d)** The excitation processes that explain the multi-electron excitation scheme for **(a)-(c)**. The satellite features can only be seen if electrons can be excited from the SS to E_F.

the photon energy is $\hbar\omega$=1.84 eV, the ME excitation can still occur to the to E_F of SS, but the a smaller fraction of SS electrons can be excited in the screening response, as indicated by the red arrow in Figure 6.8(d). This gives a weaker ME process, and the detuning form $1/3\hbar\omega$ gives less pronounced beating. If the photon energy is $\hbar\omega$=1.97 eV, the ME excitation can no longer occur to the to E_F of SS. The ME process is still possible, and probably is responsible for the Fano type lineshapes for the 2D spectrum in Figure 6.8(c). Without the sharp preference of the excitations to E_F that is mandated by the screening response one no longer observes the polarization beating. Therefore it seems that the polarization beating is probed when the screening response can excite single-electron transitions to E_F (the red and the green arrows). For larger detunings where single-electron transitions terminate above E_F, the ME process is still possible, but the polarization beating within the laser pulse disappears (the blue arrow).

7.0 SUMMARY AND CONCLUSIONS

Using 3D angle and time resolved 3PP spectroscopy with our tunable NOPA laser setup and electronic structure theory we studied the electronic structure and lifetimes of Cs and Rb at <0.02 ML coverage on the transition metal Ru(0001) surface. We found the σ- and π-resonances at comparable binding energies with respect to the vacuum level as the same resonances on the Cu(111) noble metal surfaces. This similarity suggests that the ionic interactions between the alkali ions and Ru(0001) surface dominate the alkali chemisorption as on noble metals.[12] The energy separation between the σ- and π-resonances is smaller than in 3PP measurements for Cu(111). This difference between previous measurements can be attributed in part to a slightly higher alkali coverage used in the Ru(0001) experiments, the more favorable detection of the alkali resonances with 3PP and 4PP excitation schemes, and to a higher photoelectron spectroscopic resolution.

Although the σ- and π-resonance binding energies in the zero coverage limit are consistent

with the ionic bonding, we find strong differences in that the interaction among alkali atoms that are mediated by the Ru(0001) surface through a significant hybridization with the d-bands of the substrate. The σ- and π-resonances exhibit strong dispersions at coverages as low as <0.02 ML with positive and negative effective masses, which reflect their m=0 and ± 1 orbital character. DFT calculations confirm the tendency for band formation for Ru(0001) but not for Cu(111) surface, and attribute it to more effective hybridization of alkali atom orbitals with the d-bands of the Ru substrate. Such interactions are expected to be stronger for transition metals than for noble metals because of the higher energy and larger bandwidths of the d-bands.

With increasing alkali atom coverage the binding energy is linearly proportional with $\Delta\Phi^{3/2}$ due to the formation of the dipole potential. The tuning of the energies is different for the σ- and π-resonance of alkali/Ru(0001) most likely due to the additional influence of band formation, which shifts their energies in the opposite direction at the Γ point.

In addition, we measured ITR-3PP data for the Cs and Rb/Ru(0001) surfaces in order to characterize the photoexcitation dynamics and alkali resonance lifetimes. The observed lifetimes of 40 and 20 fs for the σ- and π-resonances of Cs and Rb are consistent with a stronger inelastic decay channel on Ru(0001) than for Cu(111) due to the presence of d-bands near the Fermi level as compared to noble metals. Overall, the character of the alkali

atom-transition metal interactions shows strong influence of the d-bands on the alkali atom band dispersions and resonance lifetimes.

Finally, we observed the ME dynamics in the nonlinear 3PP through Cs and Rb localized electronic resonances on Cu(111) surface. In the ITR-3PP measurements on Cs and Rb/Cu(111) surfaces, the I2PC for the σ-resonance shows the coherent beating with a period of 6.5 fs in a narrow excitation photon energy range about $\hbar\omega$=1.91 eV, which implies that the coherent electronic response evolves faster, and creates coherent polarization components outside of the time-frequency bandwidth of the laser pulse in seeming violation of the energy-time uncertainty. By Fourier transforming the time domain correlation measurements with we obtain 2D spectra, which identify the dominant frequency components that are responsible for the polarization beating; besides the main polarization components at the fundamental $\hbar\omega$ frequency and its higher harmonics, there are additional satellites at approximately $1/3, 2/3$ and $5/3$ sub-harmonics of $\hbar\omega$ appear at the σ-resonance. The satellites components are manifestations of ME dynamics, which enable the nonresonant excitation of the σ-resonance when the detuning of the photoexcited virtual state from the σ-resonance corresponds to the excitation energy from the bottom of SS to E_F. The ME process is efficient, because photoinduced charge transfer elicits the screening response of the metal surface, and in particular by the Shockley surface state.

APPENDIX

MATLAB CODE FOR PARAMETER SIMULATIONS

A.1 SIMULATION OF TIME PARAMETERS FOR FOUR ENERGY LEVELS SYSTEM

The MATLAB code here is the simulation procedure described in Chapter 3, including the decomposition of I2PC and time parameter selection.

```
%configuration
clear;
foldername='VaryingE2_changeDephaseTime';
tspan=[-300, 500];
N=4;
```

```
E=[-0.09,2.05,4.19,6.33];

laserE=2.14;

lambda=1239.84/laserE;

Temperature=90; %Temperature. unit: K

E_final=6.33;

dlmwrite('folder/E.txt',E);



deltaRange=[-80,80];

deltaInterval=0.16;

filename='VaryingE2';

SwitchRho1=0; %wheather to draw Rho1

folderP='/User/Machree/Simulation';



T=zeros((N+1)*N/2,1);

T(1)=inf;

T(2)=1;

T(3)= 27;

T(4)= 11;
```

```
T(5)= 1;

T(6)= 1;

T(7)= 7;

T(8)= 8;

T(9)= 1;

T(10)= 10;

dlmwrite('folder/T.txt',T);


P=ones(2*N-1,1)*0.0005;

order0_exp=load('folder/3ppe/SigCsRu3p1/exp/order0.txt');

order1_exp=load('folder/3ppe/SigCsRu3p1/exp/order1.txt');

order2_exp=load('folder/3ppe/SigCsRu3p1/exp/order2.txt');

order3_exp=load('folder/3ppe/SigCsRu3p1/exp/order3.txt');

fitcoeff_exp=load('folder/3ppe/SigCsRu3p1/exp/fitcoeff.txt');

sigma0_exp=fitcoeff_exp(3);

sigma1_exp=fitcoeff_exp(9);

sigma2_exp=fitcoeff_exp(12);

sigma3_exp=fitcoeff_exp(15);
```

```
%create folder
folder=[folderP '/' foldername '/'];
if exist(folder,'dir')
else mkdir('folder');
end
%generate initial value for Rho. Name: y0
y0=zeros((N+1)*N/2+1,1);
FDD= @(X_E) 1./(exp(X_E/(8.6173324e-5*...
Temperature))+1); %Fermi-Dirac Distribution
y0(1:N)=FDD(E)*1e23;
%manipulate T
for ii=1:1:N-1
    for jj=1:1:N-ii
        m=ii+jj;
        n=jj;
        k=@(x,y) N*(x-y)+y-(x-y-1)*(x-y)/2;
        T(k(m,n))=1/(1/T(k(m,n))+0.5/T(k(m,m))+0.5/T(k(n,n)));
    end
```

```
end

delta=deltaRange(1):deltaInterval:deltaRange(2);



YData=0.*delta;

% checking to see if my pool is already open

if matlabpool('size') == 0

    matlabpool open 2

end

for jj=1:20

tic

parfor ii=1:length(delta)

    Ew=2*pi*300.*E_final/1239.84;

    ode=@(t,Rho) OBE_NLevel(t,Rho,delta(ii),T,Ew,P,lambda,N,y0);



    [t,Rho] = ode45(ode, tspan, y0);

    YData(ii)=Rho(end,end);

%

end
```

```
toc

YData=YData/max(YData);

figure;

h=plot(delta,YData);

dlmwrite(['folder/',jj,'/PiCsRu',num2str(E_final(jj)),...

'.txt'],YData,'delimiter','\r');

dlmwrite(['folder/',jj,'time.txt'],delta,'delimiter','\r');



%FFT

IFSNorm=YData;

t=delta;

delay_0=find(t==0);

IFSNorm_new=circshift(IFSNorm,[1-delay_0  0]);

IFSNorm_FFT=real(fftshift(fft(IFSNorm_new,[],1)));

% figure;

% plot(IFSNorm_FFT);

[maxvalue,locs]=findpeaks(IFSNorm_FFT);

medium=ceil(length(locs)/2);
```

```
locs0=locs(medium);locs1=locs0+84;locs2=locs1+84;locs3=locs2+84;
width=4; %the width for the square wave
Plotlength=160; %better to be even
%Create a matrix to store the envelope info
order0=zeros(Plotlength,2);
order1=zeros(Plotlength,2);
order2=zeros(Plotlength,2);
order3=zeros(Plotlength,2);


for i=1:Plotlength
    % Generate square wave in order to choose a small region
%       Toffset=(max(t)-min(t))*i/Plotlength+t(1);
     Toffset=(180)*i/Plotlength+t(1);
     ft=transpose(rectpuls(t+Toffset,width));


    % Get the small region
     for j=1:length(ft)
          Pointft(j)=ft(j)*IFSNorm(j);
```

```
    end
    %Circshift
%       delay_0=find(t==0);
    Pointft_new=circshift(Pointft,[1-delay_0  0]);
    %FFT
    Pointft_FFT=real(fftshift(fft(Pointft_new',[],1)));
   order0(i,:)=[max(Pointft_FFT)/(width/Tdelta),Toffset];
    if  order0(i,1)==0
        order0(i,1)=0.04;
    end
    order1(i,:)=[max(Pointft_FFT(locs1-2:locs1+2))...
    /(width/Tdelta),Toffset];
    order2(i,:)=[max(Pointft_FFT(locs2-2:locs2+2))...
    /(width/Tdelta),Toffset];
    order3(i,:)=[max(Pointft_FFT(locs3-2:locs3+2))...
    /(width/Tdelta),Toffset];
end
save(['folder/',jj,'/order0.txt'],'order0','-ascii');
```

```
save(['folder/',jj,'/order1.txt'],'order1','-ascii');

save(['folder/',jj,'/order2.txt'],'order2','-ascii');

save(['folder/',jj,'/order3.txt'],'order3','-ascii');


 order0_fit=fit(order0(:,2),order0(:,1),'gauss2');

 order1_fit=fit(order1(:,2),order1(:,1),'gauss1');

 order2_fit=fit(order2(:,2),order2(:,1),'gauss1');

 order3_fit=fit(order3(:,2),order3(:,1),'gauss1');

 coefforder0=transpose(coeffvalues(order0_fit));

 coefforder1=transpose(coeffvalues(order1_fit));

 coefforder2=transpose(coeffvalues(order2_fit));

 coefforder3=transpose(coeffvalues(order3_fit));


 save(['folder/',jj,'/fitcoeff.txt'],'coefforder0','coefforder1',...

 'coefforder2','coefforder3','-ascii')

 save(['folder/',jj,'/order0_fit.mat'],'order0_fit');

 save(['folder/',jj,'/order1_fit.mat'],'order1_fit');

 save(['folder/',jj,'/order2_fit.mat'],'order2_fit');
```

```
save(['folder/',jj,'/order3_fit.mat'],'order3_fit');


figure;
plot(t,IFSNorm);
title('iteration=' jj);
hold on;
plot(order0_fit);
plot(order1_fit,'c');
plot(order2_fit,'y');
plot(order3_fit,'g');
hold off


sigma0=coefforder0(3);
sigma1=coefforder1(3);
sigma2=coefforder2(3);
sigma3=coefforder3(3);


h3=ttest2(order3_exp,order3_fit);
```

```
h2=ttest2(order2_exp,order2_fit);

h1=ttest2(order1_exp,order1_fit);

h0=ttest2(order0_exp,order0_fit);


if h3==1

    tmp=sigma3-sigma3_exp;

    if abs(tmp)>2

        T(10)=T(10)-tmp;

    else if

            T(10)=T(10)-int(tmp);

        end

    end

    continue

end


if h3==0

    disp(['T(10)= ' T(10)]);

    if h2==1
```

```
        tmp=sigma2-sigma2_exp;
        if abs(tmp)>2
            T(8)=T(8)-tmp;
        else if
             T(8)=T(8)-int(tmp);
            end
        end
    continue
    disp(['iteration= ' jj]);
    end
end


if h3==0
    if h2==0
        disp(['T(8)= ' T(8)]);
        if h1==1
            tmp=sigma1-sigma1_exp;
            if abs(tmp)>2
```

```
                T(7)=T(7)-tmp;
            else if
                T(7)=T(7)-int(tmp);
                end
            end
        continue
        disp(['iteration= ' jj]);
         end
    end
end


if h3==0
    if h2==0
        if h1==0
            disp(['T(7)= ' T(7)]);
            if h0==1
                tmp=sigma0-sigma0_exp;
                if abs(tmp)>2
```

```
                T(4)=T(4)-tmp;

                T(3)=T(3)-tmp;

            else if

                T(4)=T(4)-int(tmp);

                T(3)=T(3)-int(tmp);

                end

            end

            continue

            disp(['iteration= ' jj]);

        end

    end

end



if h3==0

    if h2==0

        if h1==0

            if h0==0
```

```
                disp(['Final iteration= ' jj]);
                break
            end
        end
    end
 end
end
```

A.2 DISCRIPTION OF OPTICAL BLOCH EQUATION IN MATLAB CODE

In the following MATLAB code, the four-energy level Optical Bloch equations is written out. The last section will require the functions of OBE here.

```
function Rho_prime=OBE_NLevel(t,Rho,delta,T,wE,P,lambda,N,Rho0)
w=2*pi*300/lambda;
%H describe the perbation. H=-e*r*E_package*cos().
%Ep includes everything except polarization P=<m|r|n>.
```

```
H=-P.*Ep(t,lambda,delta);

Rho_prime=zeros((N+1)*N/2+1,1);

kk=@(x,y) N*(x-y)+y-(x-y-1)*(x-y)/2;

for ii=2:1:N

    Rho_prime(ii)=-(Rho(ii)-Rho0(ii))/T(ii);

    if ii-1>0

        Rho_prime(ii)=Rho_prime(ii)-...

            1i*H(kk(ii,ii-1))*exp(1i*w*t)*conj(Rho(kk(ii,ii-1)))+...

            1i*H(kk(ii,ii-1))*exp(-1i*w*t)*Rho(kk(ii,ii-1));

    end

    if ii+1<=N

        Rho_prime(ii)=Rho_prime(ii)-...

            1i*H(kk(ii+1,ii))*exp(-1i*w*t)*Rho(kk(ii+1,ii))+...

            1i*H(kk(ii+1,ii))*exp(1i*w*t)*conj(Rho(kk(ii+1,ii)));

    end

    Rho_prime(1)=Rho_prime(1)-Rho_prime(ii);

end

%polarization part.
```

```
for ii=1:1:(N-1)
    for jj=1:1:(N-ii)
        m=ii+jj;
        n=jj;
        k_tmp=kk(m,n);
        %phase oscillation
        Rho_prime(k_tmp)=-1i*((wE(m)-wE(n))-ii*w)*Rho(k_tmp)-...
            Rho(k_tmp)/T(k_tmp)-... %phase relaxation
            % surely N>=m-1>=n
            1i*H(kk(m,m-1))*exp(1i*w*t)*Rho(kk(m-1,n))+...
            %surely N>=m>=n+1>=0
            1i*H(kk(n+1,n))*exp(1i*w*t)*Rho(kk(m,n+1));
        if m+1<=N
            Rho_prime(k_tmp)=Rho_prime(k_tmp)-1i*...
            H(kk(+1,m))*exp(-1i*w*t)*Rho(kk(m+1,n));
        end
        if n-1>=1
            Rho_prime(k_tmp)=Rho_prime(k_tmp)...
```

```
                +1i*H(kk(n,n-1))*exp(-1i*w*t)*Rho(kk(m,n-1));

            end

        end

end

Rho_prime(end)=Rho(N);

end
```

BIBLIOGRAPHY

[1] Y. Wang, W. Wang, K. N. Fan, and J. Deng.
Surface Science, 490:125 – 132, 2001.

[2] R. Courths, H. Wern, U. Hau, B. Cord, V. Bachelier, and S .Hufner.
Journal of Physics F: Metal Physics, 14(6):1559, 1984.

[3] R. Courths and S. Hüfner.
Physics Reports, 112(2):53 – 171, 1984.

[4] H. Eckardt, L. Fritsche, and J. Noffke.
Journal of Physics F: Metal Physics, 14(1):97, 1984.

[5] W. K. Siu and R. A. Bartynski.
Physics Review B, 75:235427, 2007.

[6] T. Pelzer, G. Ceballos, F. Zbikowski, B. Willerding, K. Wandelt, U. Thomann, C. Reuß, T. Fauster, and J. Braun.
Journal of Physics: Condensed Matter, 12(10):2193, 2000.

[7] N. A. W. Holzwarth and J. R. Chelikowsky.
Solid State Communications, 53(2):171 – 174, 1985.

[8] P. Nieto, D. Farias, R. Miranda, M. Luppi, E. J. Baerends, M. F. Somers, M. J. T. C. van der Niet, R. A. Olsen, and G. J. Kroes.
Physical Chemistry Chemical Physics, 13:8583–8597, 2011.

[9] N. Fischer, S. Schuppler, Th. Fauster, and W. Steinmann.
Surface Science, 314(1):89 – 96, 1994.

[10] J. P. Gauyacq, A. G. Borisov, and M. Bauer.
Progress in Surface Science, 82:244 – 292, 2007.

[11] H. Petek, M. J. Weida, H. Nagano, and S. Ogawa.
Surface Science, 451:22 – 30, 2000.

[12] J. Zhao, N. Pontius, A. Winkelmann, A. Sametoglu, V.and Kubo, A. G. Borisov, D. Sánchez-Portal, V. M. Silkin, E. V. Chulkov, P. M. Echenique, and H. Petek.
Physics Review B, 78:085419, 2008.

[13] A. G. Borisov, V. Sametoglu, A. Winkelmann, A. Kubo, N. Pontius, J. Zhao, V. M. Silkin, J. P. Gauyacq, E. V. Chulkov, P. M. Echenique, and H. Petek.
Physics Review Letters, 101:266801, 2008.

[14] L. M. Wang, V. Sametoglu, A. Winkelmann, J. Zhao, and H. Petek.
Journal of Physics Chemistry A, 115(34):9479–9484, 2011.

[15] S. Ogawa, H. Nagano, and H. Petek.
Surface Science, 427-428:34 – 38, 1999.

[16] H. Petek, H. Nagano, M. J. Weida, and S. Ogawa.
Journal of Physical Chemistry B, 105(29):6767–6779, 2001.

[17] F. Träger.
Springer Handbook of Lasers and Optics.

Springer, 2007.

[18] H. Petek, A. P. Heberle, W. Nessler, H. Nagano, S. Kubota, S. Matsunami, N. Moriya, and S. Ogawa.
Physics Review Letters, 79:4649–4652, 1997.

[19] E. Knoesel, A. Hotzel, and M. Wolf.
Physics Review B, 57:12812 – 12824, 1998.

[20] S. Hüfner.
Photoelectron Spectroscopy, 3rd edition.
Springer, 2003.

[21] E. V. Chulkov, V. M. Silkin, and P. M. Echenique.
Surface Science, 437(3):330 – 352, 1999.

[22] T. Hertel, E. Knoesel, M. Wolf, and G. Ertl.
Physics Review Letters, 76:535 – 538, 1996.

[23] I. Langmuir.
Journal of the American Chemical Society, 54(7):2798–2832, 1932.

[24] I. Langmuir.
Physics Review, 43:224–251, 1933.

[25] P. Nordlander and J. C. Tully.
Physics Review B, 42:5564–5578, 1990.

[26] H. Winter.
Phys. Rep., 367(5):387 – 582, 2002.

[27] J. Topping.
Journal of Proceedings of the Royal Society A, 114:67 – 72, 1927.

[28] H. P. Bonzel, A. M. Bradshaw, and G. Ertl.
Physics and Chemistry of Alkali Metal Adsorption.
Elsevier, Amsterdam, 1989.

[29] S. Yamamoto.
Reports on Progress in Physics, 69(1):181, 2006.

[30] J. B. Taylor and I. Langmuir.
Physics Review, 44:423–458, 1933.

[31] K. Oura, V. G. Lifshits, A. A. Saranin, A. V. Zotov, and M. Katayama.
An Introduction, Surface Science.
Springer Verlag, 2003.

[32] R. W. Gurney.
Physics Review, 47:479–482, 1935.

[33] R. D. Diehl and R. McGrath.
Journal of Physics: Condensed Matter, 9(5):951, 1997.

[34] N. D. Lang.
Physics Review B, 4:4234, 1971.

[35] N. D. Lang and A. R. Williams.
Physics Review Letters, 37:212, 1976.

[36] N. D. Lang and A. R. Williams.
Physics Review B, 18:616–636, 1978.

[37] A. G. Borisov, J. P. Gauyacq, E. V. Chulkov, V. M. Silkin, and P. M. Echenique.
Physics Review B, 65:235434, 2002.

[38] J. P. Muscat and D. M. Newns.

Progress in Surface Science, 9(1):1 – 43, 1978.

[39] J. P. Muscat and D. M. Newns.

Solid State Communications, 11(5):737 – 741, 1972.

[40] J. P. Muscat and D. M. Newns.

Journal of Physics C: Solid State Physics, 7(15):2630, 1974.

[41] J. P. Muscat and D. M. Newns.

Surface Science, 74(2):355 – 364, 1978.

[42] J. P. Muscat and D. M. Newns.

Surface Science, 84(2):262 – 274, 1979.

[43] H. Ishida.

Physics Review B, 38:8006–8021, 1988.

[44] H. Ishida.

Physics Review B, 39:5492–5495, 1989.

[45] B. Woratschek, W. Sesselmann, J. Küppers, G. Ertl, and H. Haberland.

Physics Review Letters, 55:1231–1234, 1985.

[46] H. Wedler, M. A. Mendez, P. Bayer, U. Löffler, K. Heinz, V. Fritzsche, and J. B. Pendry.

Surface Science, 293(1):47 – 56, 1993.

[47] W. C. Fan and A. Ignatiev.

Journal of Vacuum Science & Technology A, 6:735–738, 1988.

[48] D. Fisher, Z. Y. Li, and R. D. Diehl.

Surface Science, 259(1):85 – 94, 1991.

[49] D. Heskett, K. H. Frank, E. E. Koch, and H. J. Freund.
Physics Review B, 36:1276–1279, 1987.

[50] D. A. Arena, F. G. Curti, and R. A. Bartynski.
Physics Review B, 56:15404–15411, 1997.

[51] K. Giesen, F. Hage, F. J. Himpsel, H. J. Riess, and W. Steinmann.
Physics Review Letters, 55:300–303, 1985.

[52] M. Bauer, S. Pawlik, and M. Aeschlimann.
Physics Review B, 55:10040–10043, 1997.

[53] M. Bauer, S. Pawlik, and M. Aeschlimann.
Physics Review B, 60:5016–5028, 1999.

[54] N. Fischer, S. Schuppler, R. Fischer, Th. Fauster, and W. Steinmann.
Physics Review B, 47:4705–4713, 1993.

[55] H. Petek, M. J. Weida, H. Nagano, and S. Ogawa.
Science, 288(5470):1402–1404, 2000.

[56] H. Petek and S. Ogawa.
Annual Review of Physical Chemistry, 53(1):507–531, 2002.

[57] H. Hertz.
Annalen der Physik, 267(8):983–1000, 1887.

[58] H. P. Bonzel and C. Kleint.
Progress in Surface Science, 49(2):107 – 153, 1995.

[59] P. Y. Yu and M. Cardona.
Fundamentals of Semiconductors.
Springer, 1999.

[60] P. S. Kirchmann, P. A. Loukakos, U. Bovensiepen, and M. Wolf.
New Journal of Physics, 7(1):113, 2005.

[61] R. H. Williams, G. P. Srivastava, and I. T. McGovern.
Reports on Progress in Physics, 43:1357–1414, 1980.

[62] H. Petek and S. Ogawa.
Progress in Surface Science, 56:239 – 310, 1997.

[63] F. Reinert and S. Hüfner.
New Journal of Physics, 7(1):97, 2005.

[64] A. G. Borisov, A. K. Kazansky, and J. P. Gauyacq.
Surface Science, 430:165 – 175, 1999.

[65] N. Del Fatti, C. Voisin, M. Achermann, S. Tzortzakis, D. Christofilos, and F. Vallée.
Physics Review B, 61:16956 – 16966, 2000.

[66] J. J. Quinn and R. A. Ferrell.
Physics Review, 112:812 – 827, 1958.

[67] V. E. Gusev and O. B. Wright.
Physics Review B, 57:2878–2888, 1998.

[68] R. Matzdorf, G. Meister, and A. Goldmann.
Surface Science, 286(1):56 – 65, 1993.

[69] H. Haug and S. W. Koch.
Quantum Theory of the Optical and Electronic Properties of Semiconductors.
World Scientific, Singapore, 1990.

[70] E. D. Palik.
Handbook of Optical Constants of Solids.

Academic Press, New York, 1985.

[71] J. Cao, Y. Gao, R. J. D. Miller, H. E. Elsayed-Ali, and D. A. Mantell.
Physics Review B, 56:1099–1102, 1997.

[72] S. Ogawa, H. Nagano, and H. Petek.
Physics Review B, 55:10869–10877, 1997.

[73] H. Petek, H. Nagano, M. J. Weida, and S. Ogawa.
Chemical Physics, 251:71 – 86, 2000.

[74] J.-D. Diels and W. Rudolph.
Ultrashort Laser Pulse Phenomena.
Academic Press, New York, 2006.

[75] M. J. Weida, S. Ogawa, H. Nagano, and H. Petek.
Journal of the Optical Society of America, 17(8):1443–1451, 2000.

[76] S. Ogawa, H. Nagano, H. Petek, and A. P. Heberle.
Physics Review Lett., 78:1339–1342, 1997.

[77] X. Cui, C. Wang, A. Argondizzo, S. Garrett-Roe, B. Gumhalter, and H. Petek.
Nature Physics, 10:505 – 509, 2014.

[78] G. Pirug, C. Ritke, and H. P. Bonzel.
Surface Science, 257(123):50 – 62, 1991.

[79] J. Hrbek.
Surface Science, 164(1):139 – 148, 1985.

[80] G. Rangelov and L. Surnev.
Surface Science, 185(3):457 – 468, 1987.

[81] A. Argondizzo, X. Cui, H. Wang, C.and Sun, H. Shang, J. Zhao, and H. Petek.
Physics Review B, 91:155429, 2015.

[82] M. Bauer, A. Marienfeld, and M. Aeschlimann.
Progress in Surface Science, 90(3):319 – 376, 2015.

[83] W Berthold, U Höfer, P Feulner, and D Menzel.
Chemical Physics, 251:123 – 132, 2000.

[84] N. Nguyen, M. Mulazzi, and F. Reinert.
Journal of Electron Spectroscopy and Related Phenomena, 191:27 – 34, 2013.

[85] N. Armbrust, J. Güdde, P. Jakob, and U. Höfer.
Physics Review Letters, 108:056801, 2012.

[86] M. Lisowski, P. A. Loukakos, U. Bovensiepen, J. Stähler, C. Gahl, and M. Wolf.
Applied Physics A, 78(2):165–176, 2004.

[87] R. W. Verhoef and M. Asscher.
Surface Science, 391:11 – 18, 1997.

[88] T. Aruga and Y. Murata.
Progress in Surface Science, 31:61 – 130, 1989.

[89] S. Achilli, M. I. Trioni, E. V. Chulkov, P. M. Echenique, V. Sametoglu, N. Pontius, A. Winkelmann, A. Kubo, J. Zhao, and H. Petek.
Physics Review B, 80:245419, 2009.

[90] R. Hoffmann.
Reviews of Modern Physics, 60:601–628, 1988.

[91] J. Zhao, M. Feng, J. Yang, and H. Petek.
ACS Nano, 3(4):853–864, 2009.

[92] M. Ziegler, J. Kröger, R. Berndt, A. Filinov, and M. Bonitz.
Physics Review B, 78:245427, 2008.

[93] Th. von Hofe, J. Kröger, and R. Berndt.
Physics Review B, 73:245434, 2006.

[94] A. P. Graham.
Surface Science Reports, 49:115 – 168, 2003.

[95] S. Achilli, M. I. Trioni, and G. P. Brivio.
Physics Review B, 81:165444, 2010.

[96] S. Achilli, M. I. Trioni, and E. V. Chulkov.
Physics Review B, 85:045408, 2012.

[97] M. I. Trioni, S. Achilli, and E. V. Chulkov.
Progress in Surface Science, 88:160–170, 2013.

[98] J. Zhao, M. Feng, D. B. Dougherty, H. Sun, and H. Petek.
ACS Nano, 8(10):10988–10997, 2014.

[99] J. P. Perdew, K. Burke, and M. Ernzerhof.
Physics Review Letters, 77:3865–3868, 1996.

[100] G. Kresse and J. Hafner.
Physics Review B, 47:558–561, 1993.

[101] G. Kresse and J. Hafner.
Physics Review B, 48:13115–13118, 1993.

[102] G. Kresse and J. Hafner.
Physics Review B, 49:14251–14269, 1994.

[103] G. Kresse and D. Joubert.
Physics Review B, 59:1758–1775, 1999.

[104] A.Winkelmann, C. Tusche, A. A. Ünal, M. Ellguth, J. Henk, and J. Kirschner.
New Journal of Physics, 14(4):043009, 2012.

[105] S. Ogawa, H. Nagano, and H. Petek.
Physics Review Letters, 82:1931–1934, 1999.

[106] P. M. Echenique, J. M. Pitarke, E. V. Chulkov, and A. Rubio.
Chemical Physics, 251(1-3):1–35, 2000.

[107] S. A. Lindgren and L. Walldên.
Solid State Communications, 28(3):283 – 286, 1978.

[108] A. Winkelmann, J. Sametoglu, V.and Zhao, A. Kubo, and H. Petek.
Physics Review B, 76:195428, 2007.

[109] N. Fischer, S. Schuppler, R. Fischer, Th. Fauster, and W. Steinmann.
Physics Review B, 43:14722–14725, 1991.

[110] M. B. Yilmaz, J. I. Dadap, K. R. Knox, N. Zaki, Z. Hao, P. D. Johnson, and R. M. Osgood Jr.
Journal of Vacuum Science & Technology A, 30(4):041403, 2012.

[111] S. Zhang, C. Wang, X. Cui, Y. Wang, A. Argondizzo, J. Zhao, and H. Petek.
Physics Review B, 93:045401, 2016.